



This is to certify that the

dissertation entitled

Optical studies of alkalides and electrides.

presented by

Ching-Tung Kuo

has been accepted towards fulfillment of the requirements for

Ph.D. degree in ____Chemistry

Date September 16, 1994

MSU is an Affirmative Action/Equal Opportunity Institution

0-12771

LIBRARY Michigan State University

PLACE IN RETURN BOX to remove this checkout from your record. TO AVOID FINES return on or before date due.

DATE DUE	DATE DUE	DATE DUE
		<u> </u>

MSU is An Affirmative Action/Equal Opportunity Institution choirdeadus.pm3-p.1

OPTICAL STUDIES OF ALKALIDES AND ELECTRIDES

bу

Ching-Tung Kuo

A DISSERTATION

Submitted to
Michigan State University
in partial fulfillment of the requirements
for the degree of

DOCTOR OF PHILOSOPHY

Department of Chemistry

ABSTRACT

OPTICAL STUDIES OF ALKALIDES AND ELECTRIDES

b y

Ching-Tung Kuo

A high vacuum system was built for photoemission measurements. The system allows one to load alkalides and electrides under vacuum and at low temperatures with minimum contact with air or moisture. The vacuum of the measuring system can reach better than 10^{-8} torr. The temperature of the sample holder can be controlled to ± 2 °C and cooled down to -130 °C. The 1000-W xenon light source is monochromatized, and light in the range from 200 to 900 nm is used. The response time of the system is ≈ 40 ms, and the gain of the preamplifier is 10^9 . A data acquisition system is employed to control the scanning monochromator and the electrometer, and to record data with respect to wavelength or time.

The quantum yield spectra of the alkalides, K⁺(15C5)₂·K⁻, Rb⁺(15C5)₂·Rb⁻, Na⁺C222·Na⁻, K⁺C222·K⁻, Cs⁺C222·Cs⁻ and K⁺C222·Na⁻, show the common features of main emission peak at an energy higher than 4 eV and a low energy tail, and sometimes the high energy peak has a shoulder on the low energy side and peaks at lower energies. The high energy peak is less temperature dependent

and is assigned as the emission from the valence electrons. The low energy emission strongly depends on temperature and the experimental conditions, and is presumed to be emission of trapped electrons. Photoemission threshold energies were determined, and depend not only on the alkali metal anion but also on the environment in which the anions reside.

Laser pulses had appreciable effects on polycrystalline Na+C222·Na- samples. Most samples of Na+C222·Na- contain both defect sites and defect electrons. As a result, the photoemission spectrum yields an additional shoulder at 360 nm (3.4 eV) and peaks and shoulders in the range of 500 - 700 nm, besides the main emission peak of Na- at 290 nm (≈ 4.3 eV). The 6 ns, high intensity laser pulses result in transient depletion of shallowly trapped electrons and/or occupancy of defect sites, and also lead to apparent modifications of the surface layers. Two kinetic models are developed to explain the mechanisms of the photobleaching effects and population-depopulation of defect electron traps.

In order to study the anisotropic properties of Na⁺C222·Na⁻, nearly-normal incidence reflectivity on various faces of single-crystal Na⁺C222·Na⁻ was measured in the photon energy range 0.5-3.1 eV. The polarization-dependent spectra were determined for the electric field vector parallel and perpendicular to the C axis, based on the orientation-dependent results, known structure and the shapes of the single-crystals. A Kramers-Kronig analysis of the reflectivity yielded the spectral dependence of the real and imaginary parts of the complex dielectric constant and refractive index, as well as the absorption coefficient and the energy loss function. Comparison of

the polarization-dependent spectra permitted identification of the orientation-dependent interband transitions. A peak with energy 1.64 eV appears irregularly, which is presumably due to trapped electrons. The polarization dependence of the spectra provide us with further insight into the nature of anisotropic energy states of Na⁺C222·Na⁻.

ACKNOWLEDGMENTS

I would like to express my appreciation to Dr. James L. Dye for his constant guidance and support during this course of project. I would like to thank Dr. William P. Pratt for his advice on many aspects of this work. I would also like to thank Dr. John L. McCraken for his help in correction of this thesis.

I would also like to thank all the members in Dr. Dye's research group with whom I worked with, in particular Dr. James L. Hendrickson. I would also like to thank Dr. kuo-Lih Tsai for his help in beginning of my synthesis.

I would also like to express my appreciation to electronic specialist Martin Rabb for his help in designing the electronics and in solving electronic problems. I would also like to thank machinist Thomas Palazzola for his help in building the vacuum system. I would like to thank master glassblowers Manfred Langer, Scott Bancroft and Keki Mistry, who built and repaired numerous glass cells for this work.

I am grateful to receive financial support from National Science Foundation grants No. DMR 90-24525.

TABLE OF CONTENTS

		Page
	LE OF CONTENTS	
	OF TABLES	
LIST	OF FIGURES	IX
CHA	PTER I: INTRODUCTION AND BACKGROUND	1
I.A.	Introduction to Alkalides and Electrides	1
I.B.	Trapped Electrons in Frozen Glasses and Optical	
	Photobleaching effects	7
I.C.	Ultraviolet Photoelectron Emission	11
	I.C1. Instruments for Ultraviolet Photoemission	
	Spectroscopy	12
	I.C2. Quantum Yield Spectra and Energy Distribution	
	Curves	18
	I.C3. Work Function	
	I.C4. Direct and Indirect Transitions in Photoemission	27
CHA	PTER II: THE PHOTOEMISSION APPARATUS AND	
PHO	OTOEMISSION STUDIES	32
IIA.	Introduction	32
	Description of the System	
	II.B1. General Aspects of Design	
	II.B2. The Vacuum System	
	II.B3. Temperature Control	
	II.B4. Electronic Systems	
	II.B5. Data Acquisition Methods	42
	II.B6. Optical System	
II.C.	•	
	II.C1. Sample Preparation	
	II.C2. Measurements	
пD	Results and Discussion	50

CHAP	TER III: THE PHOTOELECTRON EMISSION FROM N	Na+C222·Na⁻:
	EFFECTS OF LASER PULSES	75
III.A.	Introduction	75
III.B.	Experimental	79
III.C.	Results	
III.D.		
III.D.		
СНАР	TER IV: REFLECTANCE STUDIES OF SODIUM CRYF	TAND [2.2.2]
	SODIDE	110
IV.A.	Introduction	
	IV.A1. The Kramers-Kronig Relations	115
	IV.A2. The Optical Dispersion Theory	
	IV.A3. Procedure and Approximations for Kran	ners-Kronig
	Applications	119
IV.B.	Experimental	
IV.C.	Results and Discussion	126
IV.D.	Conclusions	146
СНАР	TER V: CONCLUSIONS AND SUGGESTIONS FOR FUR	THER WORK.
V.A.	Conclusions	147
	Suggestions for Further Works	
APPE	ENDIX	152
	RENCES	

LIST OF TABLES

2 1	Page 45
2-1	ASCII codes for the monochromator-computer interface45
2-2	The photoemission threshold energies of the valence
	bands of alkalides and the work functions of the
	corresponding alkali metals62
4-1	Important physical parameters and equations for a
	medium118
4-2	Equations for calculation of the optical constants124
4-3	Polarized and non-polarized studies of Na+C222·Na144

LIST OF FIGURES

	Page Page
1-1	Representative complexants a) 15-crown-5 (15C5) b) cryptand[2.2.2] (C222) c) pentamethylpentacyclen (PMPCY)
1-2.	Comparison of PE spectra: a) the integral form of a spectrum generated by retardation, b) the energy distribution curve spectrum obtained by differentiation of spectrum in a
1-3	The structures of deflection electron energy analyzers: (a) 127 ° cylindrical deflector; (b) electrostatic mirror18
1-4	Schematic representation of the three-step model for the photoemission process
1-5	Effect of band bending on the threshold for photoemission21
1-6	Correction of the binding energy E_{vac}^{B} for metal and nonmetal samples
1-7.	Schematic representations of indirect and direct transitions29
2-1	Schematic view of the photoemission apparatus36
2-2	Block diagram of the photoemission spectrometer38
2-3	The structure of the vertical wand40
2-4	The stabilizing rate and precision of temperature control of the sample holder41
2-5	The circuit of the spectrometer43

2-6	Schematic view of sample loading and transportation49
2-7	Quantum yield spectrum of $K^+(15C5)_2 \cdot K^-$ at -60 °C
2-8	Quantum yield spectrum of Rb ⁺ (15C5) ₂ ·Rb ⁻ at -60 °C
2-9	Photoemission quantum yield spectra of nearly defect-free crystals of Na+C222·Na- at -60°C53
2-10	Quantum yield spectrum of K+C222·K- at -60 °C54
2-11	Quantum yield spectrum of Cs ⁺ C222·Cs ⁻ at -60 °C55
2-12	Quantum yield spectrum of K+C222·Na- at -60 °C56
2-13	Normalized decrease in the photoemission intensity at various wavelengths with changes in temperature for K ⁺ (15C5) ₂ ·K ⁻
2-14	Quantum yield spectrum of K+C222·e ⁻ at -60 °C64
2-15	Quantum yield spectrum of K ⁺ (15C5) ₂ ·e ⁻ at -60 °C65
2-16	Quantum yield spectrum of Cs ⁺ (18C6) ₂ ·e ⁻ at -60 °C
2-17	Quantum yield spectrum of Na+C222·Na- (with trapped electrons present) at -60 °C
2-18	The reduction of the photoemission quantum yield spectrum of Na ⁺ C222·Na ⁻ as a function of the magnetic field71
2-19	The normalized reduction of the photoemission intensity of Na ⁺ C222·Na ⁻ at different wavelengths as a function of the magnetic field72

2-20	at -60 °C
3-1	The photoelectron emission current of Na+C222·Na- at 400 nm and -60 °C versus imposed bias voltage81
3-2	Photoemission quantum yield spectra of a Na ⁺ C222·Na ⁻ polycrystalline sample at -60 °C84
3-3	The response of the photoelectron emission current at -60 °C of a Na ⁺ C222·Na ⁻ polycrystalline thin sample to successive 532 nm laser pulses as analyzed with 400 nm xenon light86
3-4	The response of the photoelectron emission current of a Na ⁺ C222·Na ⁻ polycrystalline thin sample to successive 532 nm laser pulses as analyzed with 600 nm xenon light87
3-5	Growth of the photoelectron emission current of Na+C222·Na-at 600 nm after 532 nm laser pulses at three temperatures88
3-6	Linear dependence of the photoelectron emission current of Nat C222·Na ⁻ (open squares) and of the recovery rate constant (crosses in squares) on the 600 nm xenon light intensity after 532 nm laser pulses.
3-7	(a) Photoemission from Na ⁺ C222·Na ⁻ at 500 nm xenon light and -60 °C after the laser pulse, (b) the combination of the electron emissions at 400 nm and 600 nm after the laser pulses91
3-8	Energy diagram of Na ⁺ C222·Na ⁻ related to photoelectron emission. The solid curve is the excess quantum yield that results from a number of laser pulses with 600 nm xenon analyzing light, plotted versus energy, and is obtained from the data shown in Figure 3-2.

3-9	Na+C222·Na in the absence of laser pulses
3-10	Decay and growth of the photoelectron emission current of Na+C222·Na- after a 532 nm laser pulse at -30 °C with analysis by 600 nm xenon light
3-11	The least-squares fit of three successive photoelectron emission growth signals of Na ⁺ C222·Na ⁻ after 532 nm laser pulses at -60 °C by Equation 3-10, a double exponential function in which the slower rate constant is not adjusted, but is determined from the growth rate prior to laser irradiation
3-12	The effect of 1063 nm weak laser pulses (10 Hz) on the photoelectron emission current of Na+C222·Na- at -60 °C during and after illumination with 400 nm xenon light107
4-1	Contour for the Cauchy Principle Value integral113
4-2	Schematic diagram of the refractive microscope system122
4-3	Reflectance spectra of a single-crystal of Na ⁺ C222·Na ⁻ at ≈ - 60 °C127
4-4	Temperature-dependent reflectance spectra of Na+C222·Na128
4-5	Reflectance spectra of single-crystal Na ⁺ C222·Na ⁻ at ≈ - 60 °C with various small tilt angles of the surface plane
4-6	Near-normal incidence reflectivity of single-crystal Na ⁺ C222·Na ⁻ for \vec{E} // C and $\vec{E} \perp C$ at \approx - 60 °C

4-7	Na+C222·Na-with a thickness of 930 Å at ≈ - 60 °C. (Data of J. E. Hendrickson [86])
4-8	Spectral dependence of the derived extinction coefficient k of single-crystal Na ⁺ C222·Na ⁻ for $\vec{E}/\!\!/ C$ and $\vec{E} \perp C$ at \approx - 60 °C
4-9	Absorption coefficient of single-crystal Na+C222·Na- for $\vec{E} \parallel C$ and $\vec{E} \perp C$ at \approx -60 °C
4-10	Spectral dependence of the real part of the refractive index n of single-crystal Na ⁺ C222·Na ⁻ for $\vec{E}/\!\!/ C$ and $\vec{E} \perp C$ at \approx - 60 °C
4-11	Spectral dependence of the real part of the dielectric function ε_1 of single-crystal Na ⁺ C222·Na ⁻ for $\bar{E}/\!\!/C$ and $\bar{E} \perp C$ at \approx -60 °C
4-12	Spectral dependence of the imaginary part of the dielectric function ε_2 of single-crystal Na ⁺ C222·Na ⁻ for \vec{E} // C and $\vec{E} \perp C$ at \approx -60 °C
4-13	Spectral dependence of the energy loss function, $-\text{Im}(\varepsilon^{-1})$, of single-crystal Na ⁺ C222·Na ⁻ for \vec{E} // C and $\vec{E} \perp C$ at \approx - 60 °C
4-14	Spectral dependence of extinction coefficient k of single-crystal Na ⁺ C222·Na ⁻ at ≈ - 60 °C141
4-15	The spectral dependence of the extinction coefficient of single- crystal Na ⁺ C222·Na ⁻ at ≈ - 60 °C143
4-16	The reflectance spectrum obtained from Kramers-Kronig conversion of the absorption spectrum in Figure 4-7145

CHAPTER I INTRODUCTION AND BACKGROUND

I.A. Introduction to Alkalides and Electrides

Two new classes of compounds, with very special reactions and properties, have been synthesized in Dye's laboratory and named alkalides and electrides. The general formula for alkalides is $M^+C\cdot M^-$; the stable alkali metal cations, M⁺, are complexed and caged in macrocyclic molecules represented here by C, whereas the counterions, M⁻, can be stable and exist outside the cage to balance the charges. The metal cation and anion in a compound can be the same element or can be different. If they are different, the electron affinity of the anionic element and the complexation constant of that which forms the cation will determine the direction of charge transfer. Electrides have the general formula M+C·e-, where the electrons serve as anions to balance the positive charges. macrocyclic complexants that have been used are cryp[tands, crown ethers, and more recently, the aza- based cryptands and cyclens. Examples of these complexants are shown in Fig. 1-1.

The synthesis and study of alkalides and electrides has been continuing for the past twenty years. Since 1974, more than 30 alkalides and 5 electrides have been synthesized and characterized. The first crystalline alkalide was Na⁺C222·Na⁻, which was crystallized from amine solutions that contained sodium and cryptand[2.2.2] (C222) [1]. Although many alkalides and electrides have been

synthesized in Dye's laboratory, Na+C222·Na- is still the most stable and the one that has been most thoroughly characterized [2-4]. The first crystalline electride is Cs+(18C6)₂e- which is formed by carefully controlling the 1:2 stoichiometric ratio of cesium to crown ether, 18C6. In this electride, the electron e- apparently resides in the otherwise empty anion cavity.[5] That is, the electron density is centered in this cavity although some electron density undoubtedly spreads onto the surrounding complexant molecules.

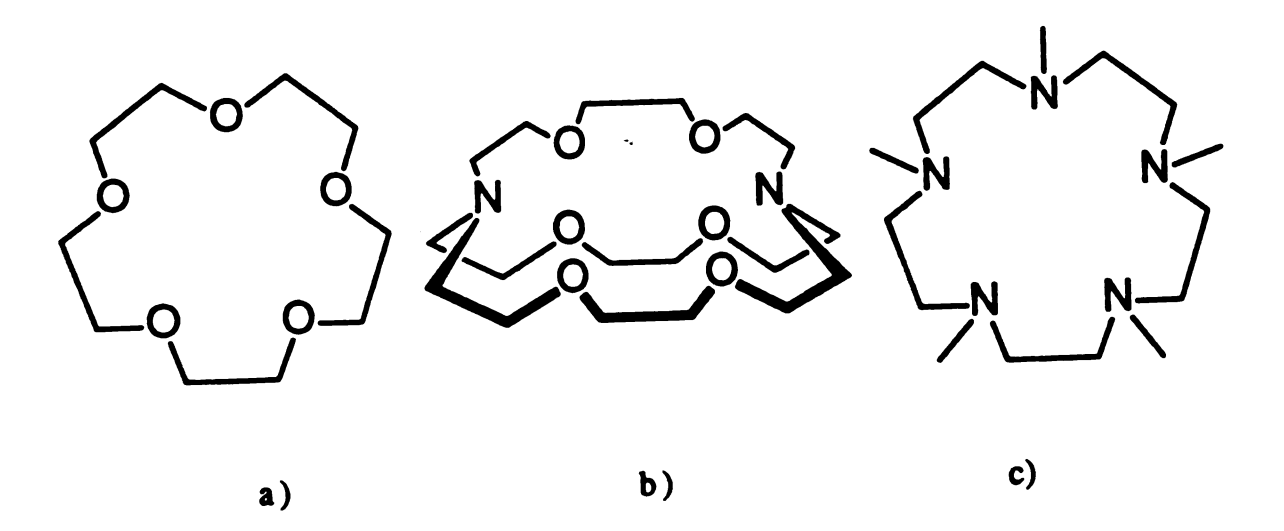


Figure 1-1. Representative complexants a) 15-crown-5 (15C5) b) cryptand[2.2.2] (C222) c) pentamethylpentacyclen (PMPCY).

Syntheses of alkalides and electrides are quite straightforward because the experiences and procedures have been well established [8]. The main technique for the synthesis is that the reaction and crystallization have to be carried out under vacuum at low temperature. The procedures can be generalized by several steps. First, a proper ratio of alkali metal and complexant are introduced

into the reaction cell in a helium glove box, then the metal is evaporated to form a mirror to increase the reaction surface. A well purified solvent such as methylamine or dimethylether is added as the first solvent. Trimethylamine or diethylether is then used as the second solvent to reduce the solubility of the complex, M+C·M- or M+C·e-. The crystal product can be obtained by precipitation from a saturated solution by either slow removal of the more volatile and more polar solvent or slow-cooling of the whole system. The details for the syntheses have been described in the references [6,7].

The alkalides and electrides are sensitive to decomposition by air, moisture or elevated temperatures, so they have to be handled and stored at low temperatures and in an inert or vacuum environment. In spite of these restrictions, their physical characteristics have been examined by various methods; among these are the optical, EPR and NMR spectra, conductivity and magnetic susceptibility.

The EPR method provides opportunities for detecting both the existence of trapped electrons and the environment of the trapping sites. For example, if the cations are well-shielded within a cryptand cage or a crown ether sandwich, there is no hyperfine splitting in the EPR spectrum. This results from the weak interactions between the trapped electrons and many surrounding cations. But when the cation forms an ion-pair with the anion, then the hyperfine coupling to a single cation becomes appreciable. For example, the well-resolved EPR spectra of K⁺(18C6)·Na⁻ and Rb⁺(18C6)·Na⁻ show hyperfine splittings indicating the presence of ion-pairs, M⁺·Na⁻, in these compounds [8].

In early studies of alkalides, the NMR method was used to identify the presence of the species M⁺ and M⁻, based on the interpretation of the chemical shift behavior. For example, the ²³Na NMR spectrum of Na⁺(C222)·Na⁻ in solution has the same chemical shifts of Na⁺ and Na⁻ as the MAS solid state spectrum of the polycrystalline sample [9,10]. The spectrum of Cs⁺(18C6)₂·Na⁻ only shows the peaks of Cs⁺ and Na⁻, which means that this is the right formula instead of a mixture of ceside and sodide [11]. Later, the NMR method was extended to study the nature of electron-trapping in electrides and the temperature effects of phase transitions and structural disorder [12].

The electrical conductivities of all alkalides have an exponential dependence on 1/T that makes the alkalides behave as apparent semiconductors, where T is the temperature. However, the band gap obtained is generally too low and is dependent on the preparation, meaning that the conductivity is extrinsic instead of intrinsic, and is due to the presence of trapped electrons with energy states in the gap [13]. The only alkalide which can be crystallized nearly free of defect electrons is Na⁺C222·Na⁻, which has a band gap of 2.4 eV, obtained from both powder and two-probe single crystal measurements [2]. Conductivity measurements of the electrides, $Cs^+(18C6)_2 \cdot e^-$ and $Cs^+(15C5)_2 \cdot e^-$, showed that, in addition to defect electronic conductivity, cationic conductivity is present. The transport process is referred as a Cs-Cs⁺ exchange, and the cesium cation was apparently reduced to metal and deposited on the cathode [14]. The electride K+C222·e⁻ has a much higher conductivity ($\approx 10^{10}$

times higher) which may be due to the "chained" dimer electrons along with the channel vacancies [16].

Temperature-dependent magnetic susceptibility measurements provide very useful information regarding the interelectron interactions. For example, both the electrides Cs+(15C5)₂·e-and Cs+(18C6)₂·e-have antiferromagnetic properties whose Neel temperatures are dependent on the annealing history. The phenomenon was interpreted as being due to the movement of the complexant molecules to block the channels, or to the presence of Cs-, which decreases the electron-electron interactions [15]. The magnetic susceptibility of K+(C222)·K- changed with an increase in temperature from essentially diamagnetic to partially paramagnetic, which was interpreted as due to a thermally populated triplet state lying 0.03 to 0.05 eV above the ground state at 200 K [16].

The most extensive studies applied to the alkalides and electrides are optical methods. In the earlier studies only the absorption spectra of thin films was measured; later, other optical techniques, such as photoluminescence [4,17], photoemission [18], and reflectance [19] were adopted to study solid samples. The absorption spectra revealed information on the energies of bandband and/or band-continuum transitions for the metal anions, M^- , which led to the identification of the absorbing species by comparing the absorption spectra of both solutions and polycrystalline films. The ground state of the metal anion, M^- , is ns^2 , which constitutes the valence band. The band-band and the band-continuum transitions are presumed to be $ns^2 \to nsnp$ and $ns^2 \to continuum$, respectively. The $ns^2 \to nsnp$ transitions of M^- in $M^+C222 \cdot M^-$ films are at 650,

840, 860 and 950 nm for Na-, K-, Rb- and Cs-, respectively [3]. $ns^2 \rightarrow continuum transition of Na^+C222 \cdot Na^- polycrystalline films$ appears as a shoulder in the spectrum at 500 -550 nm (≈2.3 eV). A small high energy peak is also present at 400 nm (3.1 eV) with a fixed intensity ratio with respect to the main peak, and it has the same direction of shifts as the main peak following a change of temperature. The species has not been identified, but may be due to the transition from the valence band to the vacuum level. The optical absorption of electride films showed the presence of two classes, which are called "localized" and "delocalized". Most electrides have a distinct absorption peak in the near infrared region that results from the localization of trapped electrons. However, the absorption spectrum of K+C222·e- has a characteristic "plasma edge", which is similar to that of concentrated liquid solutions of Na in In such spectra, the absorbance increases throughout the ammonia. visible towards the infrared and remains high in the infrared. electrons in K⁺C222·e⁻ are suggested to be somewhat delocalized, due to the overlap of the wave functions of trapped electrons with adjacent trapped electrons. But the presence of partial localization or grain-boundary effects could be the source of activated conductivity rather than true metallic behavior.

A short laser pulse on the alkalides is able to produce luminescence [17]. The luminescence spectra were temperature dependent, giving red shifts with an increase in the temperature; also, the intensities dramatically decreased as the temperature increased. The quantum yields were affected by the amount of defect trapped electrons in the samples; samples with fewer defects

had higher yields. For Na⁺C222·Na⁻, the fluorescence peak position varied with temperature from 1.854 eV at 7 K to 1.828 eV at 80 K [4], when it was illuminated by a 50 picosecond dye laser with energies between 2.2 and 2.0 eV. The time-resolved spectra were deconvoluted by fitting with a double exponential, and a simple picture of the emission suggested that the emissions were from at least two closely spaced levels. The short-time emission was from the bottom of the p-band, where electrons could further relax with the surrounding charges to a lower excited level, from which there was long-time emission. However, this simple picture could not completely describe the time-dependent spectra and short-time rate constant.

I.B. Trapped Electrons in Frozen Glasses and Optical Photobleaching effects

Free electrons can be liberated by the impact of high energy electrons or by ionizing radiation, γ-rays or x-rays in glassy solids at various cryogenic temperatures. They can be chemically stabilized in trapped states in the frozen matrix. Such trapped electrons have been observed in various frozen organic and aqueous liquids such as alcohols, ethers, amines, alkenes alkanes and alkali aqueous solutions. The aqueous ices contain trace amount of solutes, such as sodium salts or N, N, N', N'-tetramethyl-p-phenylenediamine (TMPD) [20], and the trapped electrons are formed by photoionization of the solutes. However, significant yields of trapped electrons have not been found in pure crystalline samples of the solvent. The frozen

liquids are in amorphous states, formed by rapidly quenching the samples with liquid nitrogen or liquid helium, and apparently contain defect sites at which the electrons can be trapped.

Electron spin resonance and optical absorption spectrometry are the most common methods used to detect the trapped electrons Other evidence for trapped electrons was found in (e_t^-) . luminescence, electrical conductivity, and differential thermal analysis studies [21]. The optical absorption spectra of the organic and aqueous ice glasses that contain trapped electrons are broad, and extend from the visible or near infrared to the IR region. absorption peaks have a long high-energy "tail" and a short lowenergy side, and they were suggested to have been composed of individual electrons in different trap depths; where the red end of the spectrum of each e_t is the photoionization threshold for the trap and the blue side of the maximum is the energy required to move the electron far enough to react with a cation or a radical rather than being retrapped [22]. The spectra of e_t in the frozen glasses are similar to those in the respective liquids, but the former are narrowed and blue shifted; this suggests that the nature of trapped electrons is similar in liquids and glasses, but that the trapped electrons in the glasses are more stabilized [23].

The electrons in the trapping sites can be thermalized into more stable states. The stabilizing mechanisms suggested were that they are first weakly trapped in the matrix of molecules through dipole interactions, which then induces a rearrangement of the molecules around them, and the traps deepen as the arrangements of molecules achieve equilibrium. This explained the broad absorption

bands as due to the electrons occupying a continuum of trap depths. The above suggestion was verified by the facts that the spectra of etproduced in organic glasses are not stable, but undergo a continual blue shift with time after production, which can be as long as 380 seconds [24]. This indicates that the electrons deepened in the traps after a sufficiently long period of time.

A convincing piece of evidence to prove that the trapped electrons, e_t⁻, are distributed in a continuum of trap depths rather than being in the same depth of traps, is the reversible partial photobleaching of the blue side of spectra accompanied by the enhancement of the red side. The most conclusive evidence is the selective bleaching effects on the absorption spectra of 2-methyltetrahydrofuran (MTHF), 3-methylpentane (3PM) and C2H5OH glasses at selective wavelengths when monochromatic bleaching light is used. For example, the bleaching effects of e_t⁻ occur in MTHF only in the range from 1200 to 1550 nm when monochromatized light of 1338 nm wavelength is used [25].

Photobleaching effects showed that the trapped electrons in hydrocarbon glasses can be detrapped by a monophotonic process at all wavelengths of their absorption spectra, from far on the low energy side (2500 nm) to far on the high energy side (400 nm) [25,26]. This implies that the photon energy absorbed by the trapped electrons can raise the electrons to the quasi-free state in the glassy matrix. But not every electron that absorbs a photon is activated enough to react with the radical or cation, since the quantum yield of bleaching at wavelengths on the red side is low, and increases with photon energy. In the slightly more polar matrix,

MTHF, the absorption maximum is at 1200 nm, and monophotonic bleaching occurs up to about 1200 nm but not at wavelengths longer than that. This implies that the energy given to the electrons by the longer wavelengths is lower than that necessary to reach the quasifree state and is insufficient to prevent the subsequent prompt return to the oriented coulomb well of the parent trap or the formation of a new trap without appreciable migration. A plot of the photon energy maximum (λ_m) versus the static dielectric constant (D_S) of the matrix compound forms a smooth curve, which suggests that the trap depths increase with an increase in molecular polarities [25].

The EPR spectra of trapped electrons is a broad Gaussian line resulting from hyperfine interactions with a g value near the free electron value. The line widths of EPR spectra of the trapped electrons in glasses at 77 K generally broaden with increasing polarity of the matrix molecules. This indicates increased hyperfine interactions with the atoms in the walls as the traps become deeper [23], due to the structure change or relaxation effect. The EPR spectrum also contains information about the orientation of molecules around the trapped electrons. For example, the EPR singlet in deuterium-substituted alcohol C₂H₅OD is narrower than that in C₂H₅OH by the ratio approximately expected if the hyperfine coupling with deuteriums replaces that with protons. Apparently the hydroxyl groups in the trapping walls align toward the trapped electrons [27, 28]. Electron spin echo studies or ENDOR, can be used to obtain more detailed quantitative information about electron locales. The spectrum shows a hyperfine splitting pattern which is related to the structural information about the solvation shell of a localized electron. The solvation structure of the electron in a variety of solvents has been elucidated in this way [29].

The spontaneous removal of trapped electrons occurs by combination with cations, radicals or the additives of aqueous ices. Half-lives are on the order of tens of minutes near the glass transition temperature for organic glasses and alkaline ices. The rate increases with a rise in temperature. Possible mechanisms of electron migration include: (1) diffusion of e_t —coupled with its surrounding shell molecules; (2) diffusion of e_t —without the movement of surrounding molecules, only the polarity passing to the new molecules as e_t —; and (3) quantum tunneling to a radical, cation or an added scavenger with greater electron affinity than the trap. In the third suggested mechanism, the thermal detrapping and movement to a reaction partner by a hopping mechanism seems improbable, since the detrapping thresholds are larger than 0.5 eV and the kT is only 0.006 eV at 77 K [22].

I.C. Ultraviolet Photoelectron Emission

The first photoelectric effect was observed by Hertz [30] in 1887. He found that a spark between two electrodes occurs more easily when the negative electrode is illuminated by ultraviolet light. The effects were interpreted by Einstein [31] in 1905 by quantum mechanics, which led to the establishment of the foundations of the quantum theory of radiation. In the 1950s, the understanding of the band structures of solid samples particularly enhanced the

knowledge about the microscopic basis of photoemission. Many theories have been developed since then.

Photoelectron emission (PEE) from a solid provides less ambiguous information about the nature of electron transitions than does the optical absorption spectrum. The electronic transition in PEE is absolute, in that only final states whose energies are higher than the vacuum level contribute to the spectrum. By contrast, the absorption transition occurs relatively; that is, the electronic transition takes place only when the energy difference between the final state and the initial state corresponds to the selection rule. Therefore, the photoelectron spectrum formed by populating a given set of final states indicates the absolute energies of the initial electron states.

The alkalides and electrides have unusual properties as introduced previously; they would be excellent candidates for photoemission studies of the energy state of the alkali anion outer shell (ns²) electrons, and those of any trapped electrons in the sample.

The nature of the instruments used, and the principles of work function measurements, optical transitions and the photoemission spectra will be introduced in this chapter because they include most of the important background information needed to understand photoemission.

I.C1. Instruments for Ultraviolet Photoemission Spectroscopy

Photoemission spectroscopy can be divided into two categories: ultraviolet photoemission (UPS) and X-ray photoemission (XPS). The former is mainly for the study of the energy states of valence electrons and energy bands in a solid; the latter is primarily for probing energy levels of core electrons, although it can be used at lower resolution to study the valence band. For the alkalides and electrides, only the energies of the valence band and states above it are of direct interest to us, so this introductory chapter will limit its scope to ultraviolet photoemission.

An ultraviolet photoemission spectrometer is composed of three major parts; light sources, vacuum chambers and electron energy detectors. In the early 1960s, conventional light sources, such as mercury arcs and tungsten lamps, etc., together with a conventional monochromator, were used [32][33]. The available photon energies were under 6 eV, which limited the applications because the work functions of most materials are at least 3 to 5 electron volts [34]. In the late 60s, obtaining higher energy photon sources became more important. With the development of vacuum techniques, some higher energy photon sources could be applied. The vacuum UV photon source was first introduced by Spencer [35]. in which a hydrogen lamp was separated from the vacuum chamber by an LiF window. Currently, the most common photon sources are the discrete He(I) line at 21.2 eV and He(II) line at 40.8 eV [36]. The HeI radiation arises from the transition 2p-2s of the neutral He atom, and the He(II) line is from a singly ionized atom. Both line widths are only a few milli-electron volts (meV). Although the line widths can be broadened by experimental conditions such as the selfabsorption effect, the changes usually are quite minor. There are two other source lines from Ne at 16.8 and 26.9 eV. They are not as commonly used as the He lines, but sometimes are convenient when one wants to follow the changes of solid sample cross-sections with photon energy.

The most common UV lamp is the cold cathode discharge tube, which has a double differential pumping stage to limit the gas flow into the sample chamber when a solid sample is measured. When a gas sample is measured, the double differential pumping is unnecessary. The discharge chamber is confined by a quartz tube of ~ 1 mm bore which determines the dimensions of the light that is shone on the sample.

Due to the fact that the cross-sections of different atomic subshells change as a function of the photon energy [37], synchrotron radiation has become an ideal light source, since it has the property of a high intensity monochromatized source of continuously tunable energy. The synchrotron radiation is polarized in the plane of the electron orbital, so it is very effective in determining the orientations of surface states such as surface plasmons, surface-bonded molecules, etc.. However, only radiation sources from a storage ring, rather than an ordinary synchrotron, are suitable for this application because the radiation emitted from the storage ring is continuous, whereas the pulsed radiation from an ordinary synchrotron can't be used as a photon source in photoemission spectroscopy. A storage ring with a 10⁷ (Hz) r.f. power source can repeatedly top up the electron beam current to account for losses by radiation emission [38].

A good vacuum system in the photoemission spectrometer fulfills two basic functions. First, emitted electrons can pass from the surface of samples through the vacuum toward the electron detectors without making too many collisions with residual gases. A moderate vacuum of 10⁻⁵ torr would satisfy this requirement. Such a pressure is actually the operating vacuum in an energy analyzer for the measurement of gas samples. Second, a good vacuum environment can keep the solid surfaces clean. Theoretically, a solid surface will be covered by a monolayer of gas every second at a pressure of 10⁻⁶ torr, assuming a sticking probability of 1 for the solid surface studied. For routine analysis, a vacuum of 10⁻⁹ torr is a compromise between the pumping time and surface cleanliness. Some experiments, especially for fundamental surface studies such as the changes of surface states with the absorption of molecules, require more restricted conditions in that the vacuum must be 10⁻¹⁰ torr or even higher [39].

The electron detection systems consist of electron energy analyzers and detectors. The function of an electron analyzer is to measure the energy distribution of electrons emitted from a sample. The energy analyzer is divided into two categories, according to the methods used to separate electrons with different energies. These are potential retarding fields and deflection fields. The retarding field energy analyzer is essentially a high pass energy filter; only electrons with kinetic energies that surpass the height of the potential barrier can reach the detector. The spectrum observed is the current reaching the collector upon scanning decrements of the retarding potential (Figure 1-2). The energy distribution curve then

is obtained by either electrical or numerical differentiation of the spectrum [40].

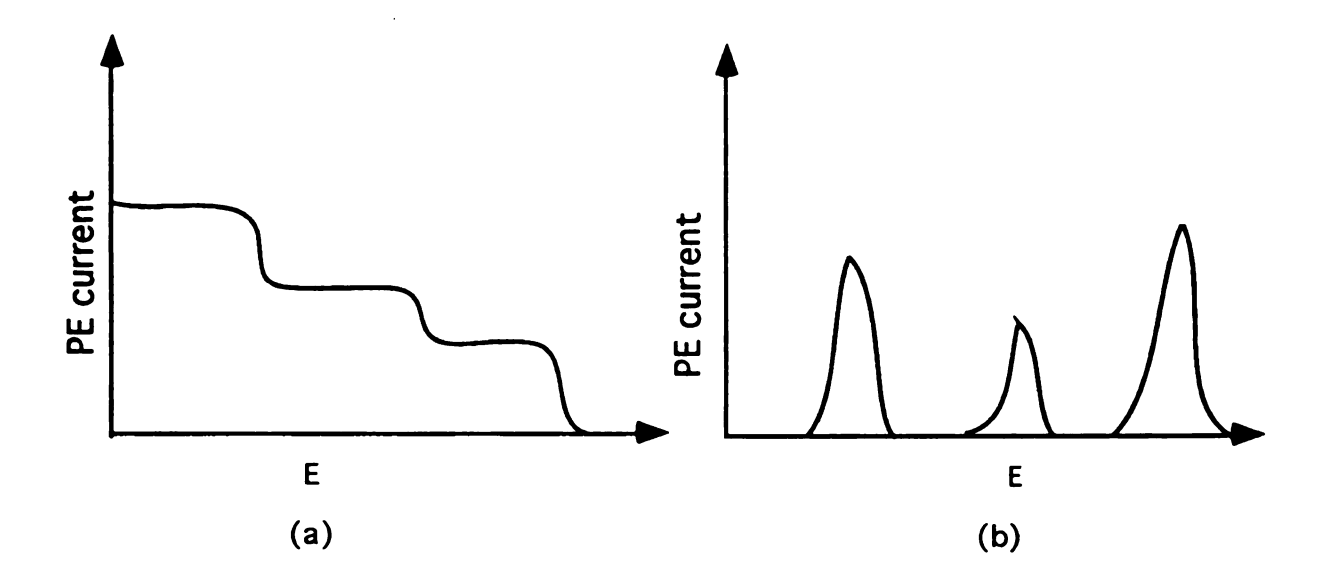


Figure 1-2. Comparison of PEE spectra: a) the integral form of spectrum generated by retardation, b) the energy distribution curve spectrum obtained by differentiation of the spectrum in a.

The retarding field analyzers are somewhat limited in resolution. First, the barrier heights of the retarding potentials are not actually a measure of the total kinetic energies of the electrons, but rather of the momenta. If one electron approaches the retarding grid at the angle, θ , only the velocity component normal to the grid is effective in surmounting the retarding potential. The electron with energy $E = \frac{1}{2}mV^2$ will be retarded when the retarding potential reaches a value $V_R = \frac{1}{2}m(V\sin\theta)^2$. The angular spread will result in energy aberration, which will be greatest when the electrons approach the grid at grazing incidence. A spherical retarding grid

with a sample in the center minimizes the energy aberration effect. Second, perfect equipotential is not actually produced when a retarding potential is applied to a wire mesh grid. The field spills out into each mesh hole like a meniscus electrostatic lens, which also degrades the resolution. Third, the increments of stepped signals at lower retarding potentials also increase the background levels and the noise associated with the magnitude of the background level. Background levels are the total current detected instead of just the signal in each step. Therefore, the result leads to a poor signal-to-noise ratio on the low kinetic energy side of the spectrum.

Deflection analyzers are subdivided into two different types, magnetic deflection analyzers and electrostatic deflection analyzers. Magnetic deflection analyzers are not common, due to the difficulties in controlling low magnetic fields for low energy electrons (in UPS) and in canceling external magnetic fields.

Electrostatic analyzers are more easily screened from external magnetic fields, and are now universally used. The magnetic shielding is normally made from material of high magnetic susceptibility, such as mu-metal or the combinations of mu-metal and current-carrying coils. There are two types of deflection electron energy analyzers (Figure 1-3). One is usually referred to as a deflector or condenser, where electrons essentially travel along the equipotential lines; the other is the electrostatic mirror, in which electrons move across the equipotential lines where a gradient of potential is established between two parallel plates. The detectors for the deflection fields are electron mulitipliers [41].

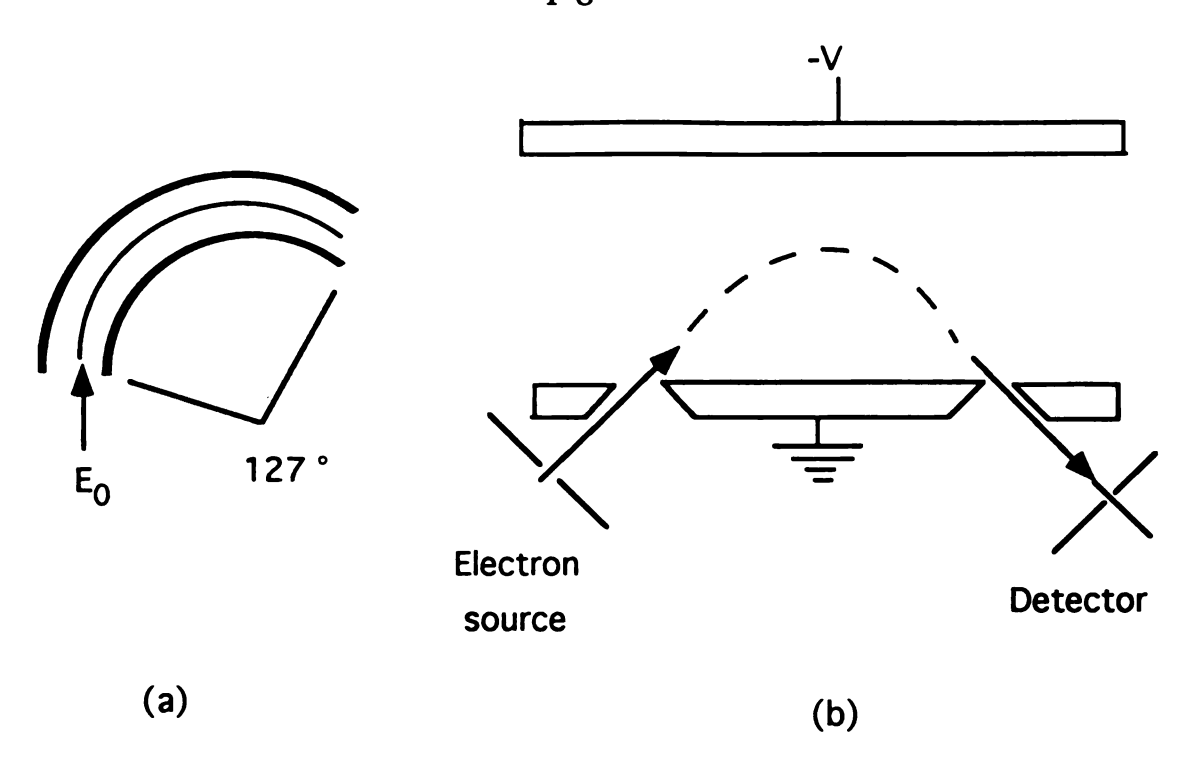


Figure 1-3. The structures of deflection electron energy analyzers: (a) 127 ° cylindrical deflector; (b) electrostatic mirror.

I.C2. Quantum Yield Spectra and Energy Distribution Curves

The simplest form of photoelectron spectroscopy is the quantum yield spectrum, in which the total flux of photoelectrons is measured as a function of the energy of the incident photon. The sample is held in or on a photo cathode with an applied electric field which accelerates the electrons toward the anode with a high enough voltage to give a saturation current. The anode is usually set to virtual ground potential, and the cathode has a negative bias.

Photoemission normally is a volume process, and the electron excitation is suggested as a three-step model [42][43]. First, the

optical excitation of electrons occurs at a distance from the surface, where the excitation corresponds to the electronic structure of the solid. Second, the excited electrons must travel through the crystal to the surface. Scattering occurs during such transport, due to electron-phonon and/or electron-electron interactions. Third, the excited electrons finally escape over the surface barrier into the vacuum (as illustrated in Figure 1-4).

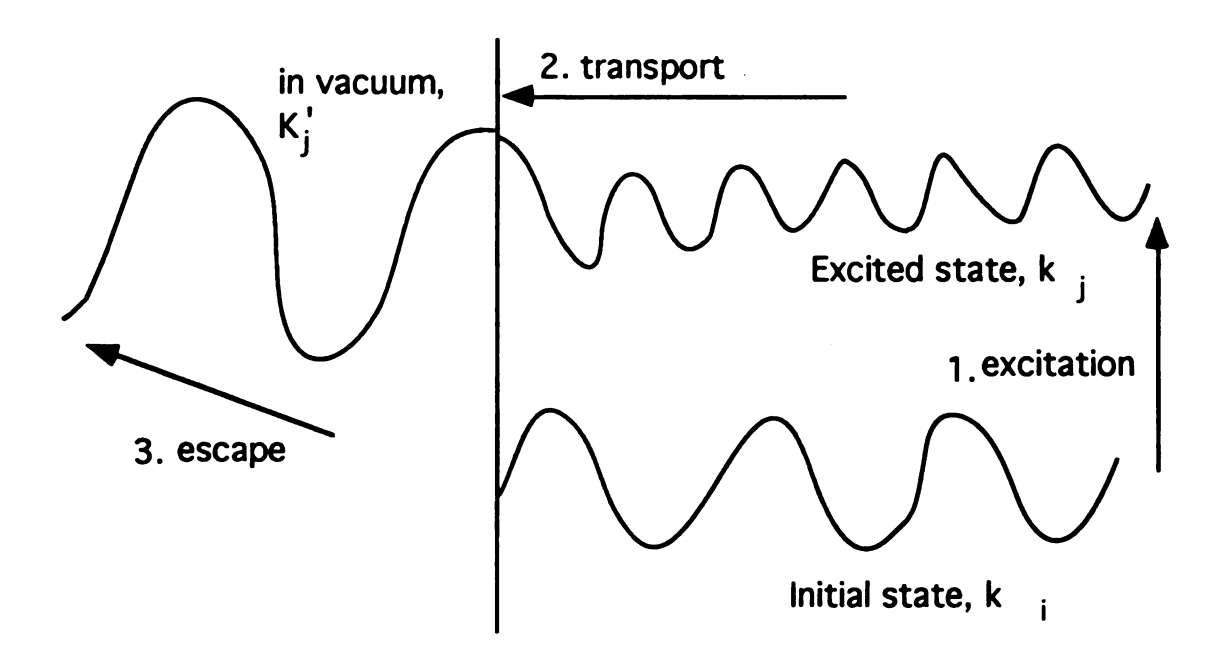


Figure 1-4. Schematic representation of the three-step model for the photoemission process: 1) electrons in the initial state $|k_i\rangle$; 2) electrons photoexcited to the final state $|k_j\rangle$; and 3) electrons photoemitted into the vacuum and coupled with some plane wave state, k_j '.

Based on this model, the spectral dependence of the yield per incident photon for a solid was derived as

$$Y(E) = A(E) \frac{\left\{ \left[\alpha_{PE}(E) \right] / \left[\alpha(E) \right] \right\}}{1 + \left[1 / \alpha(E) L(E) \right]} , \qquad (1-1)$$

where A(E) is the escape function that describes the probability of an electron emitted via the surface, and L(E) is the mean free path of an electron of energy E. The absorption coefficient, $\alpha(E)$, is divided into two parts: the absorption coefficients for transitions above the vacuum level, $\alpha_{PE}(E)$, and below the vacuum level, $\alpha_{C}(E)$ [43].

If the mean free path is large, the major contributions to the quantum yield spectrum are from electrons that originate in the bulk because the number of the surface states is small compared to the total number of participating bulk states. However, the contributions to the spectrum caused by the electrons excited directly from the surface states is also important. A theory developed by Kane [44] shows that the photoemission threshold of a semiconductor can be characterized by a dependence of the form

$$Y = A(hv - E_T)', (1-2)$$

where Y is photoemission quantum yield, A is a constant, r is predicted by the model of the transition that produces energetic electrons and the scattering processes. For example, the power order r is 1 and 5/2 for direct and indirect transitions in bulk processes, respectively.

The surface barrier is an extension of the electron wave functions beyond the positive ion cores. Therefore, the barrier

hei; plai

to

and

stat

dov

Fig pho AE inc do AE by

sili

heights, hence the thresholds, are different for different crystal planes of a material. The surface electron distribution is so sensitive to the surface condition that structural change, absorbed molecules and external fields will cause severe changes. Therefore, surface states often induce a surface charge that bends the band either up or down near the surface.

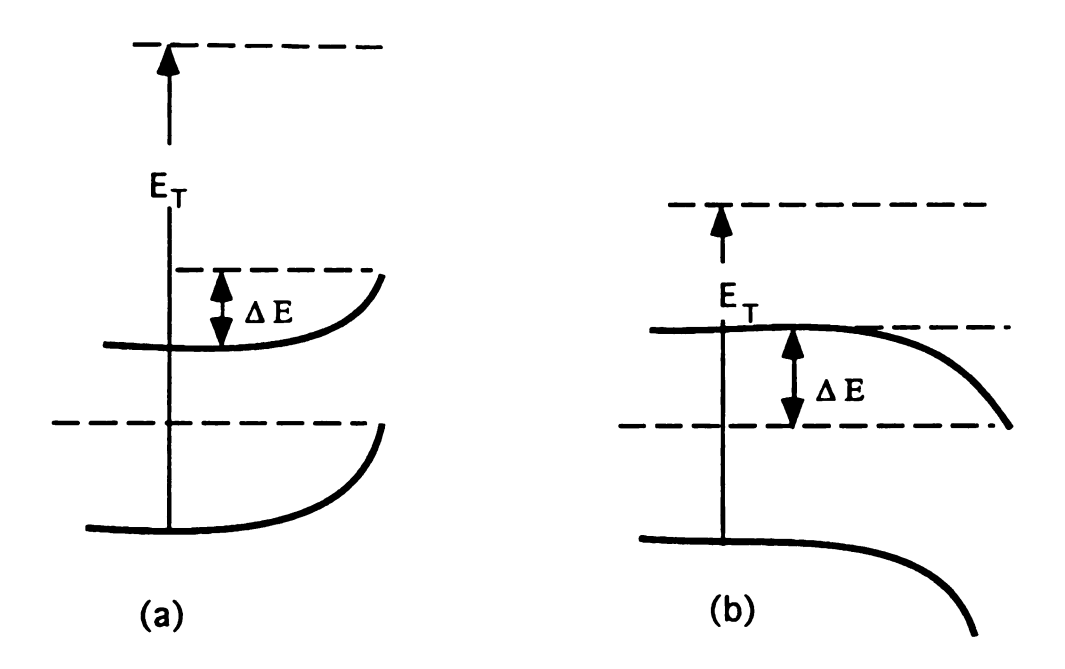


Figure 1-5. Effect of band bending on the threshold for photoemission: (a) for a n-type semiconductor the bands bend up by ΔE , and the photoemission threshold for excitation from the bulk is increased by ΔE ; (b) for a p-type semiconductor, the bands bend down by ΔE , and the threshold emission from the bulk decreases by ΔE . The electron affinity at the surface is assumed not to be changed by the bending.

When Gobeli and Allen studied the photoemission from cleaved silicon (111) plane [45], they observed that the spectra were

dependent on the sample dopings, and they interpreted this as being due to the volume excitation process modified by surface charge band bending. For a material with p-type degenerate-doping, the bands bend down, and the surface inversion layer will lower the photoemission threshold for emission from the bulk. On the contrary, for a n-type degenerately doped material, the bands bend up at the surface, which will cause an increase of the photoemission threshold from the bulk (Figure 1-5) [46].

I.C3. Work Function

Determining the characteristics of various materials is a major task in a photoemission study. The work function of, is the strength of the potential barrier that prevents the valence electrons from escaping from the surface of the solid. It is defined as the difference between the potential immediately outside the solid surface (vacuum level) and the Fermi energy in the solid. In a metal at 0 K, the highest energy electrons are at the Fermi level; in a semiconductor or insulator, the Fermi level usually lies within the forbidden gap, defined as the energy difference between the top of valence band and the bottom of the conduction band. In general, there are two types of methods for determination of the work function: one is the contact potential, which is the energy transfer of electrons from one metal to another. Another is the escape of electrons from a solid surface, which includes photoemission, thermionic and field emission. Different methods and experimental conditions can lead to widespread difference in the results, which usually depend on the

surface conditions. Our research has focused on the photoemission method.

The determination of the work function of a metal by photoemission, can be either by the lowest frequency of light at which photoemission occurs or by the highest electron energy for a given exciting photon. However, the thresholds are usually not sharp, which is due to either the spread in the Fermi distribution at high temperatures which permits photoemission for $h\nu < \Phi$ or to the measurement of photoemission from polycrystalline materials. The measurements from polycrystalline sample may yield different average work functions, and even the results from a single-crystal surface can be distorted by the presence of exposed patches of other orientation faces.

In photoemission, when a metal sample is electrically connected to the collector of the spectrometer, there always exists a small electric field between them due to the difference in work function of the sample and the collector, where the sample metal and spectrometer have the same potential at the Fermi level. If the spectrometer collector has a higher work function than the metal sample, then the electrons leaving the sample will be retarded by the electric field existing between the sample and the spectrometer collector. In a quantum yield spectrum with no bias voltage, the measured work function is for the collector instead for the metal sample. Therefore a compensating bias voltage is needed to extract the emitted electrons to obtain the correct work function. In an energy distribution curve (EDC) the measured kinetic energy E_{kin} will

be lower than the true kinetic energy by an amount $(\phi_{sp} - \phi_s)$ (Figure 1-6).

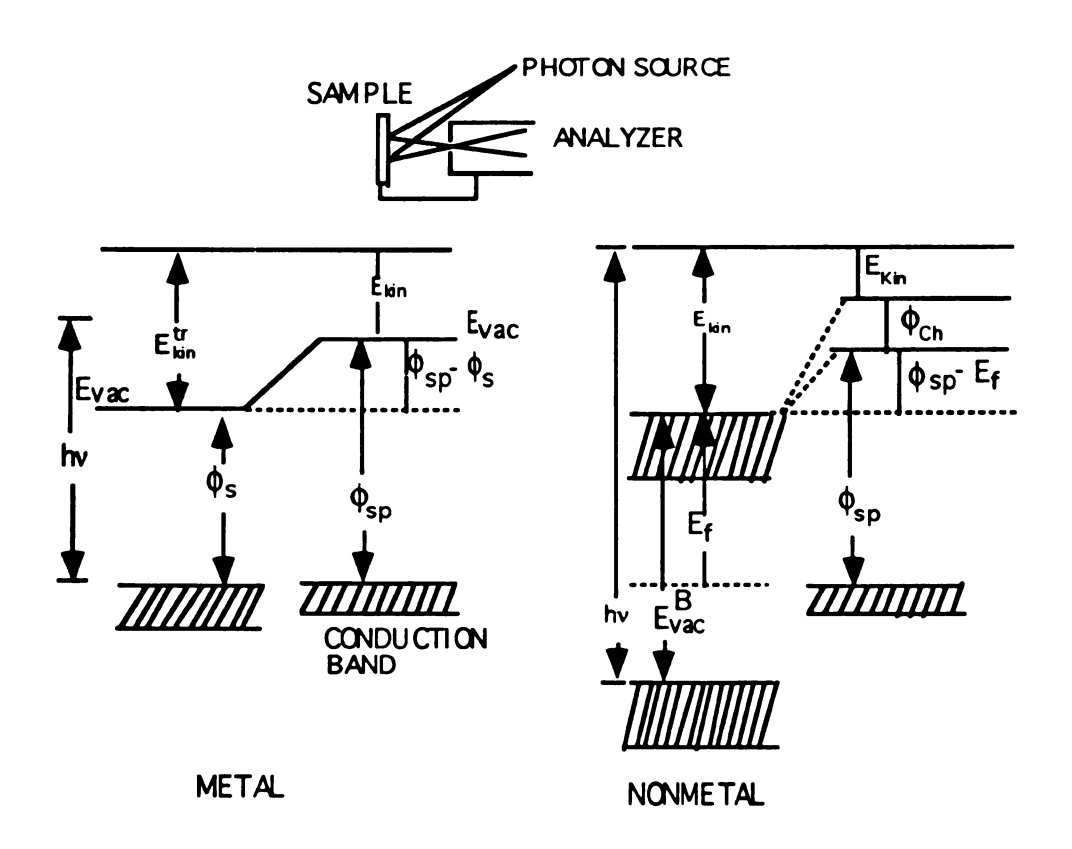


Figure 1-6. Correction of the binding energy E_{vac}^{B} for metal and nonmetal samples: (a) if a metal has lower work function than that of the spectrometer, the binding energy has to be corrected as $E_{vac}^{B} = hv - E_{kin} - (\phi_{sp} - \phi_{s})$; (b) the binding energy of a nonmetal has to be corrected with respect to both the work function difference and the surface charge on the sample, $E_{vac}^{B} = hv - E_{kin} - (\phi_{sp} - E_{f}) - \phi_{ch}$.

The binding energy, with respect to the vacuum level, has to be corrected by the difference

$$E_{vac}^{B} = hv - E_{kin} - (\phi_{sn} - \phi_{s}) \tag{1-3}$$

where the hv is the photon energy.

In insulators and semiconductors, the correction term for the difference of the work function is $(\phi_{sp}-E_f)$ where E_f is the energy from Fermi level to the vacuum for the sample. In addition, when the electrons leave the sample, there is a positive surface charge existing on the sample due to the lack of good conductance. The surface charge will decelerate the emitted electrons, and the amount of energy lost equals the surface charge; therefore, the binding energy with respect to the vacuum level is

$$E_{vac}^{B} = hv - E_{kin} - (\phi_{sp} - E_{f}) - \phi_{ch}$$
 (1-4)

where ϕ_{ch} is the surface charge. Because it is difficult to determine the work function or binding energy with respect to the vacuum level for insulators or semiconductors, an alternative measurement is the threshold energy E_T which is the energy difference from the top of the valence band to the vacuum level [47][48].

Fowler[49] developed a theory to accurately determine the work function for metals by fitting the tail into the theory. He explained that the causes for broadening are the results of the diminishing number of electrons with sufficient energy to overcome the work function as the electron approaches the vacuum, and changes in the band structure resulting from the temperature effect. The latter factor is not very important to the broadening; the former is related to the concept of the conservation of linear momentum

parallel to the surface. He developed a data analysis method to extract the work function ø from the temperature-dependent spectral quantum yield and also from the energy distribution curve. The equation derived from momentum conservation is

$$\log\left(\frac{j}{T^2}\right) = B + \log f\left(\frac{h\nu - \phi}{kT}\right) \tag{1-5}$$

where j is the photocurrent, f is a tabulated function, B is a constant independent of v and T, and ϕ is the work function. The plot of $\log(\frac{j}{T^2})$ vs $\frac{hv}{kT}$ is called the Fowler plot; the horizontal shift yields the work function while the vertical shift gives the constant B. Although these results were derived carefully, they were only rough approximations when compared to more recent data because of the poor vacuum conditions used in earlier experiments.

Temperature-dependent studies are usually plagued by changes in surface condition with temperature. It is nearly impossible to avoid contamination of the surface as the temperature is lowered. For a theoretical temperature study, it is customary to express the temperature dependence of the work function as [50]

$$\frac{d\phi}{dT} = 3\alpha \left(\frac{\partial \phi}{\partial \ln V}\right)_T + \left(\frac{\partial \phi}{\partial T}\right)_V \tag{1-6}$$

in which α is the expansion coefficient. The first term on the right-hand side is the volume dependent term, while the second term is the explicit form of the temperature dependence. The volume dependent term is a function with dipole moment dependence; the

temperature dependent term is related to the change in the ionic charge induced by vibrational changes. These two terms have contributions with opposite signs; therefore they almost cancel each other. For example, Cu has +3k and -1.6k for the volume and the temperature dependent terms, respectively, where k is Boltzmann's constant. This fact adds difficulty to experiments designed to obtain reasonable information on the change of the work function with changes in temperature. Considering that the electrical potential induced by the lattice vibration can be screened by electrons, a more reliable calculation was performed with the pseudopotential formalism in which the potential induced by lattice vibrations is smeared out [51].

I.C4. Direct and Indirect Transitions in Photoemission

Energy distribution curves (EDC) usually show various features which are ultimately related to the electronic band structure, and the features of the spectra show up in a way relating to the nature of optical transition. To distinguish between direct and indirect transitions from the features of spectra provides additional information for exploring the electronic band structures. The criteria are based on the variations of the energy distribution features with different exciting photons in the photoemission.

For a direct transition between discrete levels, the excited electrons originating in the bulk are excited to the empty states in the conduction band without phonon assistance. Therefore, the k vectors in the initial and final states have to be identical. Such a

constraint usually forces the summation of the initial state energy and the photon energy to be equal to the final state energy, and leads to two sorts of features in the experimental EDC: (1) the structure will appear and disappear abruptly at different photon energies, and (2) an increase of the photon energy by a certain amount, $\Delta\hbar\omega$, does not result in a peak-shifting to a higher energy by $\Delta\hbar\omega$. The former effect is because the transition probability varies with photon energy, such that the occurrence of any optical transition in photoemission is associated with a critical point in the final state, the critical point is more a saddle point rather than a maximum or minimum position in the density of states curve. latter is because various photon energies will emit electrons from their corresponding initial states in k-space. The energies of the initial states depend on the curvature of the valence band [53]. (Figure 1-7b)

For an indirect transition, the probability of an electron excited to the energy E from a lower energy $E-\hbar\omega$ by the photon energy $\hbar\omega$ is proportional to the product of the initial and the final density of states, and the energy distribution of photoemitted electrons D(E) is

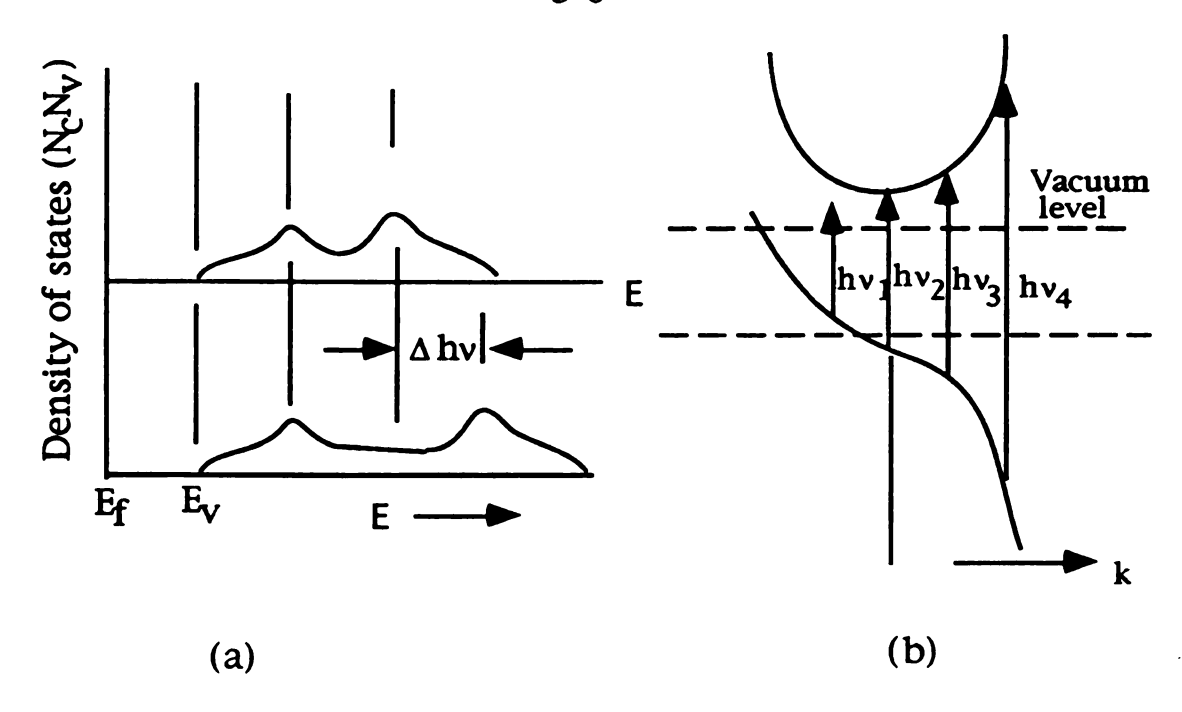
$$D(E) = CT(E)N_i(E - \hbar\omega)N_f(E)$$
 (1-7)

where N_i and N_f are the initial and final optical density of states, C is a constant, and T(E) is the escape function which is determined from the experimental data. Because the indirect photoemission is determined both by the empty high density of final states and by the high density of initial states, the emission peak in EDC either (1)

remains and is located at a constant energy in the distribution curve when the energy of photons is changed, and the energy of such a peak corresponds to the location of a maximum density of the final states, or (2) moves to a higher energy in an increment exactly equal to the amount of change of photon energy, corresponding to a peak in the density of filled valence band states [52]. (Figure 1-7a)

In the direct transition, if the wave functions of the initial state and the final state are well described by the Bloch wave function, and the excitation only involves a single electron, then the initial and final values of k must be the same. In contrast, for the indirect transition, the excitation does involve more than the single electron, for example electron-phonon scattering, the overall k may be still conserved (conservation of momentum) without the k values being the same in the initial and final states.

For solids with d-state electrons, such as transition metals, the bands are quite flat, and for such flat bands it sometimes is difficult to determine whether the transition is direct or indirect. The way to distinguish the transitions is to measure the temperature dependence and to compare the absolute quantum yield magnitude, because indirect transitions have obvious temperature dependence and lower quantum yield magnitudes [52].



Schematic representations of indirect and direct Figure 1-7. (a) A photoemission energy distribution for indirect transitions. transitions with constant matrix elements. The low energy peak is fixed in energy corresponding to a high density of states in the empty conduction band; the high energy peak that moves in energy by an amount exactly equal to the change in photon energy, $\Delta\hbar\omega = \hbar\omega' - \hbar\omega$, corresponds to a peak in the density of filled valence band states. (b) The direct transition processes. Because of the energy variations in the initial states, the important features in EDC move to higher energies at a somewhat slower rate than the increase in photon energy.

Another criterion was proposed by Spicer [43], that a nondirect transition can take place in the excitation process in the three-step model. The nondirect transition has a peak with the characteristics of an indirect transition, and the peak moves to higher energy by an amount that is exactly equal to the increment of the photon energy, except that it is temperature independent. The suggestion was based on the experimental results from the semiconductors Cs₃Bi and Cs₃Sb,

and the metals Cu and Ag [53][54]. He interpreted the effects as due to a weak overlap of valence state wave functions on adjacent lattice sites, and *energy* conservation instead of momentum conservation becomes the selection rule for the optical transition.

However, the interpretations are not without controversy. The transitions in the energy distribution curves for Cu and Ag were interpreted as nondirect processes by Spicer; whereas the results obtained by Smith [55] indicate direct transitions. Both model calculations of the energy distribution of the joint density of states and experimental spectra of the energy distribution curves were used to prove that the transition processes are direct. Other measurements of Cu and Ag with higher photon energy, 10 - 27 eV, also indicated that the transitions are direct rather than nondirect processes [56]. The discrepancies are due to the fact that the three-step model is too simple to interpret all the photoemission phenomena [57].

CHAPTER II

THE PHOTOEMISSION APPARATUS AND PHOTOEMISSION STUDIES

IIA. Introduction

Alkalides and electrides are very sensitive to air, moisture and temperature. Except for a few compounds, most alkalides are usually highly unstable and will decompose at temperatures higher than -20 °C, even under inert atmosphere or vacuum conditions; the electrides are even more unstable and the decomposition temperature is lower, with decompositions setting in when the temperature is higher than -40 °C [8.58].

For these materials, the experimental conditions have to be restrictive. Many measurements of bulk properties can be performed if the samples are transferred in a glove bag that is filled with nitrogen gas or in a dry box; however, an even more restrictive condition is required for the surface measurements, since the materials are so reactive that their surfaces are easily decomposed, or can become contaminated, especially at low temperatures. Based on the above considerations, the present photoemission apparatus was built to circumvent these difficulties. The design permits the sample to be loaded under a high vacuum environment at low temperatures to minimize decomposition.

Two photoemission apparatuses had been built in the past, but both systems were not without problems in vacuum and sample loading. The first one was made entirely from Pyrex, except for the

metal electrodes. The vessel was pumped by a small ion pump, and the vacuum was maintained at only 10-4 torr [18]. The second photoemission apparatus was constructed of stainless steel; however, most of the O-rings used at the joints were Viton instead of copper Such sealing introduced the possibility of leakage caused either by the shrinkage of the gaskets at low temperatures or by the deterioration of the gaskets by organic solvents such as methylamine. Although the system was pumped by a turbomolecular pump, the vacuum could reach only 10-5 torr [59]. In both previous systems the loading of samples had to be performed in a glove bag, so that we could not rule out the possibility of a trace amount of moisture being condensed on the surface of sample. As mentioned earlier, the surface quality is so important for photoemission studies that we decided to design a new system to decrease the chance of the sample coming in contact with air or moisture.

Thermionic emissions from the alkalides and electrides had been observed in the previous system [72]. However, the phenomena did not show up in this new system. We infer that the thermionic emissions might be from the surface reactions or the surface contamination due to the lower vacuum of 10^{-5} torr, which is compared to this new system with vacuum of 10^{-8} torr.

Alkalides and electrides have very unusual properties due to the presence of weakly bound ns² electrons in anions and as trapped electrons in electrides. The apparent band gaps of most alkalides are low (0.8 -1.5 eV), which probably results from defect electrons whose energy states lie in the gap. All the alkalides, except

Na+C222·Na-, are therefore considered to be electron-doped extrinsic semiconductors [13], and electrides are insulators, semiconductors or near-metals. The photoemission method is a useful way to characterize the energy states of trapped electrons and the valence bands of these compounds.

Photoelectron emission spectroscopy (PEE) provides direct information in exploring the electronic states of materials, especially solid materials. In our system, the light source spans the region from the ultraviolet to the near infrared. Ultraviolet incident radiation probes the electron distribution of valence electrons to provide direct information about the amount of energy required for the transition of electrons from the valence band to the vacuum. Visible and infrared radiation provide information about excitation of the trapped electrons.

The emitted electrons originate from depths a few hundred Angstroms below the surface, and electron emission involves both volume and surface processes [44], so that surface cleanliness is very critical in PEE for a solid sample. The most common methods of obtaining a fresh surface are by cleavage of a crystal [73], by ion sputtering [60], or by continuous evaporation of a metal to form a fresh film [61] in an ultra-high vacuum environment. Unfortunately, none of these methods can be applied to the alkalides and electrides due to the high instability and reactivity of these compounds. Therefore, our procedure has to be more complicated than the usual methods, in that we have to load and dissolve the sample, alkalides or electrides, in a solvent and then remove the solvent under high

vacuum and at a low temperature, so that a fresh film can be obtained.

There have been a number of apparatuses built for photoemission measurements with the possibility of study under UHV conditions and at low temperatures [62,63], but none of these provide for loading samples which are air and temperature sensitive. The apparatus which we built has the advantage of loading the sample while cold with minimum contact with gases, which gives the best possible way to guarantee the quality of the samples.

IIB. Description of the System

II.B1. General Aspects of Design

The photoelectron emission apparatus shown in Fig. 2-1 has four main components. (1) The vacuum system is composed mainly of the loading chamber, the film-preparation chamber, and the main chamber where photoelectron emission is measured; (2) The pumping system which consists of two roughing pumps for prepumping of the sample loading chamber and for pumping the transition feedthroughs, an 8 inch cryogenic pump (Leybold-Heraeus) which is isolated from the film preparation chamber by a high-vacuum valve for efficient condensing of solvent gas from the sample film, and a turbomolecular pump (Varian 3000) backed by a high capacity roughing pump (Varian SD-300) to pump out the main chamber, creating the high vacuum (better than 10^{-8} torr); (3) The feedthroughs, which provide the necessary electrical and optical access, and cooling, sample transportation and temperature control;

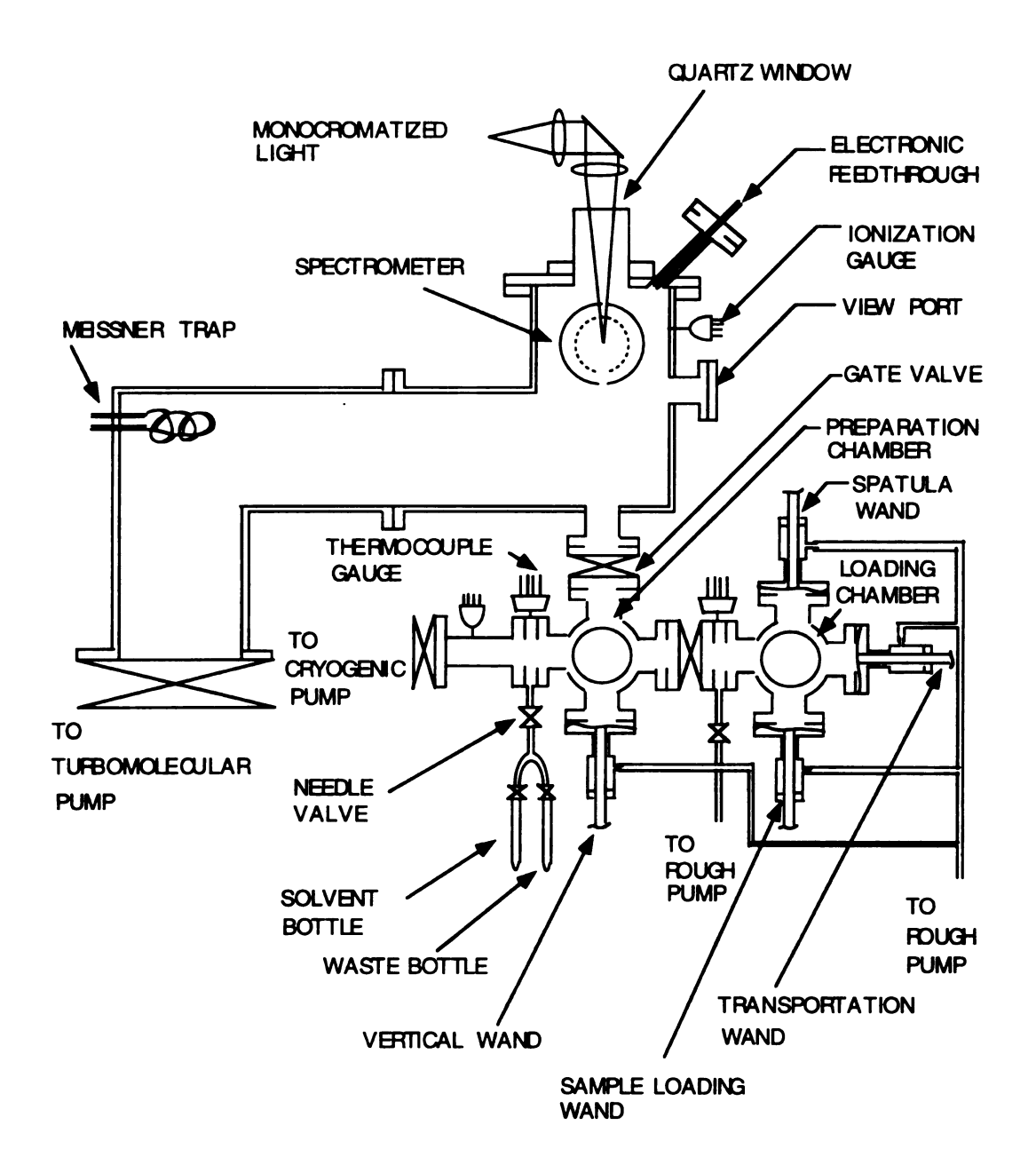


Figure 2-1. Schematic view of the photoemission apparatus

(4) The data collection system, which uses an IBM XT microcomputer for the collection of data, and an IEEE 488 interface board (from Metrabite) to talk and listen to a Keithley 617 electrometer. The computer also communicates with a home-built interface via a RS-232 serial port to control the scanning speed of the monochromator and to read data from the controller. The block diagram of the system is given in Fig. 2-2.

II.B2. The Vacuum System

The vacuum system is composed of a loading chamber, prechamber and main chamber. The materials, including the gate valves, are stainless steel (MDC Manufacturing Co.); the joint materials are copper gaskets, with the exception of the loading chamber where Viton gaskets are used. There are two reasons for the use of Viton instead of copper gaskets: one is that the vacuum of 10-5 torr will be good enough for sample loading, and the other is for easy, fast cleaning and operation.

Before operating the system, the main chamber and preparation chamber are pumped down to 10^{-8} and 10^{-6} torr respectively, while the gate valve between these two chambers is closed to assure ultra high vacuum in the main chamber. However, the gate must be opened momentarily to transport the sample from the preparation chamber into the main chamber. There is a 3/8" orifice in the gate when it is open. The effect of the orifice has been evaluated, and its throughput is only 1×10^{-6} Watt (equal to the conductance of 1×10^{-8} L s⁻¹ at atmosphere) if the vacuums in the preparation chamber and the main chamber are 10^{-6} and 10^{-9} torr,

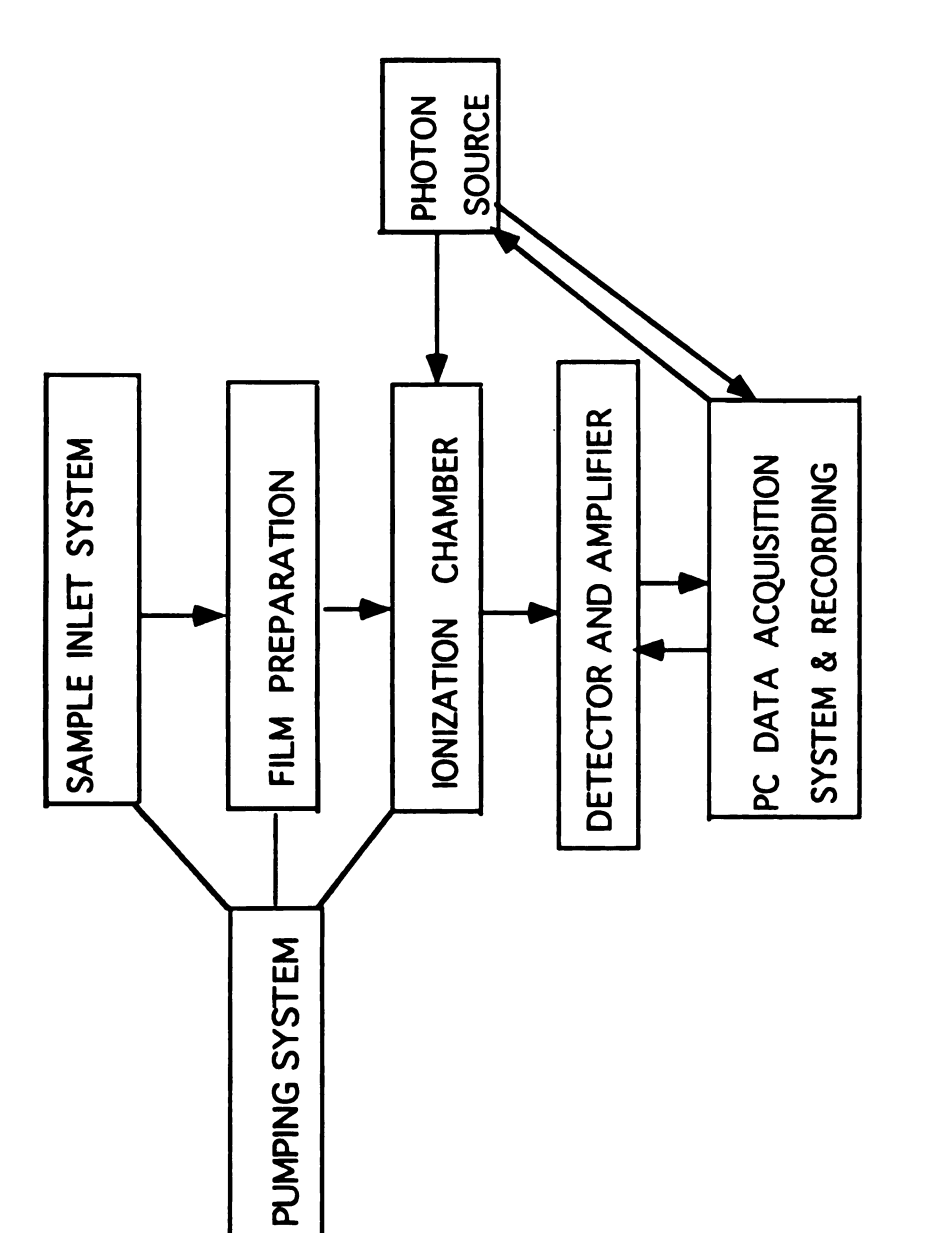


Figure 2-2. Block diagram of the photoemission spectrometer.

respectively. Thus, opening the gate valve causes little deterioration of the vacuum in the main chamber.

II.B3. Temperature Control

Temperature control is essential in the experiment. The vertical wand, for holding the sample during measurement, provided for temperature control, with the structure shown in Figure 2-3. There are two inner tubes in the wand, one inside the other, which have two functions: one is for directing the flow of nitrogen gas, and the other is to work as a heater to warm the nitrogen gas. The high resistance of stainless steel tubing allows generation of heat by passing current through it. House nitrogen, with a pressure of 20 psi, is circulated through a liquid nitrogen bath and then used to cool down the sample holder. The temperature of the sample holder, which can go down to -130 °C, is monitored and controlled by an Omega temperature controller (model No. CN2001T-AT). A Variac and a converter are added in the circuit between the heater and the temperature controller for more accurate and efficient controlling. For example, for a 20 degree change from -80 to -60 °C, the temperature was stabilized in 10 minutes to within ±2 °C (see Fig. 2-4). However, it takes longer to decrease the temperature further; a 30 degree change from -60 to -90 °C required 20 minutes to The flow rates of nitrogen are controlled by two flow meters (manufactured by Cole Parmer Co.) with calibrated scales from zero to 23 and zero to 11 liters per minute, respectively. larger flow meter regulates nitrogen flowing through the temperature controllable vertical wand, and the other flow meter

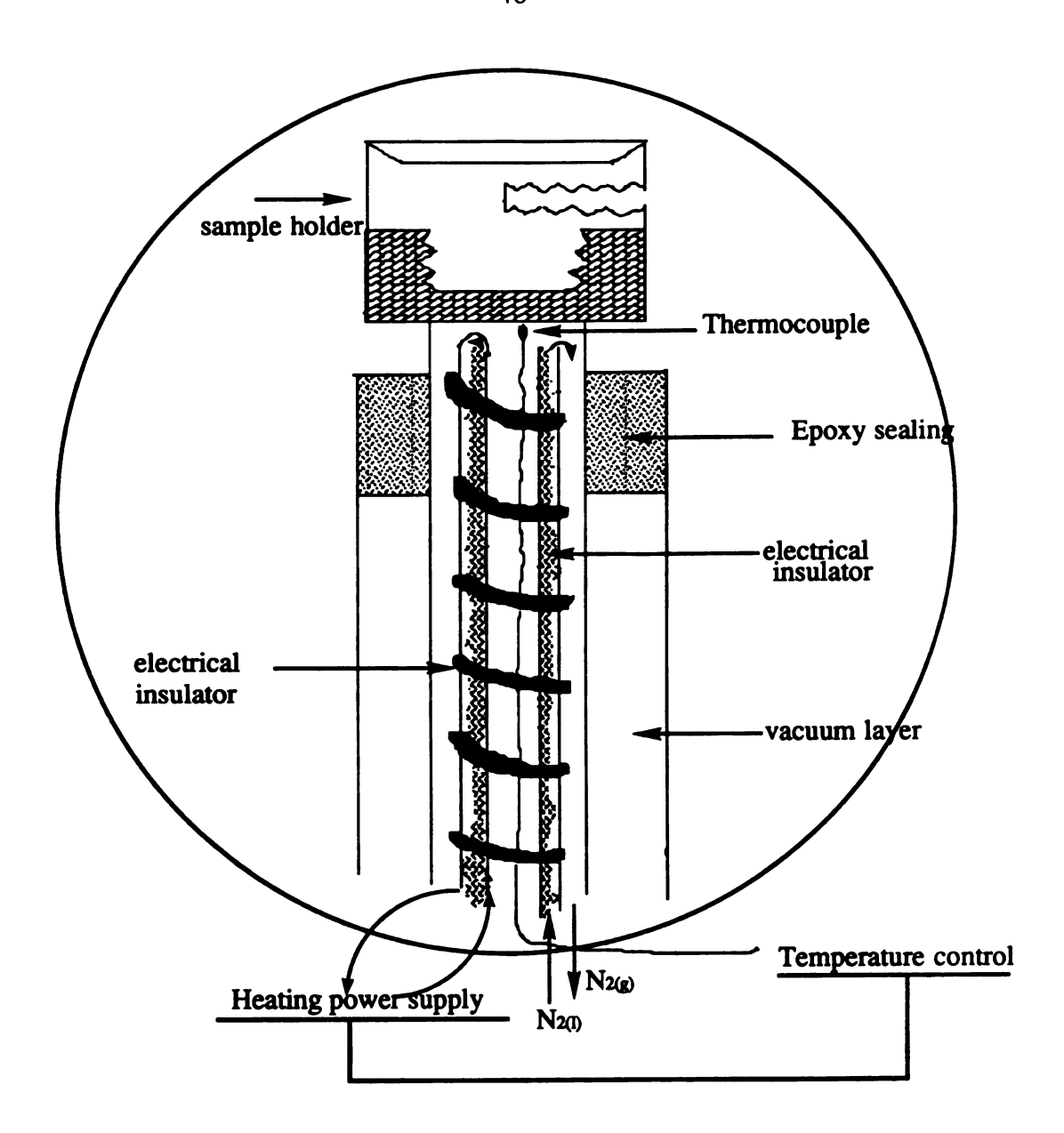


Figure 2-3. The structure of the vertical wand. The temperature is monitored by a thermocouple and stabilized by a temperature controller which produces an output current to heat up the inner stainless steel tubing if the temperature is lower than the pre-set value.

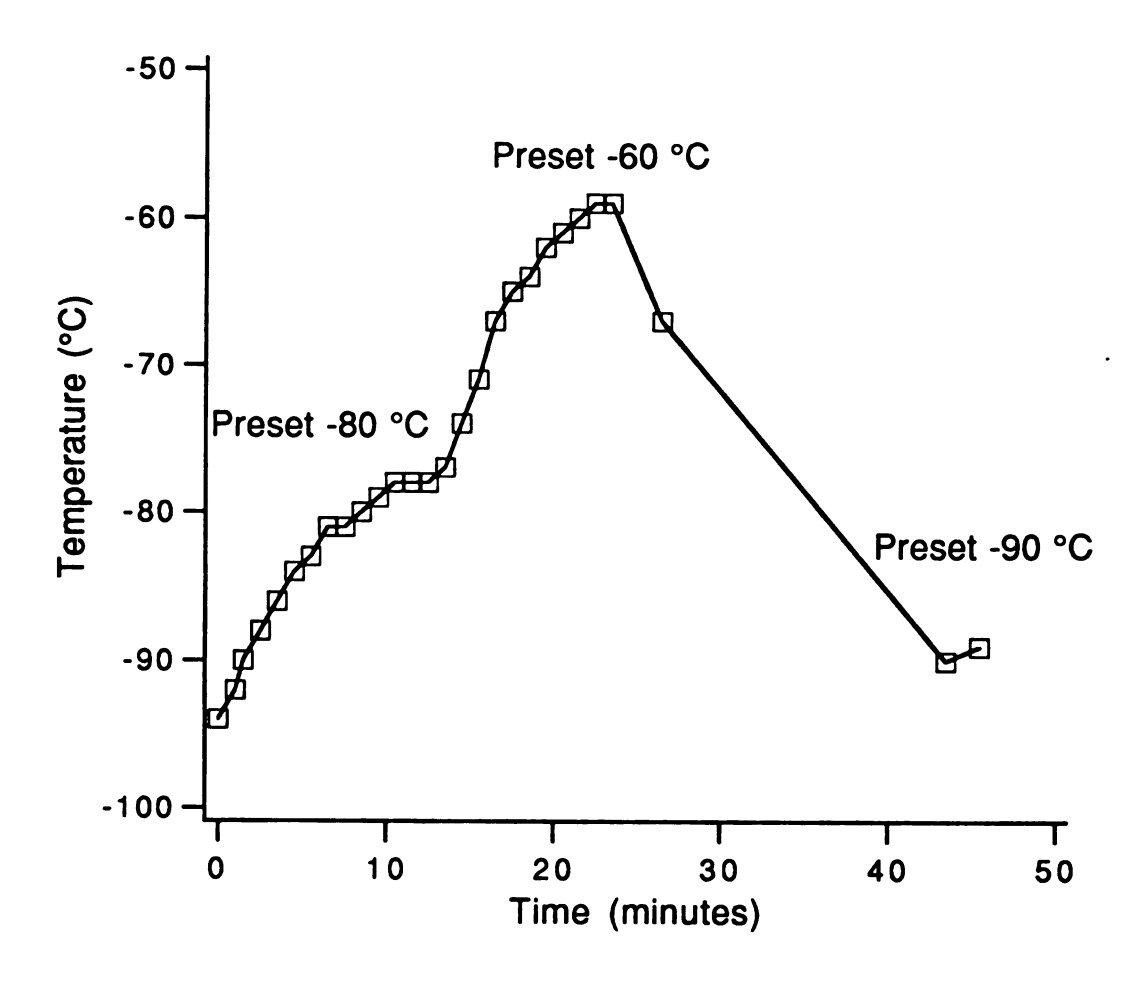


Figure 2-4. The stabilizing rate and precision of temperature control of the sample holder.

adjusts the nitrogen flow through the sample-holding and the transportation wands.

II.B4. Electronic Systems

The electronics circuit of the spectrometer is shown in Figure The sample holder is the cathode, and the electron collector works as the anode. For quantum yield measurements, the grid was connected to a real ground potential to prevent charge capacitance inside the spectrometer, since larger capacitance will increase the In order to eliminate the noise generated from response time. magnetic and electric field interferences, the preamplifier (109) amplification) was placed inside the vacuum system. necessary, the amplification factor can be switched to $9x10^7$. The output voltage is measured by a Keithley 617 electrometer. space charge buildup on the surface of the sample film, a bias voltage (supplied by the same electrometer) was imposed between the cathode and the anode to extract the emitted electrons. extraction voltage was 40 V, which corresponds to an electric field of ≈ 8 V/cm. The response time of the system is ≈ 40 ms. determined from the fast exponential decay of the "shot-signal" recorded by an oscilloscope (Tektronix 7313), when an alkali metal film was illuminated by a laser pulse.

II.B5. Data Acquisition Methods

An IBM XT computer with an IEEE-488 interface board, a Keithley electrometer and a home-built interface are used for data acquisition. The computer controls the output of the bias voltage and

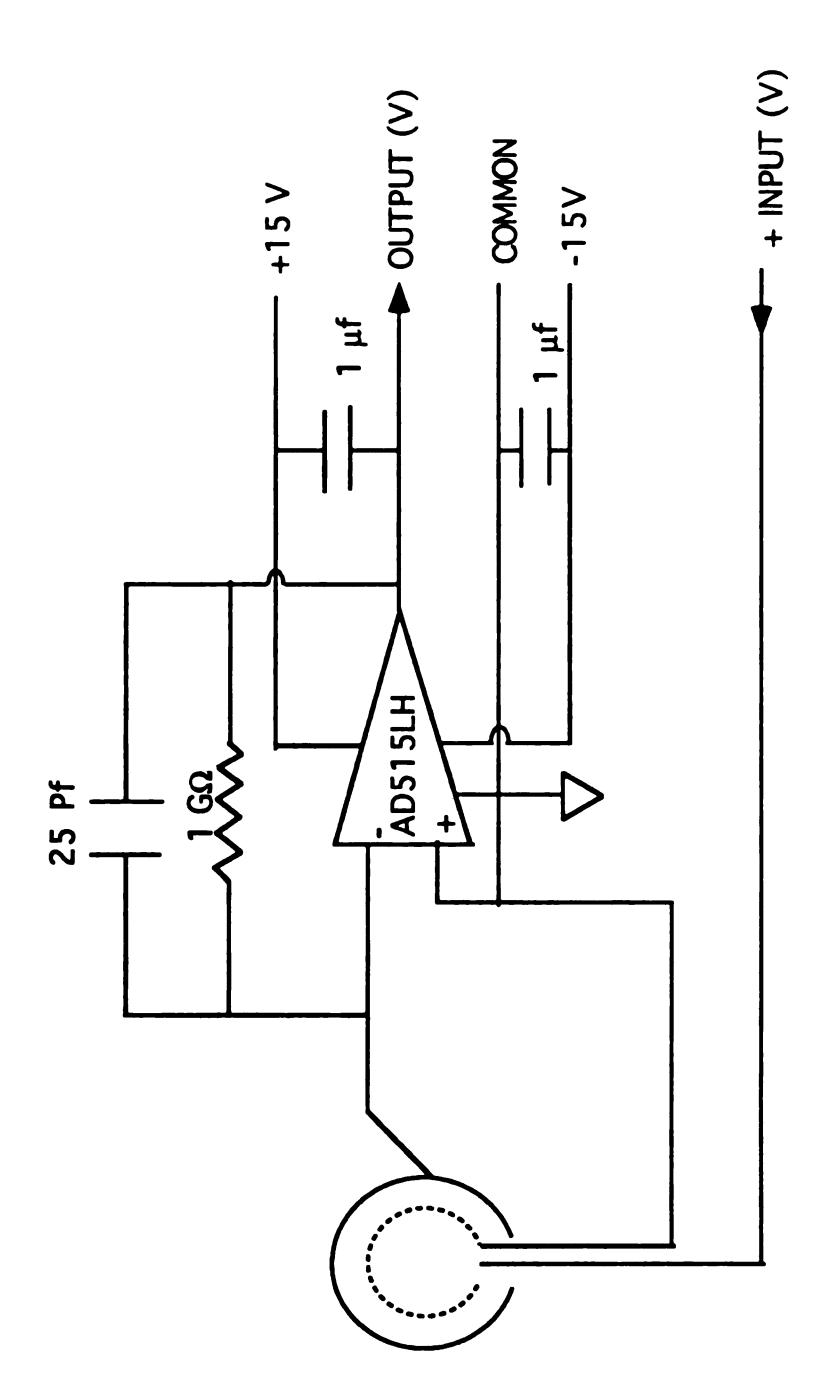


Figure 2-5. The circuit of spectrometer including the preamplifier is inside the vacuum chamber.

reads the input signal of the electrometer; in addition, it also controls the scanning speeds of the monochromator and records the corresponding wavelengths through the home-built interface.

The Keithley 617 Programmable Electrometer can be used as a sensitive voltmeter, ammeter and ohmmeter. When measuring, it can also act as a voltage source which ranges from -102 V to +102 V in 50 mV increments.

The programs were written in Microsoft GW-Basic language. The IEEE-488 interface board has some software located in ROM for controllers. In programming, we need only call in the software as subroutines. The home-built interface for the monochromator stepper motor is commanded by specific ASCII codes (see Table 2-1) that direct the logic executions. The UART unit (Universal Asynchronous Receiver-Transmitter) in the interface is designed to operate with a microprocessor, and to incorporate auxiliary logic. When the interface is energized, the registers in the UART are loaded automatically to set up for communication: 8 bit word, 9600 baud, no parity bit, one stop bit. When the set-up is ready, the interface will send a "2" (00000010) to the computer to signify that it is ready to receive commands from the computer. Data sent to the interface should have the interface codes listed in Table 2-1. First, set the Grating, then sequentially the Step Rate, and Start and Stop digital numbers. When a READ command is sent, the interface will send the digit requested and immediately go back into the receive mode to accept the next command. Such flip-back-and-forth operation proceeds until the logic matches the Stop command. The program must be written according these formats. to

Table 2-1. ASCII codes for the monochromator-computer interface.

Decimal	Hex	Comr	nand	Descri	pti	on					
0	0	Set the direction to REVERSE									
1	1	Set the direction to FORWARD									
2	2	START in the REVERSE direction									
3	3	START in the FORWARD direction									
4	4	STOP	with	directi	on	set	to	REVE	RSE		
5	5	STOP	with	directi	on	set	to	FORW	ARD		
16	10	set th	e GRA	TING	to	1 a	and	STEP	RATE	to	100
17	1 1	**	••	**	••	2	••	**	"	**	100
18	12	**	"	**	**	1	"	11	**	"	50
19	13	**	••	**	**	2	••	**	**	**	50
20	14	**	••	**	"	1	"	**	***	**	20
2 1	15	••	••	••	**	2	"	**	**	**	20
22	16	"	••	"	**	1	**	**	11	**	10
23	17	"	ti .	••	••	2	"	"	"	**	10
24	18	**	**	**	**	1	••	"	**	**	5
25	19	**	••	"	••	2	"	"	"	"	5
32+DIGIT	2 x	enter START DIGIT 0, x=DIGIT:0,1,2,3,4,5,6,7,8,9									
48+"	3 x	"	**	**		1,		"			
64+"	4 x	••	**	"		2,		"			
80+"	5 x	**	••	"		0,		**			
96+ "	6 x	**	**	"		1,		**			
112+"	7 x	••	**	"		2,		**			
128+"	8 x	read COUNTER DIGIT 0, x=DIGIT read:1,2,3									
144+"	9 x	**	**		"	1	,		•	•	
160+"	Ax	"	**		"	2	·,		•	•	

The photoemission data as a function of wavelength were collected by using the Basic program MONOVOLT.bas which is listed in the Appendix. This program controls the Keithley 617 electrometer and the monochromator. The program can take measurements at different bias voltages up to -102 V. Typically, -40 V bias gives the saturation emitting current, which is determined by using the program VOLTSCAN.bas. The monochromator has 5 speed rates and can scan forward or backward. The parameters for these functions can be set in the program. As for the other data acquisition programs used in these experiments, the data collected by MONOVOLT.bas were stored in ASCII format, which can be used directly for quantum yield calculations and plotting purposes.

The program VOLTSCAN.bas applies the scanning bias voltage to the spectrometer when the light source is at a specific wavelength. The program only needs to communicate with the Keithley 617 electrometer, while the monochromator is preset at a specific wavelength. This allows us to determine the saturation current from the emitting intensity as a function of voltage. If a positive bias were scanned (but not feasible with our sample) the spectrum obtained could be differentiated with respect to the applied voltage to obtain the energy distribution curve.

The program PHOLASER.bas was written for measurements made during photobleaching experiments. This program was derived from the program VOLTSCAN.bas, and allows one to measure the photoemission current as a function of time at a specific wavelength and bias voltage. The time interval between data points can be preset. This allows the study of photobleaching effects in

photoemission caused by laser pulses. Detailed descriptions of the bleaching phenomena are given in Chapter 3.

II.B6. Optical System

The light from a 1000-W xenon lamp is focused onto the entrance slit of the scanning monochromator (Oriel model No. 77250). Two diffraction gratings are used, and they range from 200-700 and from 300 - 1000 nm, with a resolution of ~13 nm. The monochromatized light is collimated and directed through a right-angle mirror, then focused vertically through a quartz window onto the sample. The output signal is pre-amplified before leaving the vacuum system, and the dark current is about 2 picoamperes.

II.C. Experimental

II.C1. Sample Preparation

The electrides and alkalides were synthesized under vacuum (≈10-5 torr) in a low temperature environment [7,8]. When the synthesis had been completed, the crystalline samples were sealed in Pyrex ampoules which were sealed to the synthesis cell. The samples were stored in a liquid nitrogen dewar prior to the measurements.

The sealed sample was loaded into the tip of the loading wand, where it was kept cold by blowing cold nitrogen gas through the inner tubes of the vacuum insulated wand. The loading chamber was first pumped by a roughing pump until the pressure reached less than 100 mtorr, then the gate valve between the loading chamber

and the preparation chamber was opened to let the cryopump evacuate both chambers. The sample was then loaded in a vacuum of $\approx 10^{-5}$ torr. The procedures are as follows: (1) first, the transportation wand is moved forward to break the sample ampoule; (2) then another wand directly opposite from the loading wand, with a spatula on the tip, removes the sample and loads it into the sample cup; (3) finally, the sample is transported to the vertical wand which had been pre-cooled to a temperature of -60 °C by blowing cold nitrogen through it. (Fig. 2-6)

The vertical wand is used for film preparation and spectral measurements. We prepared a fresh surface film by the "dissolve-and-dry" procedure. First the solvent, methylamine or dimethylether, was condensed onto the crystalline sample by cold-condensation at -60 °C in the vacuum of the preparation chamber. When the crystal had been completely dissolved, the solvent was removed first by condensation into a liquid nitrogen trap, then pumped by the cryogenic pump immediately for 3 minutes. After the solvent had been removed, the characteristic color of the sample reappeared on the film. Thereafter, the vertical wand was pushed upward slowly, through the opening in the gate valve, into the center of the spherical spectrometer for the measurements.

II.C2. Measurements

The computer controlled the output bias voltage and the scanning speed of the monochromator, and simultaneously recorded the intensity of photoemission (as a voltage) and the corresponding wavelengths of the exciting photons (in nanometers). The

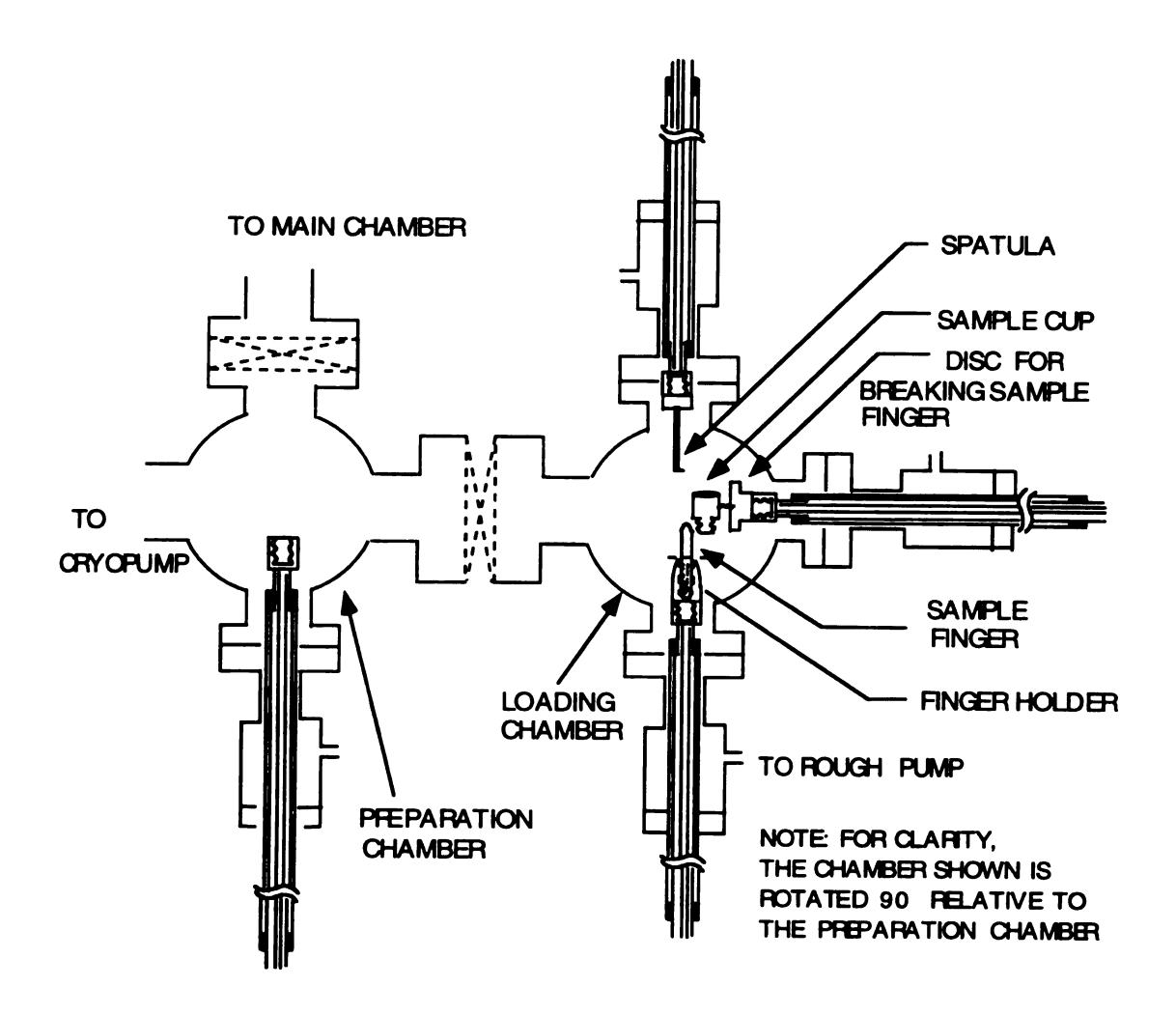


Figure 2-6. Schematic view of sample loading and transportation. The transportation wand has a level 0.8 cm lower than the loading and spatula wands.

monochromatized light focused on the sample had a trapezoidal shape and was about 2x3 mm² in size. The light intensity was on the order of 10¹⁵ photons per second, which generally emitted electrons to yield photocurrents in the nanoampere range. After 10⁹ amplification, the output was the order of volts. The quantum yield was calculated by reference to a standard light intensity measured by a silicon diode detector (EG&G model No. UV44430). The yield is calculated as follows:

$$Y_s = (I_s/I_p)Y_p (2-1)$$

where Is and Ip are the photocurrent measured from sample and the calibrated standard photocell, and Yp is the quantum efficiency of the photocell.

II.D. Results and Discussion

Because the sample could be loaded in a vacuum environment and kept cold during film preparation, we were able to measure photoemission from alkalides. The alkalides, K+(15C5)₂·K⁻, Rb+(15C5)₂·Rb⁻, Na+C222·Na⁻, K+C222·K⁻, Cs+C222·Cs⁻ and K+C222·Na⁻, were measured (Fig. 2-7 - 2-12). The spectra show the common characteristics that there is a main peak at greater than 4 eV and a low energy tail, and sometimes the high energy peak has a shoulder on the low energy side. The low energy tail may contain another broad peak whose position varies with respect to the nature of sample. For example, K+C222·Na⁻, Rb+(15C5)₂·Rb⁻ and

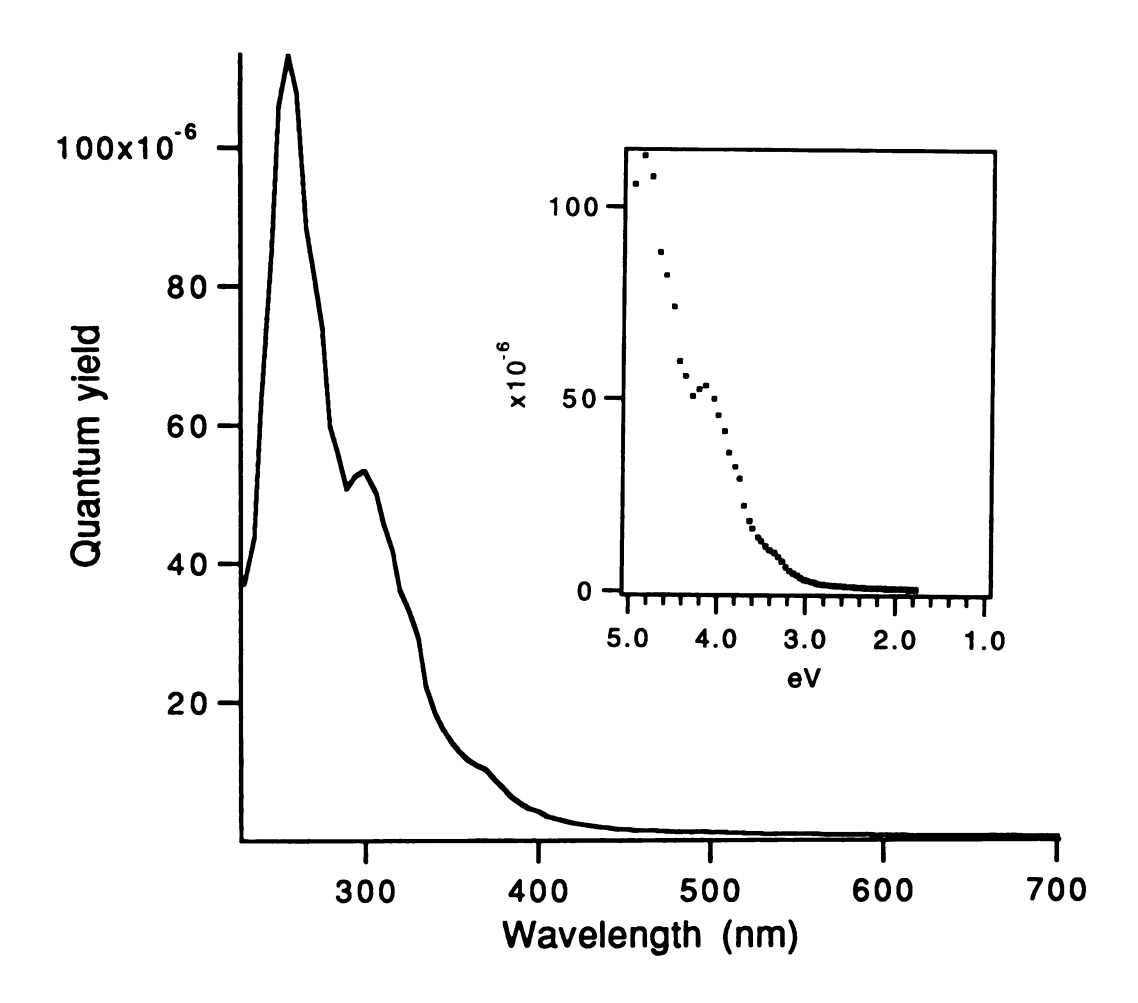


Figure 2-7. Quantum yield spectrum of $K^+(15C5)_2 \cdot K^-$ at -60 °C. The photoemission threshold energy for the valence band is $\approx 3.4 \pm 0.1$ eV, which is determined by extrapolating the low energy side of the main emission peak to intercept the X-axis.

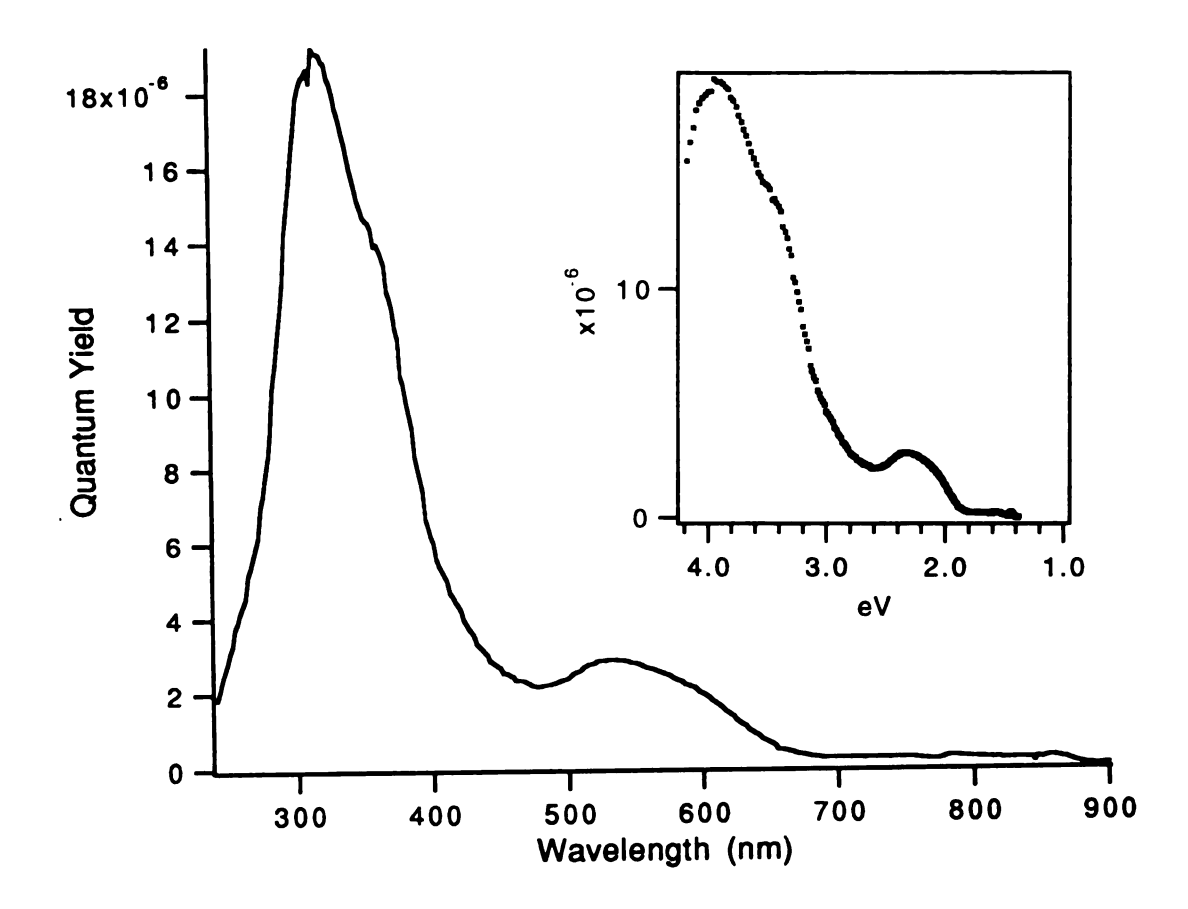


Figure 2-8. Quantum yield spectrum of $Rb^+(15C5)_2 \cdot Rb^-$ at -60 °C. The photoemission threshold energy for the valence band is $\approx 2.9 \pm 0.1$ eV, which is determined by extrapolating the low energy side of the high energy peak to intercept the X-axis. The low energy peak, 500 - 650 nm, is from trapped electrons.

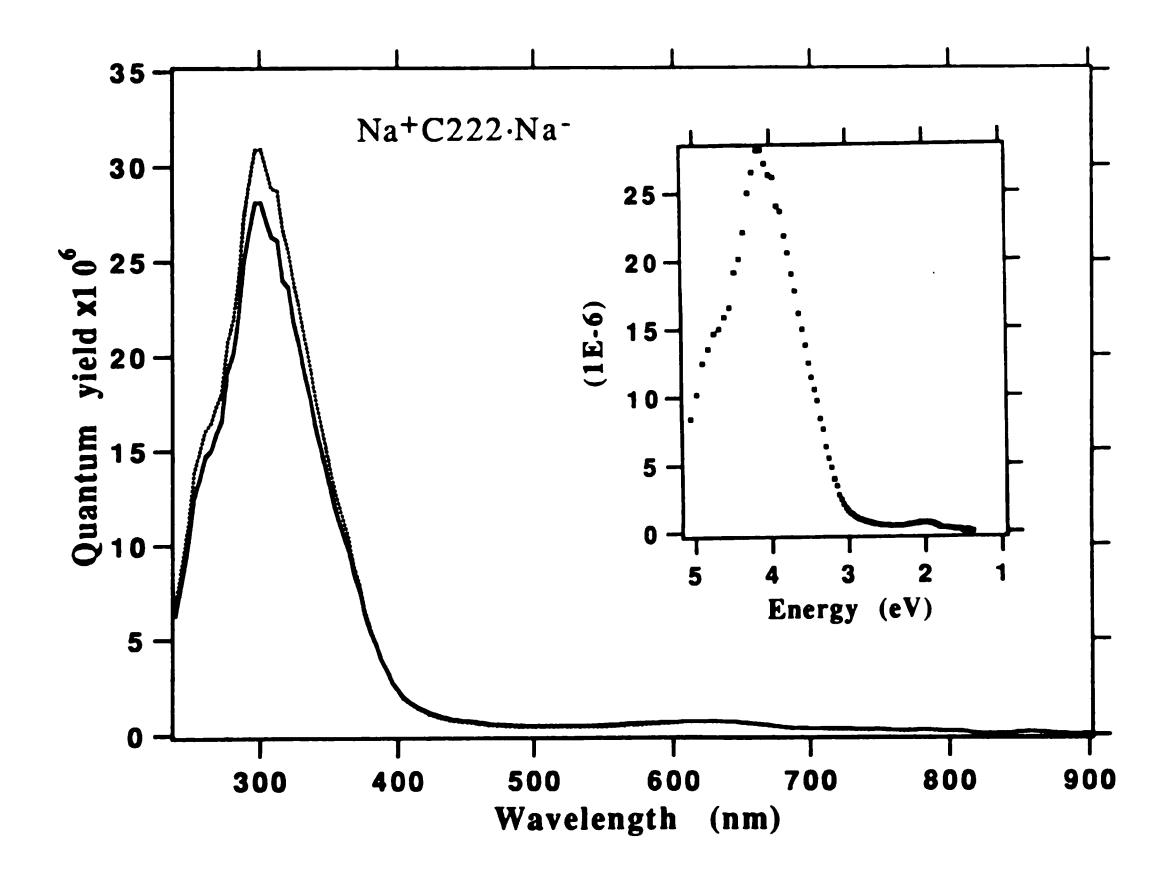


Figure 2-9. The threshold energy for the emission from the valence band edge to the vacuum level is 3.1 ± 0.05 eV, obtained by the extrapolation of the low energy straight line behavior versus energy shown in the inset. The slightly increased spectrum shows the slight effect of three 532 nm laser pulses.

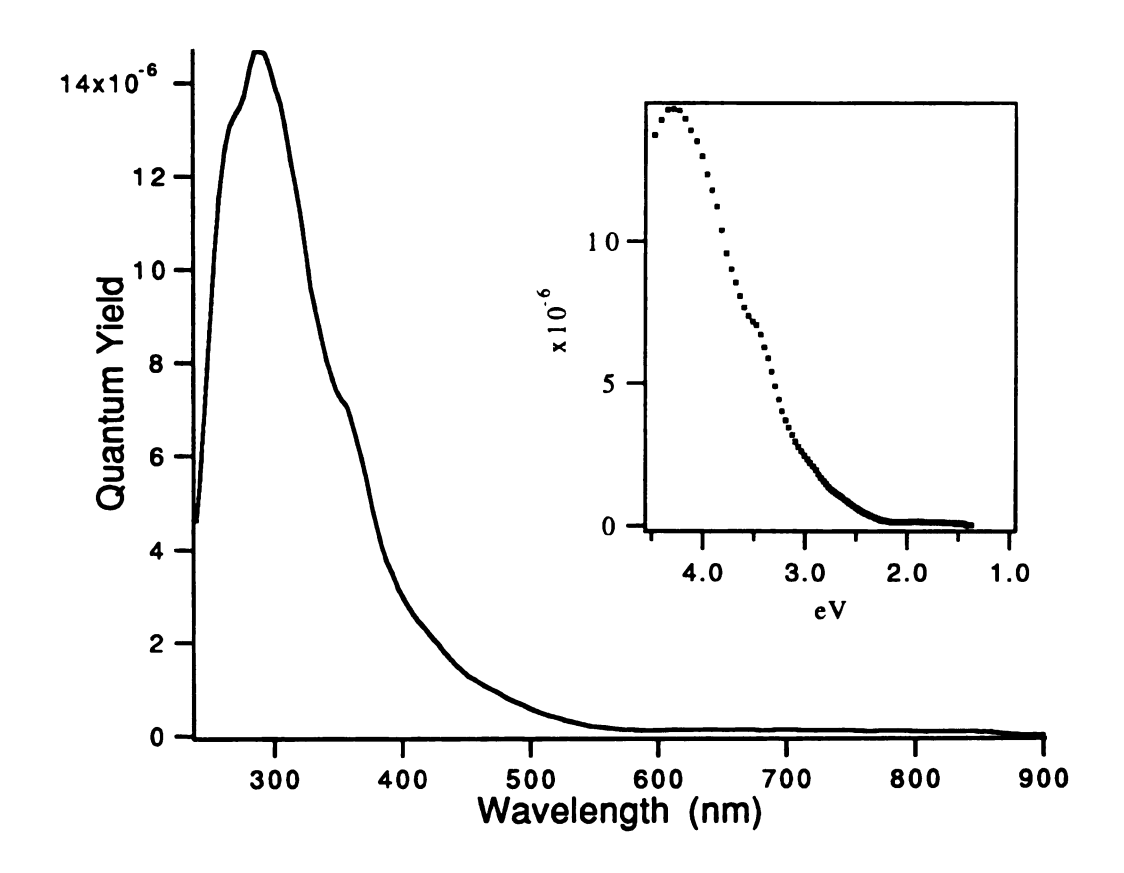


Figure 2-10. Quantum yield spectrum of $K^+C222 \cdot K^-$ at -60 °C. The photoemission threshold energy for the valence band is $\approx 3.1 \pm 0.1$ eV, which is determined by extrapolating the low energy side of the main emission peak to intercept the X-axis.

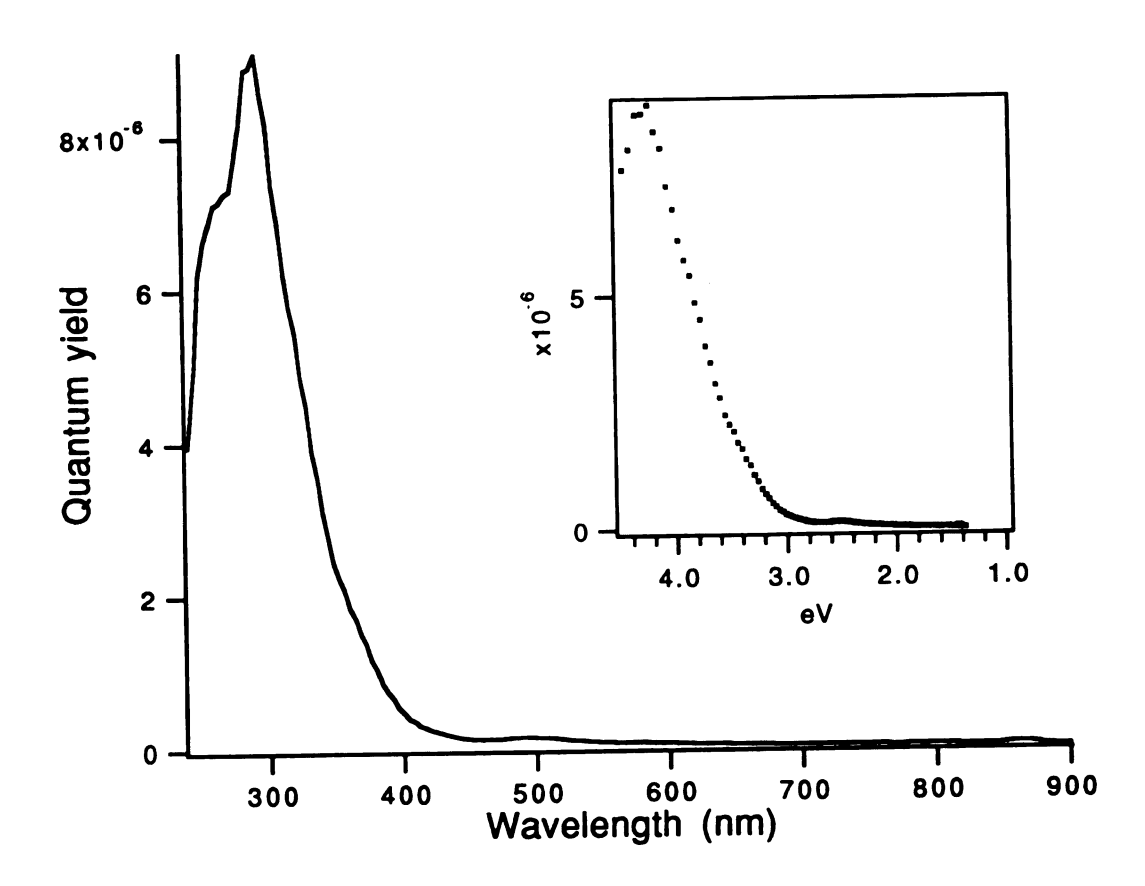


Figure 2-11. Quantum yield spectrum of Cs⁺C222·Cs⁻ at -60 °C. The photoemission threshold energy for the valence band is $\approx 3.4 \pm 0.05$ eV, which is determined by extrapolating the low energy side of the main emission peak to intercept the X-axis.

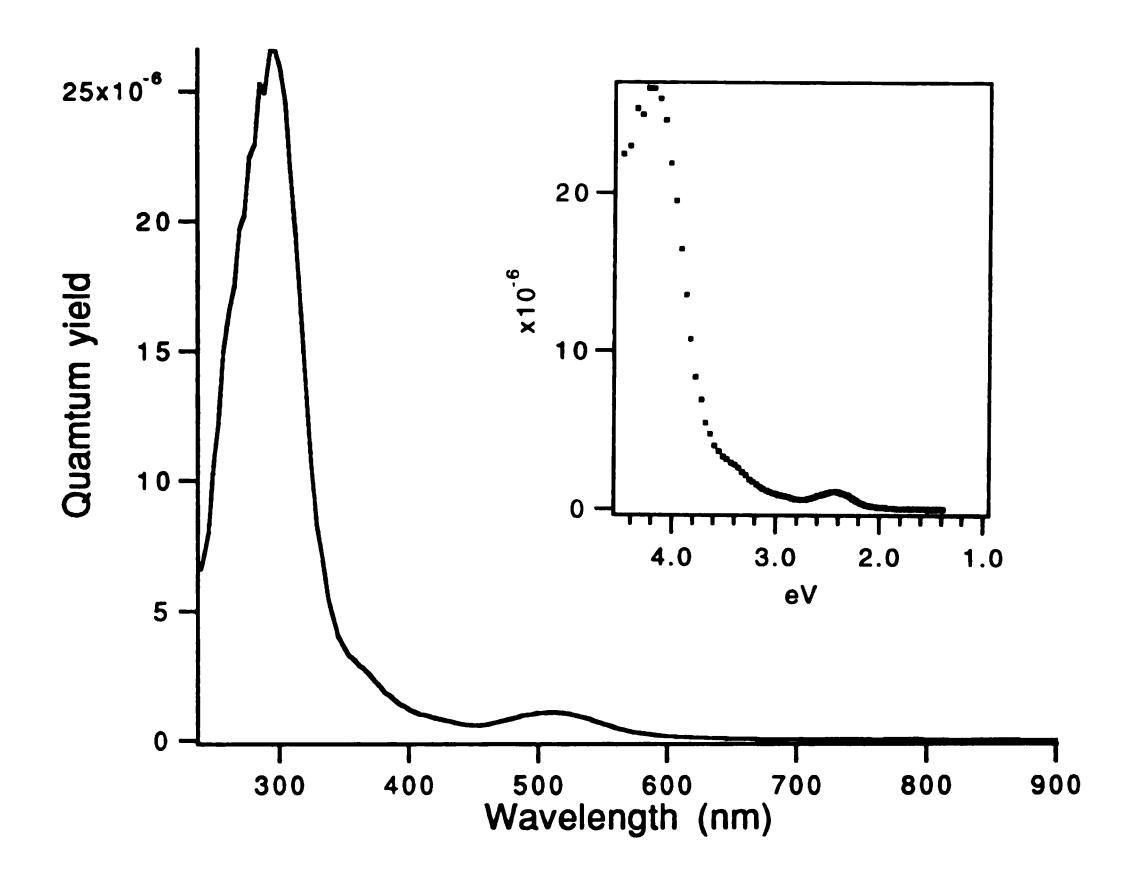


Figure 2-12. Quantum yield spectrum of $K^+C222 \cdot Na^-$ at -60 °C. The photoemission threshold energy for the valence band is $\approx 3.6 \pm 0.05$ eV, which is determined by extrapolating the low energy side of the high energy peak to intercept the X-axis. The low energy peak, 460 - 570 nm, is from the trapped electrons.

Na⁺C222·Na⁻ (see Figure 2-17) have peaks in the range of 460 - 570, 500 - 650 and 430 - 700 nm, respectively. The low energy peak doesn't always appear for a sample in different experimental runs, and its intensity depends on the experimental conditions which include the method of sample loading, film preparation and the temperature. The photoemission quantum yields for these alkalides vary from ≈10⁻⁴ to ≈10⁻⁵. The emission intensity is relevant to the inherent properties of the compound as well as the experimental parameters such as thickness of sample film, surface conditions and temperature. In general, thicker films have lower emission intensities, which may be due to the higher resistance leading to a slow charge neutralization. The surface charge indeed reduced the emission intensity.

Figure 2-13 shows the decrease in the photoemission intensity of K⁺(15C5)₂·K⁻ with a decrease in temperature. The measurements were made at -30, -60 and -90 °C in order, and the time intervals between the measurements were about 30 minutes. The emissions on the high energy side apparently show less temperature dependence than those on the low energy side. Although we also have to consider the decay of intensity with time, the time effect is small in this short period compared with the temperature effect.

The same anion in different complexant systems is expected to have different photoemission threshold energies because the highest energy bands are formed from contributions of the alkali metal anion outer-shell electrons whose energies relative to the vacuum level will be sensitive to the environment. Indeed, the onsets of photoemission of the high energy peaks from $K^+(15C5)_2 \cdot K^-$ and

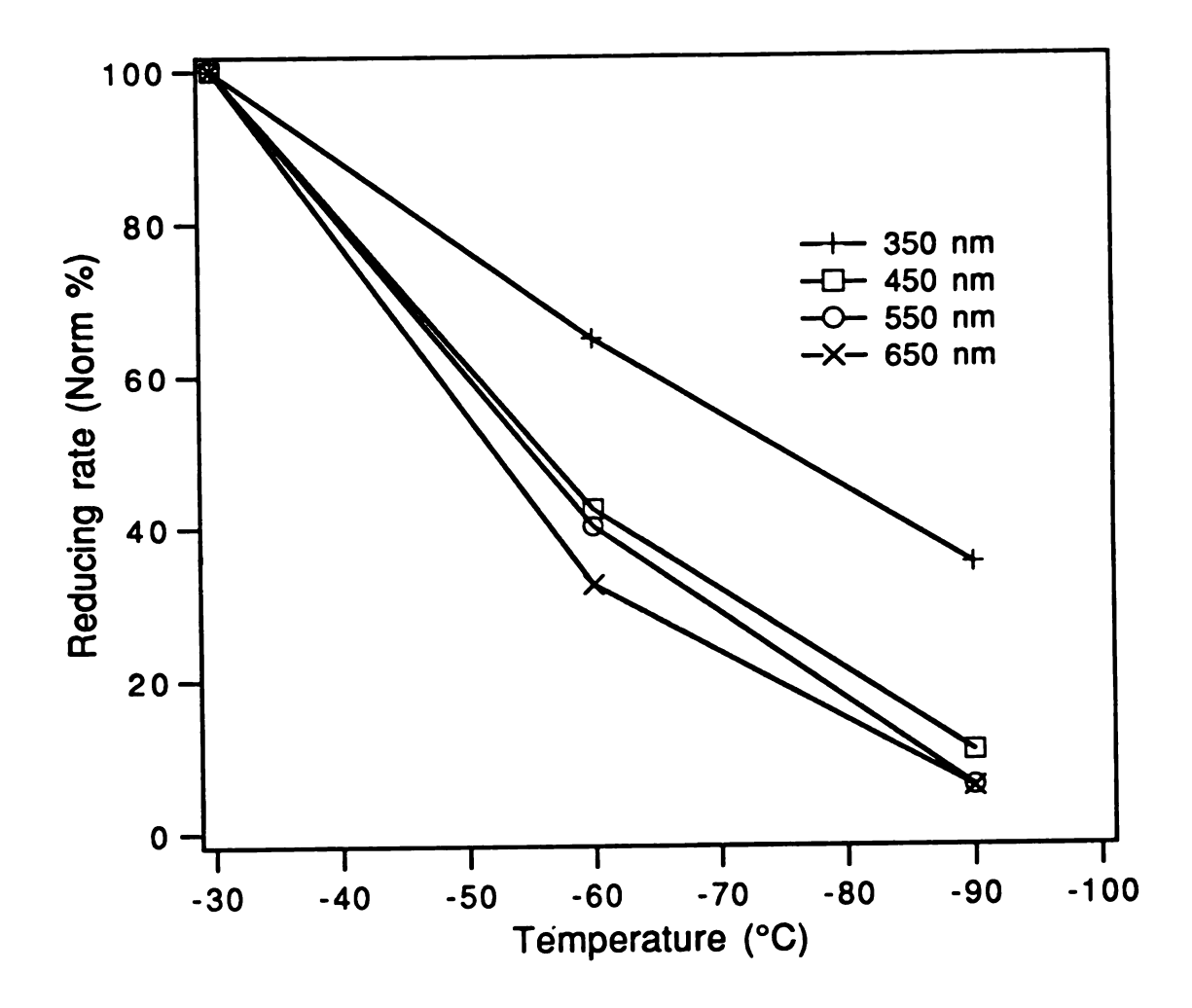


Figure 2-13. Normalized decrease in the photoemission intensity at various wavelengths with changes in temperature for $K^+(15C5)_2 \cdot K^-$. The measurements were performed first at -30 °C, then -60 °C and -90 °C in order, and the time intervals between the measurements were 29 and 34 minutes, respectively.

K+C222·K⁻ are different ($\approx 3.4 \pm 0.1$ and $\approx 3.1 \pm 0.1$ eV, respectively). The structure of K+(15C5)₂·K⁻ is monoclinic [66], and the anion is isolated, so that the interactions between the anions are very weak. By contrast, K+C222·K⁻ is triclinic [67], and the distance between the potassium anions (4.90 Å) is less than the expected Van der Waals separation, and there is a considerable amount bonding character in the K⁻ · K⁻ interaction. Energy differences between the ns² and nsnp states associated with different alkalides were also observed by M. Faber [65]. In her optical absorption experiments on polycrystalline alkalide films, the spectra showed some shifts for the same anion in different complexant systems, as for example, the transition energy of $4s^2 \rightarrow 4s4p$ for the potassium anion shifted from 1.47 eV for K+C222·K⁻ to 1.51 eV for K+(18C6)₂·K⁻. She also found that the solvents from which the dried films were formed also affected the transition energies for the same alkalide, but the reason was unclear.

The sodides, Na+C222·Na- and K+C222·Na- have the same complexant system, but their photoelectron emission spectra show different threshold energies (≈ 3.1 ± 0.05 and ≈ 3.6 ± 0.05 eV, respectively). The reason for this may be due to their different structures, hexagonal for the Na+C222·Na- and orthorhombic for the K+C222·Na- [68,69]. Although the sodium anions in both compounds are rather isolated and with similar Na-H distances, they are not exactly in the same environment. The band states are formed from combinations of the wave functions of many sodium anions and surrounding molecules, and their energies relative to the vacuum level would be sensitive to structural differences. Based on these considerations and the experimental thresholds, we suggest that the

binding energy of the valence band electron is not solely determined either by the anion or by the complexant, but rather is influenced by the structure of the compound.

The onsets of the high energy peaks are not sharp for two reasons. One is that the emission from trapped electrons that lie in the band gap contributes to the onset signal. Another is the temperature effect, in that the lattice vibrations assist the lower energy electrons to transit to the vacuum level. Such phonon-assisted transitions had been observed in the optical absorption experiments of Na+C222·Na- thin films, in which the increase of temperature tended to broaden the absorption peak on the low energy side for the transition from the ground sate to the p-band state. The characteristics of the trapped electron states will be elucidated later.

Photoemission is mostly a volume process, in that electrons excited in the bulk are the main contributors to the emission. Although surface states also contribute to the photoemission, the total number of surface states is very small compared to the number of states in the bulk that can participate in the emission. In this experiment, the high energy peak was less temperature dependent than the low energy peaks. This is a characteristic of direct rather than indirect transitions. At the onsets of photoemission of the alkalides the photon energies were less than 4 eV and electron-electron scattering is unlikely at such low electron energies [70]. Therefore, we can suggest that the high energy peak of photoemission was due to bulk and direct processes, and that the electrons were unscattered by electron-electron interactions at the

onset of the emission. The photoemission theory developed by Kane [44] concluded that if the photoemission is a bulk process with direct transitions and unscattered transport, the quantum yield is proportional to $(\hbar\omega - E_T)$, in which E_T is the photoemission threshold energy. Based on this theory, we could extrapolate the straight line portion of the of the photoemission to intercept the X-axis in order to obtain the emission threshold energy for the valence band.

A comparison between the onset of photoemission of an alkalide with the work function of the corresponding metal also provides some useful information. The photoemission threshold energies, together with the work functions of the corresponding alkali metals are listed in Table 2-2. The threshold energies are higher than the work functions of the corresponding metals. Apparently, stabilization of the anions in the ionic lattice yields outer-shell electrons that are more strongly bound than those of the free electrons of alkali metals, even though the binding energy of the electrons in $M^{-}(g)$ is much weaker than in M(g).

An alternative argument suggests that the energy from the top of the valence band to the vacuum level corresponds to the onset of the low energy peak instead of the high energy peak. Strong evidence against this proposal is that for a nearly defect-free crystalline sample of Na⁺C222·Na⁻, the low energy band is absent, and only the high energy peak shows up in the spectra. (see Figure 2-9) The low energy bands do not always appear in the spectra of alkalides. In addition, the gap energy of Na⁺C222·Na⁻ was determined as 2.4 eV by conductivity measurements [2], whereas the onset of the low energy peak in photoemission is only ≈ 1.77 eV

Table 2-2. The photoemission threshold energies of the valence bands of alkalides and the work functions of the corresponding alkali metals.

Compound	Photoemission threshold energy (eV)
K+(15C5)2.K-	3.4 ± 0.1
Rb+(15C5)2.Rb-	2.9 ± 0.1
Na+C222.Na-	3.1 ± 0.05
K+C222.K-	3.1 ± 0.1
Cs+C222.Cs-	3.1 ± 0.05
K+C222.Na-	3.6 ± 0.05

Metal	Work function (eV)*
Na	2.75
K	2.30
Rb	2.16
Cs	2.14

^{*} Data from CRC Handbook of Chemistry and Physics, 71st editon (1991).

(700 nm). If the alternative argument were true, then the energy of the vacuum level would be below the bottom of conduction band, which is improbable. These facts provide strong evidence that the low energy emission peak is from some higher energy states rather than from the valence band. Due to the facts that the low energy band is strongly temperature-dependent and is extended to the near infrared, these high energy states are presumed to be electron-trapping states whose energies have a broad distribution in the gap.

We tried to measure photoemission from the electrides, $K^+(15C5)_2 \cdot e^-$, $K^+C222 \cdot e^-$ and $Cs^+(18C6)_2 \cdot e^-$, which are even more sensitive to the environment, especially to temperature. we could obtain photoemission signals from this class of compounds, the quantum yields were low (Figure 2-14 - 2-16). The spectra do not show appreciable photoemission on the low energy sides (IR range) as we expected for the electrides, which may be due to partial decomposition of the electrides or the presence of excess metal in the The photoemission was probably from a mix of metal, alkalide and complexant instead of from the trapped electrons of the Alkali metal formed by partial decomposition might react electride. with the left-over electride to form an alkalide. There might be some electride left, but the ratio between these components can't be known and the surface layers would be most subject to change. carefully checked the procedure of sample handling for measurement, and tried to find the causes for the decomposition. is possible that this occurred during sample loading and transferring, but it seems unlikely. Because the temperatures of the loading wand and the transport wand were measured and both were kept colder

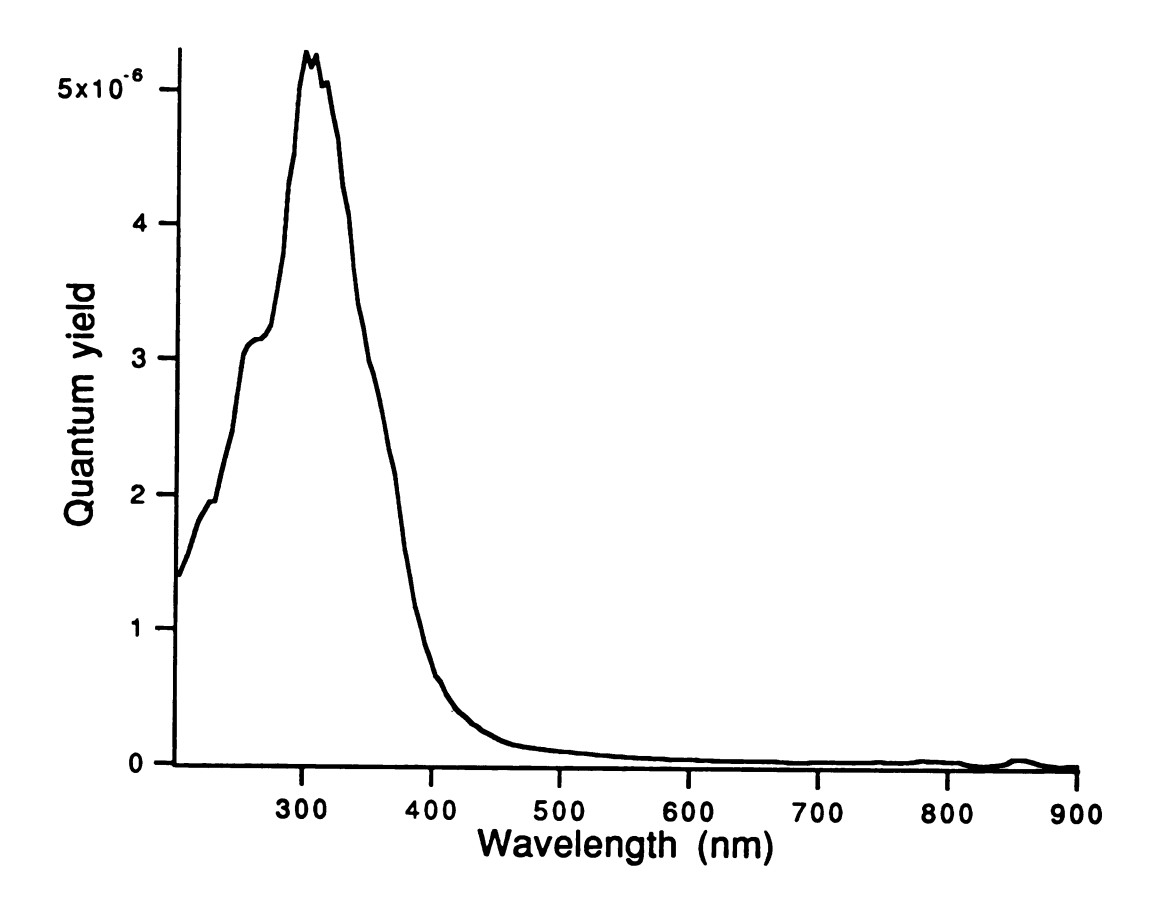


Figure 2-14. Quantum yield spectrum of K⁺C222·e⁻ at -60 °C. The spectrum doesn't show significant emission on the low energy side, which may be due to the decomplexation or decomposition of the sample or the presence of excess metal.

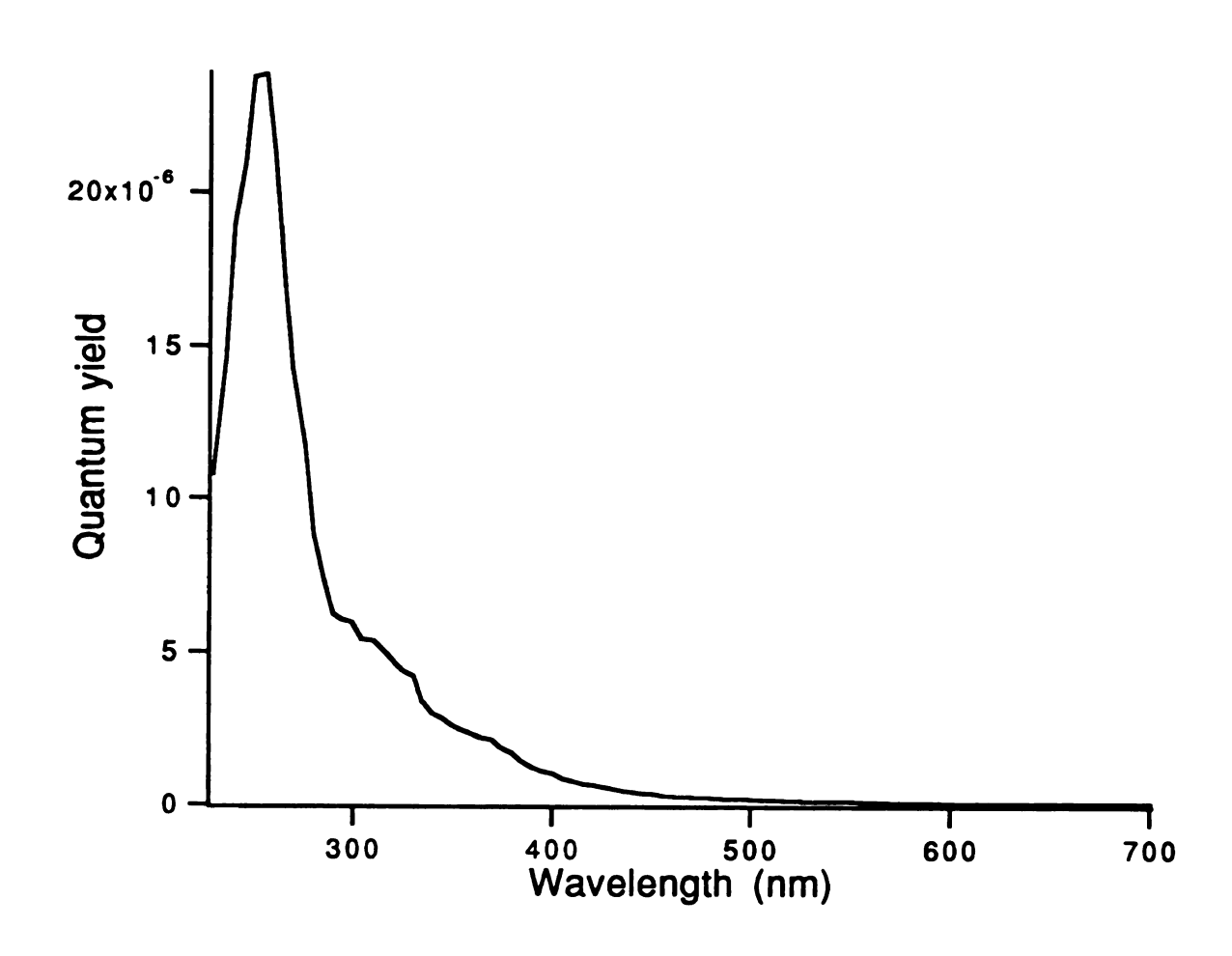


Figure 2-15. Quantum yield spectrum of $K^+(15C5)_2 \cdot e^-$ at -60 °C. The spectrum doesn't show significant emission on the low energy side, which may be due to the decomplexation or decomposition of the sample or the presence of excess metal.

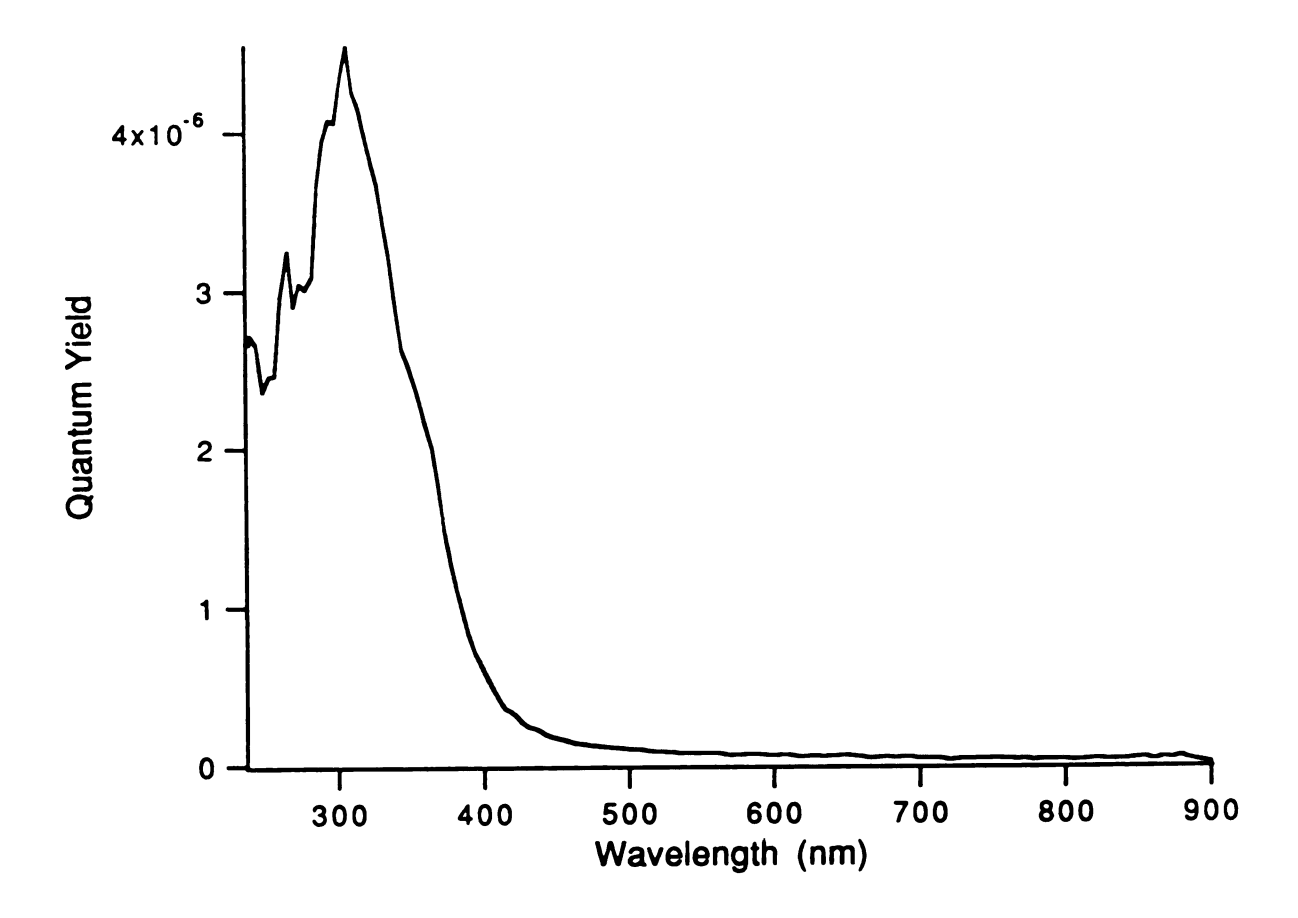


Figure 2-16. Quantum yield spectrum of $Cs^+(18C6)_2 \cdot e^-$ at -60 °C. The spectrum doesn't show significant emission on the low energy side. The saw-tooth shape on the high energy side is due to noise because the emission signal was weak.

than -60 °C, it is unlikely to be the cause of decomposition. On the other hand, other factors than temperature such as the presence of reactive impurities might be the cause. Another possibility for the decomposition may be the heat released into the sample when the solvent condensed at the time of film preparation. The heat released by condensation of dimethylether vapor at -60 °C is estimated to be When 0.05 ml was condensed from room temperature 32 KJ/mole. to -60 °C, it would release \approx 35 Joules of heat. We can't say all this heat released would go to raise the temperature of the sample because the heat could be absorbed by the sample cup, and the copper cup was cooled by cold nitrogen gas. However, at the moment of condensing, the solvent vapor contacted the sample, which might raise the temperature of the sample momentarily, especially the It is impossible to estimate how much the temperature surface. increased, but that might lead to partial decomposition of the electrides, because they are so temperature-sensitive. In any event, all attempts to measure the true photoemission spectra of electrides in this system have been unsuccessful. The conductivity measurement of Cs⁺(18C6)₂·e⁻ shows that the transition energy from the ground state to the conduction band is more than one eV, so that we cannot rule out the possibility that the observed photoemission spectrum for this compound may be due to a true signal. (Figure 2-16)

Fig. 2-17 shows the photoemission quantum yield of Na+C222·Na-, which has an emission peak at 290 nm presumed to be mainly attributed to the electron emission from the sodium anion valence electrons, 3s², to the vacuum. The polycrystalline film with

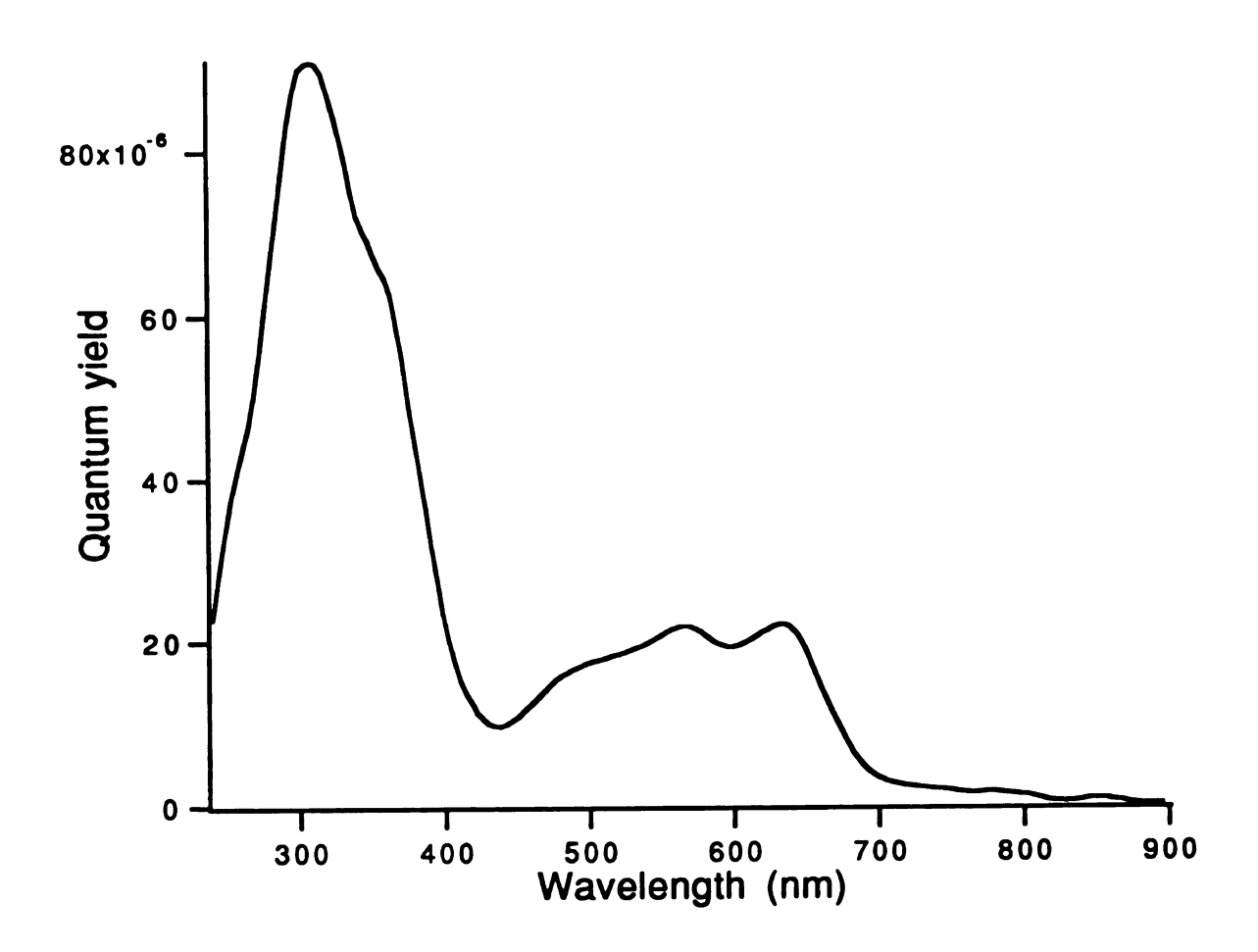


Figure 2-17. Quantum yield spectrum of Na⁺C222·Na⁻ (with trapped electrons present) at -60 °C. The high energy peak is mainly from the valence band, and the low energy peak (from 430 - 700 nm) is from trapped electrons.

defect states yields an additional shoulder at 360 nm and broad emission at 430 - 700 nm. The emission on the low energy side, presumed to be from trapped electrons [18, 71], is much higher in intensity than that obtained in previous work, performed under poorer vacuum conditions (10-4 torr) and a different loading procedure. This confirms the strong influence of vacuum environments and of appropriate sample loading. In past experiments [18], the sample was loaded inside a glove bag filled with inert gas, in which condensation of some moisture was more or less inevitable, and subsequently the water might react with trapped electrons as a scavenger, leading to a decrease in the photoemission of trapped electrons.

To verify that the photoemission was electronic instead of ionic, a set of Helmholtz coils 8 inches in diameter and with 150 turns on each side was set up, with the spectrometer in the center of the coils. It generated a magnetic field of 14 Gauss when one Ampere of current passed through the coils. Because the retarding effect is proportional to the mass of charged particle, smaller mass charged particles have smaller radii of a circular trajectory. An electron will be retarded a thousand times more than the lightest atomic ion under the same experimental conditions. Actually, under the conditions used, emitted electrons would return to the surface from which they are emitted. This method provides a clear way to distinguish whether the emission is from electrons or ions. If the photoelectron emission were from ions instead of electrons, a small magnetic field applied to the Helmholtz coils wouldn't have any obvious effect on the spectrum. If some range of the spectrum is partially from ions, the decrease of the signal would be much smaller than that of electrons. Figure 2-18 shows the photoemission quantum yield of Na+C222·Na- at various strengths of the magnetic field. The emission intensity decreased to 15 % when a magnetic field of 42 Gauss was applied, and it further decreased to 6 % in a magnetic field of 56 Gauss. The radii of the helical trajectories are estimated that they are 0.4 mm and 15 m for an electron and a sodium anion, respectively. Assuming that the initial emitting direction of the electron and the Na- is normal to the sample surface in a magnetic field of 56 Gauss.

Figure 2-19 shows the normalized decrease of emission intensities of Na⁺C222·Na⁻ at various wavelengths in different magnetic fields. The reducing rates of the emission intensities at different wavelengths were uniform, and the results strongly verify that the emission over the whole spectral range is electronic.

Figure 2-20 shows the stability of photoemission from Na+C222·Na- films versus time after the sample films were formed. Stability of the samples was always a concern, and it was affected mainly by the vacuum condition. The intense light beam should not be a problem because the light source was monochromatic, and the light spot on the sample spread over an area of 2x3 mm² instead of being concentrated at a point. For Na+C222·Na-, the emission intensity decreased only 5 % in 10 minutes at -60 °C at 350 nm; however, at 600 nm the decrease in the intensity could reach 21 %. Because the photoemission on the low energy side was presumed to be from the trapped electrons the more rapid decay is understandable since trapped electrons would have lower stability

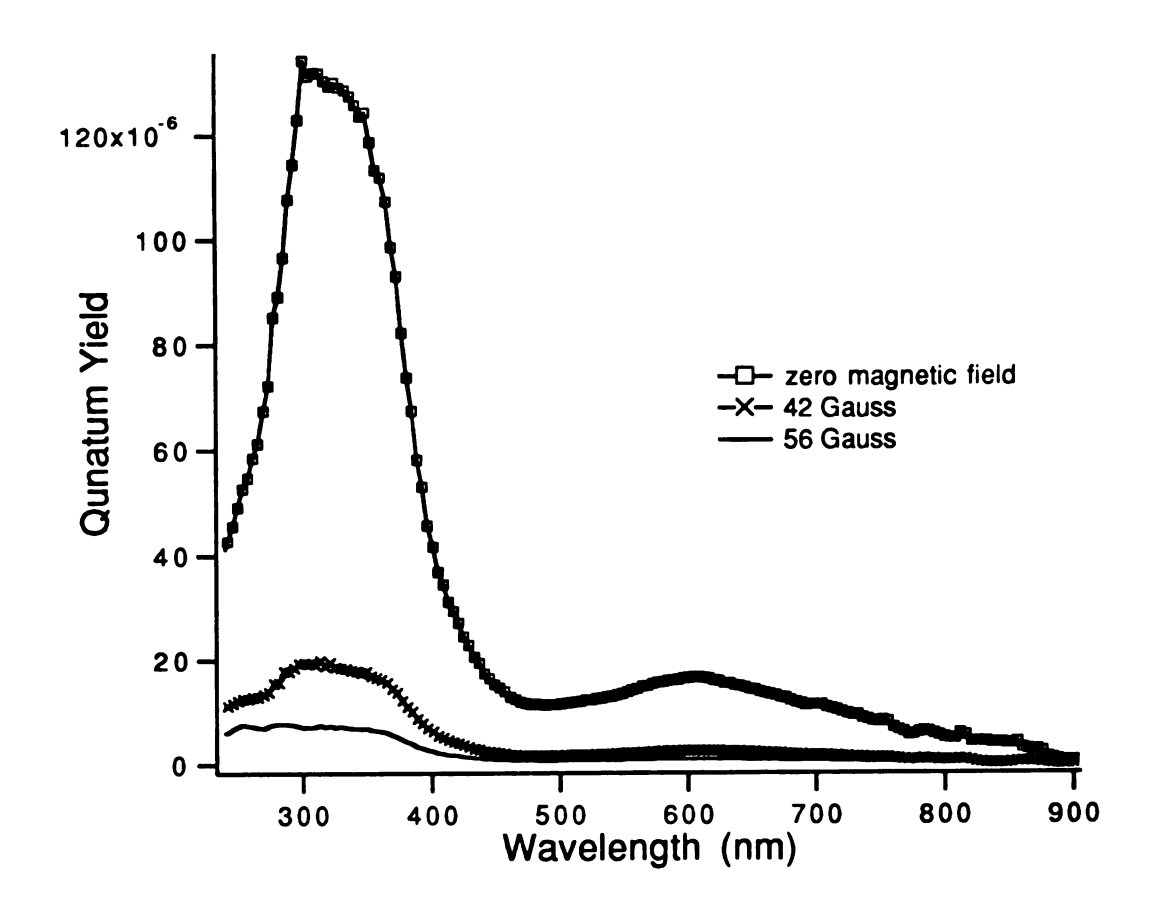


Figure 2-18. The reduction of the photoemission quantum yield spectrum of Na⁺C222·Na⁻ as a function of the magnetic field.

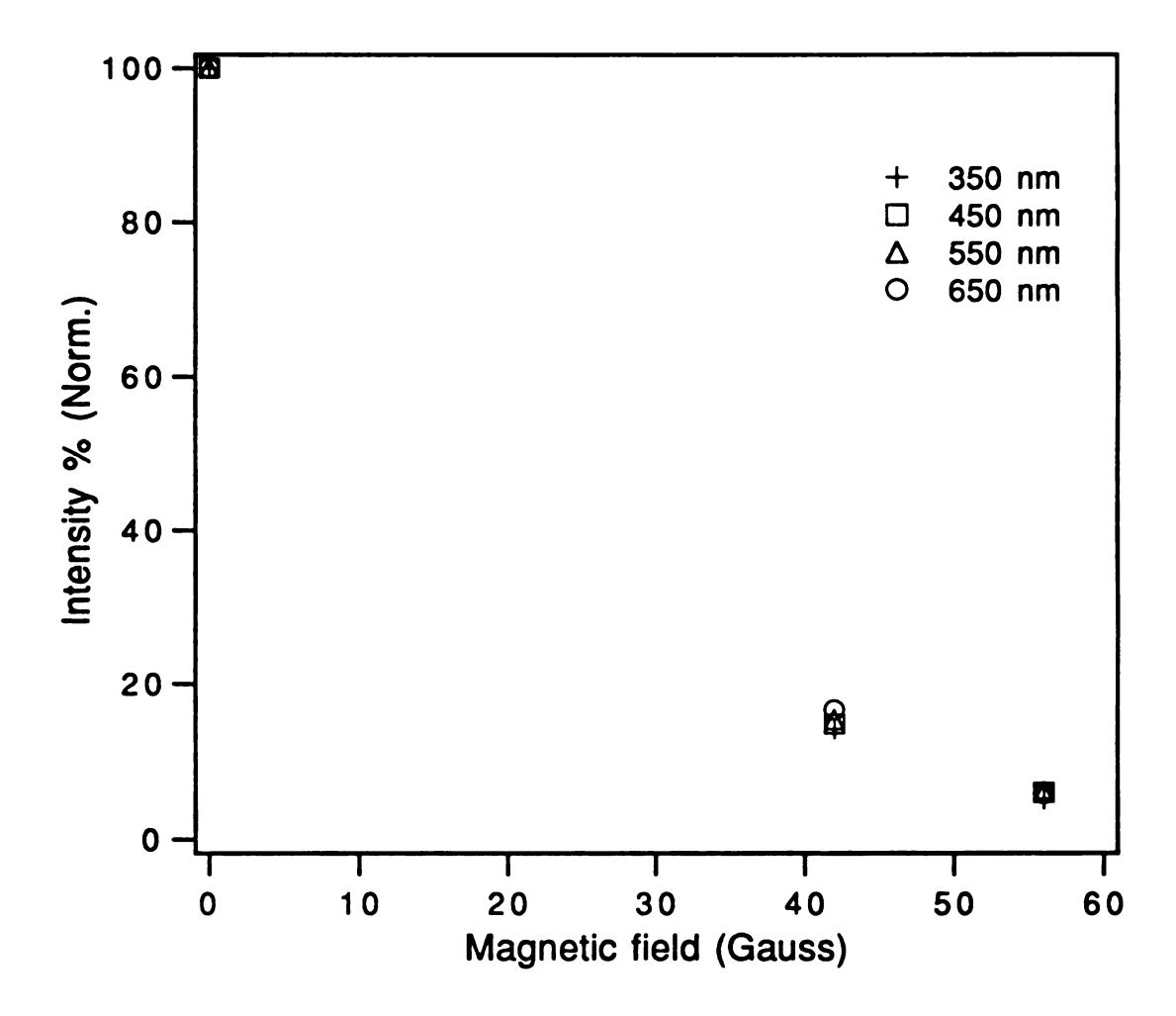


Figure 2-19. The normalized reduction of the photoemission intensity of Na⁺C222·Na⁻ at different wavelengths as a function of the magnetic field.

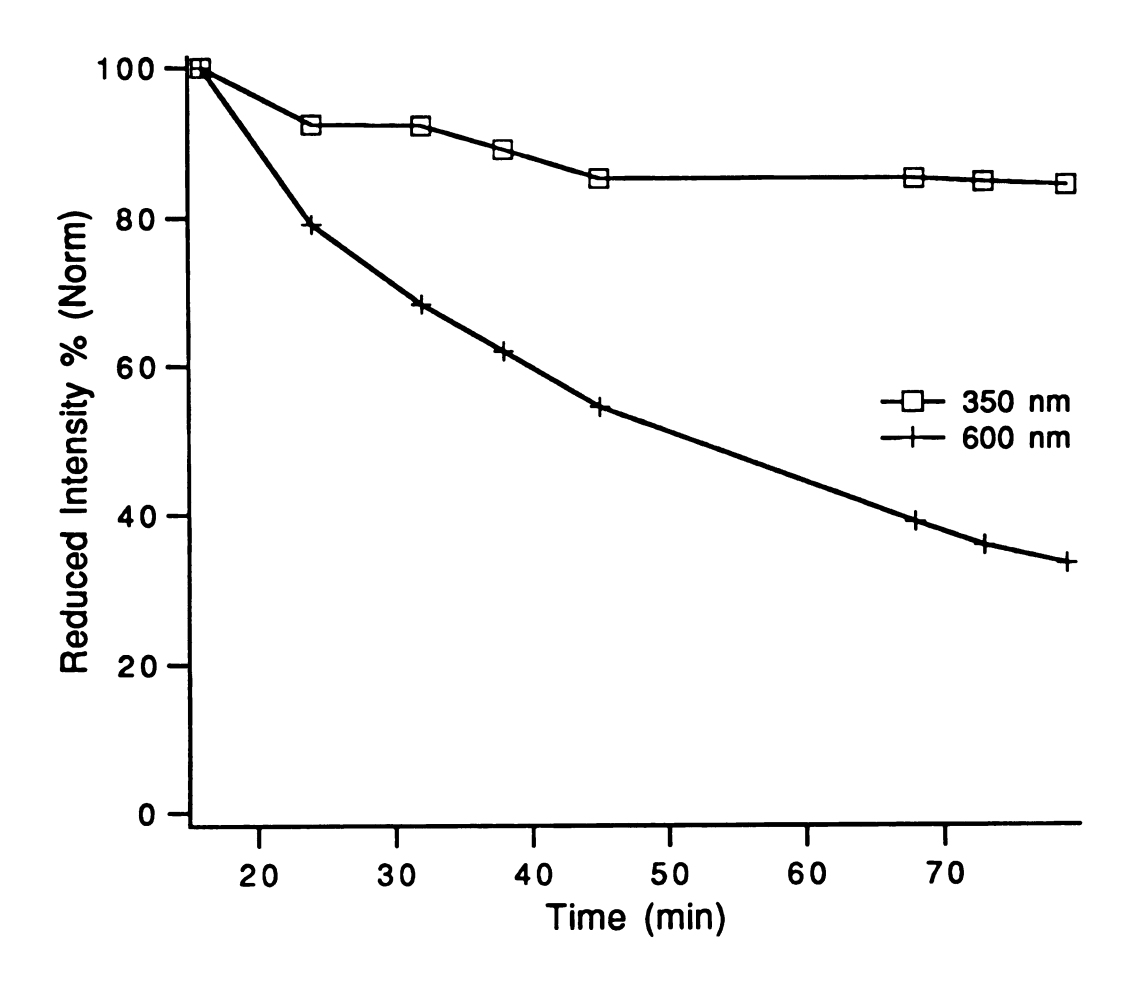


Figure 2-20. The time-stability of photoemission from Na⁺C222·Na⁻ at -60 °C.

than Na⁻. The stability was sample dependent, and most alkalides lasted more than 2 hours without apparent decomposition, which allowed us enough time to measure the photoemission under different experimental conditions.

Although the system has been used up to now for only photoemission studies of air- and temperature- sensitive materials, it could also be used for photoconductivity studies. All that would be required would be the modification of the vertical wand to one equipped with conductance patterns on the sample holder. Then the photoconductance signal would be able to be separated from the contribution of photoemission. Both the photoemission and photoconductance methods are very useful in exploring energy states in semiconductors.

CHAPTER III

THE PHOTOELECTRON EMISSION FROM Na+C222·Na-: EFFECTS OF LASER PULSES

III.A. Introduction

It has been known for a long time that when alkali metals are dissolved in alkylamines or polyethers, an equilibrium is established between solvated electrons and alkali metal anions. However, the nature of the solvated electrons, where the electrons reside and in what form they are present, is still debated. Alkali metal anions had been reported as existing in metal-ammonia [74], metal-amine and metal-ether solutions by optical spectra characterizations [75-77], although later studies showed that they are not present in metal-ammonia solutions [8]. The presence of alkali metal anions in the solid state was confirmed by the synthesis of alkalides, ionic salts that contain alkali metal anions [1, 8]. Among them, Na+(cryptand[2,2,2])·Na- (Na+C222·Na-) was the first compound crystallized and identified [1].

In Na+C222·Na-, the sodium cation is encapsulated in the cryptand, and the macrocyclic cryptand molecule serves to separate the positive and negative ions in the solid, such that the sodium anion resides outside of the cage and balances the positive charge. The crystal structure consists of close-packed cryptated cations with sodium anions in the pseudo-octahedral holes, and the structure has considerable anisotropy. Although, as with all alkalides, this sodide

is thermally unstable and is sensitive to air and moisture, it is the most stable alkalide synthesized to date and can be stable for several days at room temperature. In order to insure stability, however, it is synthesized and studied only *in vacuo* or in an inert atmosphere and at low temperatures, usually below -20 °C.

The physical properties of Na⁺C222·Na⁻ have been studied most intensively among all alkalides. The optical absorption spectra of thin films show a broad absorption peak at 1.91 eV and a shoulder at The main peak has the same position as for Na- in ethylenediamine and was assigned to the be sodium anion $3s^2 \rightarrow$ 3s3p bound-bound transition [3]. The shoulder, which does not appear in solution, was assumed to result from electronic excitation from the valence band 3s² to the bottom of conduction band, in agreement with both powder and two-probe single crystal conductivity measurements [2]. The conductivity measurements indicate that Na⁺C222·Na⁻ behaves as an intrinsic semiconductor with a band gap of ≈ 2.4 eV. The photoelectron emission spectrum from a rapidly dried Na+C222·Na- film had been previously measured under a low vacuum of 10⁻⁴ torr [18], and showed two peaks at 3.4 and 2.0 eV. The high-energy peak was less temperature-dependent and was attributed to direct emission of the electron from the valence band to the vacuum, while the low-energy peak was strongly broadened and increased more rapidly in intensity than the high-energy peak when the temperature increased. This emission peak was attributed to the photoemission of electrons trapped at lattice defect sites and was presumed to be an indirect process.

Luminescence spectra of crystalline Na+C222·Na- were studied by using a 50 picosecond pulsed dye laser at wavelengths between 560 and 618 nm (2.2 and 2.0 eV), which resulted in a narrow fluorescence peak. The peak position varied with temperature from 1.854 eV at 7 K to 1.828 eV at 80 K [4]. The time-resolved emission spectra, obtained by fitting the spectra with a double exponential function, showed that emission occurred from at least two closely spaced levels. On the high energy side of the band, the excitation occurred by absorption of photons in a $3s^2 \rightarrow 3s3p$ process, which both emitted radiation and further relaxed to a lower level from which the longer-time emission was observed. However, this picture was too simple to completely interpret the time-dependent spectral shape and the rate of decay on the high energy side. The role of exciton-polaritons [78, 101] and local exciton trapping [17, 102] have been recently described in detail.

Flash photolysis of the alkali metal anion, M-, in solution has been studied extensively; however such photolytic studies conducted in the solid state are more recent. Photolysis of Na- in solution caused a bleaching of the 650 nm absorption peak of the Na-absorption and the formation of a new absorption band in the infrared. The results were interpreted as the detachment of electrons from Na- to form solvated electrons, with recovery times that varied from milliseconds to seconds depending on the temperature and viscosity [79-81].

The laser photolysis of solvent-free Na+C222·Na- films showed [82] that a 15 ns pulsed dye laser at 605 nm with power higher than 1 mJ/mm² (peak power 6.6x10⁴ W) could bleach the 650 nm

absorbance of Na⁻, and a new absorbing species was created in the infrared simultaneously. The half-time of partial recovery is ≈ 30 ms at room temperature. The system did not return completely to its original state after the bleaching but rather a new set of absorbing species was established. The photo-bleaching effect was presumed to be due to the detachment of the electron from the sodium anion and its trapping at another trapping site, accompanied by partial decomposition.

Trapped electrons are commonly found in alkali halides and in frozen glasses, when the defect sites are added deliberately by irradiation or by "doping" with alkali metals [83, 84]. Photoemission studies of doped alkali halides yielded a low energy emission peak in the quantum yield spectrum whose position depended on the alkali halide studied [84].

Trapped electrons, e_t-, in frozen organic or aqueous glasses have being studied thoroughly by various methods, such as electron spin resonance, optical absorption, luminescence and electrical Suggested stabilization mechanisms for the conductivity [21]. trapped electrons are that the mobile electrons produced by radiation are first thermalized and stabilized through ion-dipole Further stabilization in the trap sites results from interactions. molecular orientation at rates that depend on the polarity of the matrix molecules and the temperature [25]. The absorption spectra of trapped electrons in glasses show a shift with time and temperature that strongly suggests that they are distributed among a continuum of trap depths rather than all being trapped with the The decay of trapped electrons, accompanied by a same energy.

blue shift, is better interpreted by trap deepening due to molecular orientation rather than by thermal detrapping and retrapping [24].

The present study focuses on laser photolysis of polycrystalline films of Na⁺C222·Na⁻ in which transient surface modifications are associated with photobleaching effects caused by nanosecond laser pulses. In this chapter we investigate the effect of laser irradiation on the photoelectron emission from Na⁺C222·Na⁻. The results are described in terms of possible structural changes and the creation of trapped electrons. A kinetic model for the redistribution of trapped electrons is suggested based on the recovery effects.

III.B. Experimental

Crystalline samples of Na⁺C222·Na⁻ were synthesized by methods described previously [6, 22], with crystal growth in a preevacuated (10⁻⁵ torr) glass cell at low temperatures. The primary solvent was methylamine and the second solvent trimethylamine, which was used to reduce the solubility of the Before adding the second solvent, the complexation compound. reaction between a sodium metal film and cryptand C222 was carried out for at least 12 hours at a temperature of -30 °C. At this or a lower temperature, the crystalline samples were grown by slowly evaporating the solvents starting methylamine/trimethylamine ratio of about 2:1. After removing primarily the more volatile methylamine, the product crystallized in the remaining solvent, which was rich in the less polar trimethylamine. The crystals were then washed five times with pure

trimethylamine in the same glass cell by condensation and filtration. After evaporating the remaining solvent, the sample was sealed in vacuo in small ampoules attached to the synthesis cell and stored in a liquid nitrogen dewar.

The photoemisson was measured with a 1000 watt xenon light source before and after irradiation with a pulsed laser. The xenon light was monochromatized with a scanning monochromator (Oriel model No. 77250) with gratings (Oriel #77296 and #77298) and a resolution of \approx 10 nm. The pulsed YAG laser was frequency-doubled to 532 nm by a KD*P (potassium dideuterium phosphate) crystal, and filtered by a pair of dichroic beam splitters (Spectra-Physics DHS-2). The pulse frequency was set in the manual mode, and the duration between the pulses was as long as 30 seconds to avoid accumulating heat on the sample, and to permit observation of the full timedevelopment of the effect of photo-bleaching. The diameter of laser beam is about 1 cm² which can completely cover the whole sample The light spot of the monochromatic xenon light spot is a trapezoidal shape with the size about 2x3 mm². Each laser pulse was 7 ns in duration and had an average energy deposition at the sample of 0.1 mJ/mm², as estimated from measurements by a laser power meter (Opher with -N type absorber head) and losses at the reflective mirrors and beam-splitter.

The spectrometer had the anode virtually grounded, and the cathode was biased at - 40 V to assure that the saturation current of photoemission would be obtained. The emitting current is shown in Figure 3-1 as a function of electric field. To perform quantum yield measurements, the grid for the retarding field was grounded to

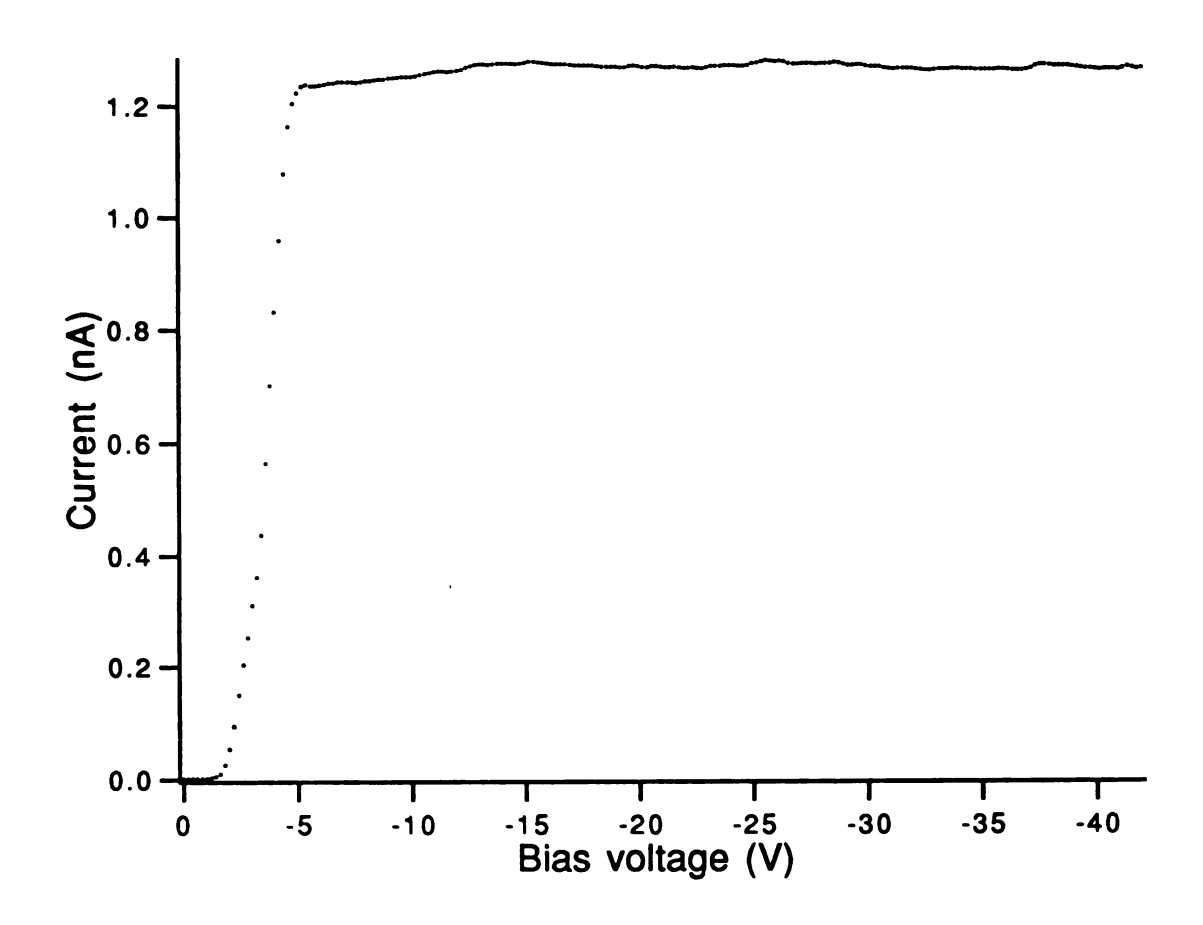


Fig. 3-1. The photoelectron emission current of Na⁺C222·Na⁻ at 400 nm and -60 °C versus imposed bias voltage. The current reaches plateau (saturation) when the bias voltage is larger than -5 V.

reduce the capacitance in the spectrometer. The response time of the spectrometer was measured to be \approx 40 ms. The signal was preamplified by a factor of 10^9 with a preamplifier inside of the vacuum system. It was then measured with an electrometer (Keithley 617). The noise background was \approx 2 pA. An IBM XT computer with an IEEE-488 Interface (from Metrabite) and a homebuilt stepper motor interface were used for the data acquisition. The former interface was used for the electrometer and the latter was for controlling the monochromator.

To make a film, the crystalline sample was introduced into the system under vacuum, placed in a copper cathode cup, and dissolved in methylamine by condensing the solvent vapor onto the sample at -60 °C. The solvent was then removed by evaporation into a liquid nitrogen trap to form a polycrystalline film, followed by evacuation with a cryogenic pump to remove any residual solvent (p = 10^{-6} torr). For determining the emission characteristic of nearly defectfree crystalline Na⁺C222·Na⁻, the crystals were merely wet with methylamine to renew the surface, followed by solvent evaporation. The emission spectra were measured under a vacuum of 10⁻⁸ torr. produced with a turbopump (Varian Model V300). The temperature was controlled (Omega model No. CN2001T-AT) with an accuracy of ±2 °C. The details of the photoemission system are described in Chapter 2. The quantum yield was calculated with the reference light intensity measured by a silicon photodiode detector (EG&G model NO. UV44430).

III.C. Results

Photoemission quantum yield spectra of polycrystalline Na+C222·Na- films were obtained at wavelengths from 240 - 900 nm. Figure 2-9 shows the spectrum of the photoemission from a collection of nearly perfect shiny crystals that were only slightly wet by methylamine prior to the measurement. The spectrum shows an emission peak at 290 nm and a very low emission on the low energy side above 400 nm wavelength. The main peak is less temperature dependent than the low energy peaks described later and is attributed to direct emission from the sodium anion. The quantum yield is in the range of 10⁻⁵ - 10⁻⁴. As shown in Figure 2-9, laser pulses had practically no effect on the emission spectrum of this sample. Figure 3-2 shows the emission spectrum at -60 °C from a more typical Na⁺C222·Na⁻ thin polycrystalline sample prepared by solvent evaporation from completely dissolved samples. The spectrum shows, in addition to the high energy peak at 290 nm, a shoulder at 360 nm and a broad emission band in the range 500 -700 nm. The lower energy emission bands are presumed to result from defect electrons, due to their strong temperature dependence and the absence of such bands in a good crystalline sample. Samples of this type presumably contained both defect sites and excess defect electrons produced by the fast solvent evaporation process.

The emission characteristics of these films were easily modified by the pulsed laser presumably because of the presence of lattice defects at which electrons could be trapped. As shown in Figure 3-2, the nanosecond doubled Nd:YAG laser at 532 nm had no appreciable effect on the emission below 290 nm. However, after several

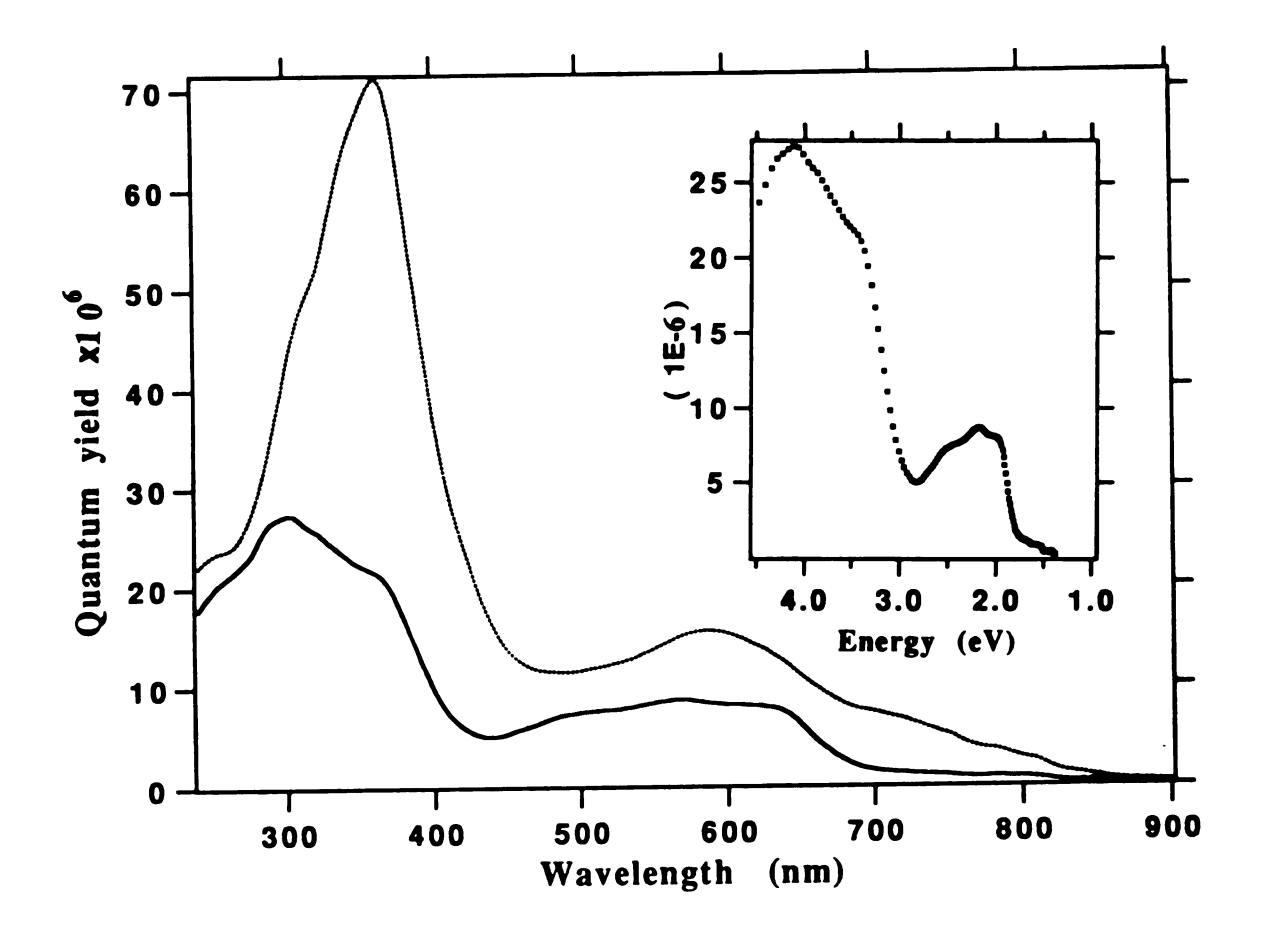


Figure 3-2. Photoemission quantum yield spectra of a Na⁺C222·Na⁻polycrystalline sample at -60 °C. The solid line is the original emission spectrum; the dashed line is the emission spectrum after the sample was illuminated by a number of laser pulses. The inset shows the pre-irradiation quantum yield spectrum as a function of the photon energy of the xenon light - monochromator system.

prof of regilive ord mo 400 Fig tra fol

succ

w

an

ef

W

1

n

f

ť

successive laser pulses, with time intervals = 30 seconds, there was pronounced enhancement of the emission at 360 nm and in the range of 500 - 900 nm. The increase of emission in the lower energy region is assumed to result from population of initially empty, longlived defect sites by electrons that are excited by the laser pulses. In order to study the photolysis effects in more detail, we set the monochromator to pass the xenon light at both 600 nm (2.07 eV) and 400 nm (3.1 eV) during the period of consecutive laser pulses. Figure 3-3a shows that when the xenon light is set at 400 nm the transient response of electron emission during the laser pulse is followed by a decay to a steady-state. Figure 3-4b shows that when the xenon light is set at 600 nm and additional laser pulses are used, the emission intensity decreases abruptly following the laser pulses, and then increases slowly to a new steady-state value. The same effects were observed when the xenon light was first set at the wavelength of 600 nm, and then at 400 nm. (Figures 3-4a and 3-3b which can be compared with Figures 3-3a and 3-4b) A common characteristic is that the steady-state emission intensity increased after each laser pulse until a saturation condition was reached, after which additional laser pulses had little effect.

Figure 3-5 shows the recovery behavior at different temperatures, -95, -60 and -30 °C. Note that recovery rate at 600 nm decreases with an increase in temperature. Analyses of the data by fitting the derived equations will be discussed later. When the intensity of the xenon light was modified by using neutral density filters, Figure 3-6 shows that the more intense the light the faster the recovery to steady-state at 600 nm. The recovery and decay

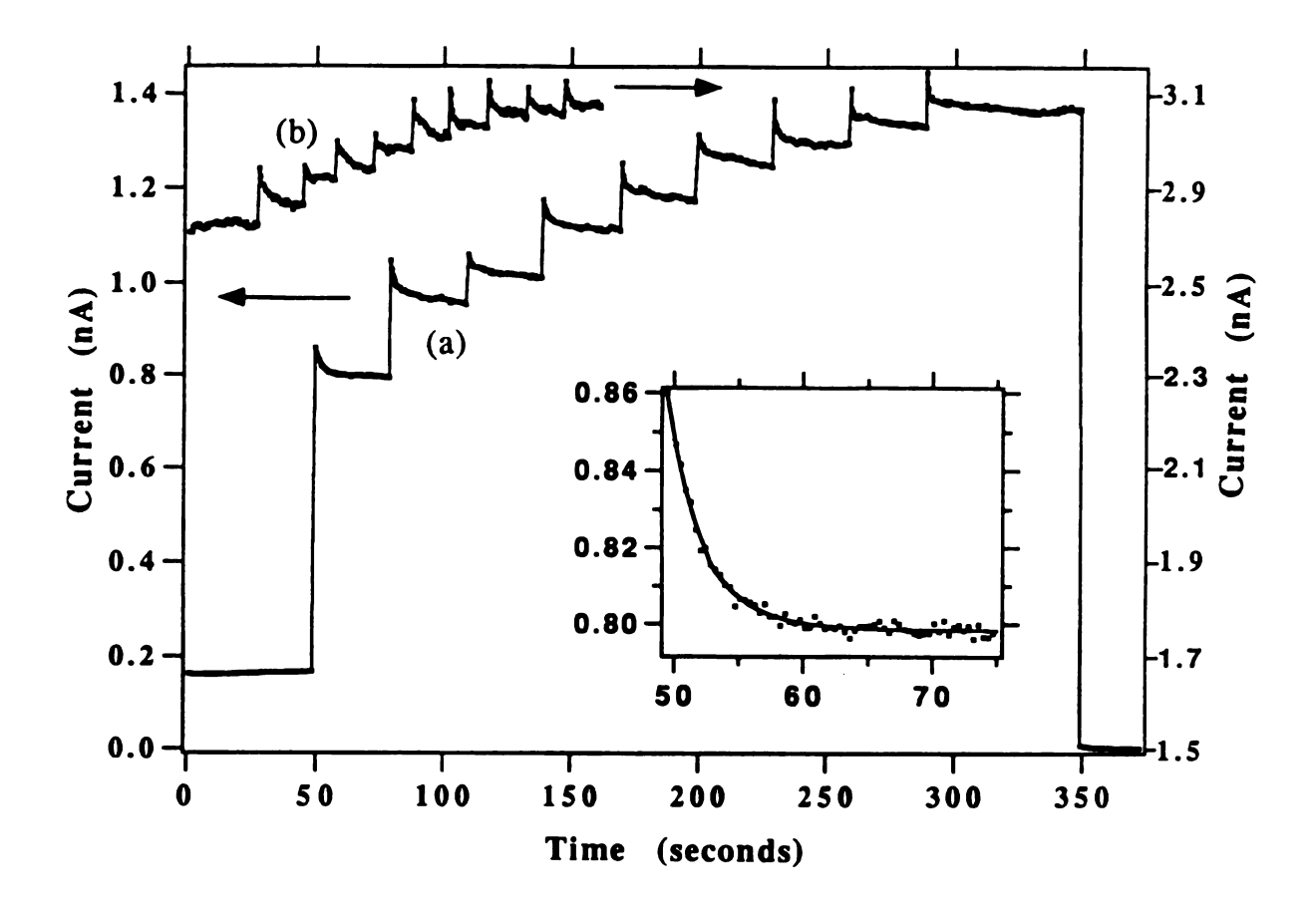


Figure 3-3. The response of the photoelectron emission current at -60 °C of a Na⁺C222·Na⁻ polycrystalline thin sample to successive 532 nm laser pulses as analyzed with 400 nm xenon light. The lower curve (a) shows the response of a fresh sample, while the upper curve (b) shows the response of a separate sample that had been previously pulsed repeatedly and analyzed with 600 nm xenon light (curve a in Figure 3-4). The inset shows the decay kinetics of the fresh sample after the first pulse. The solid line is the least-squares fit by an exponential with $k = 0.36 \pm 0.03$ s⁻¹. The decay after subsequent laser pulses also showed a slow component (see text).

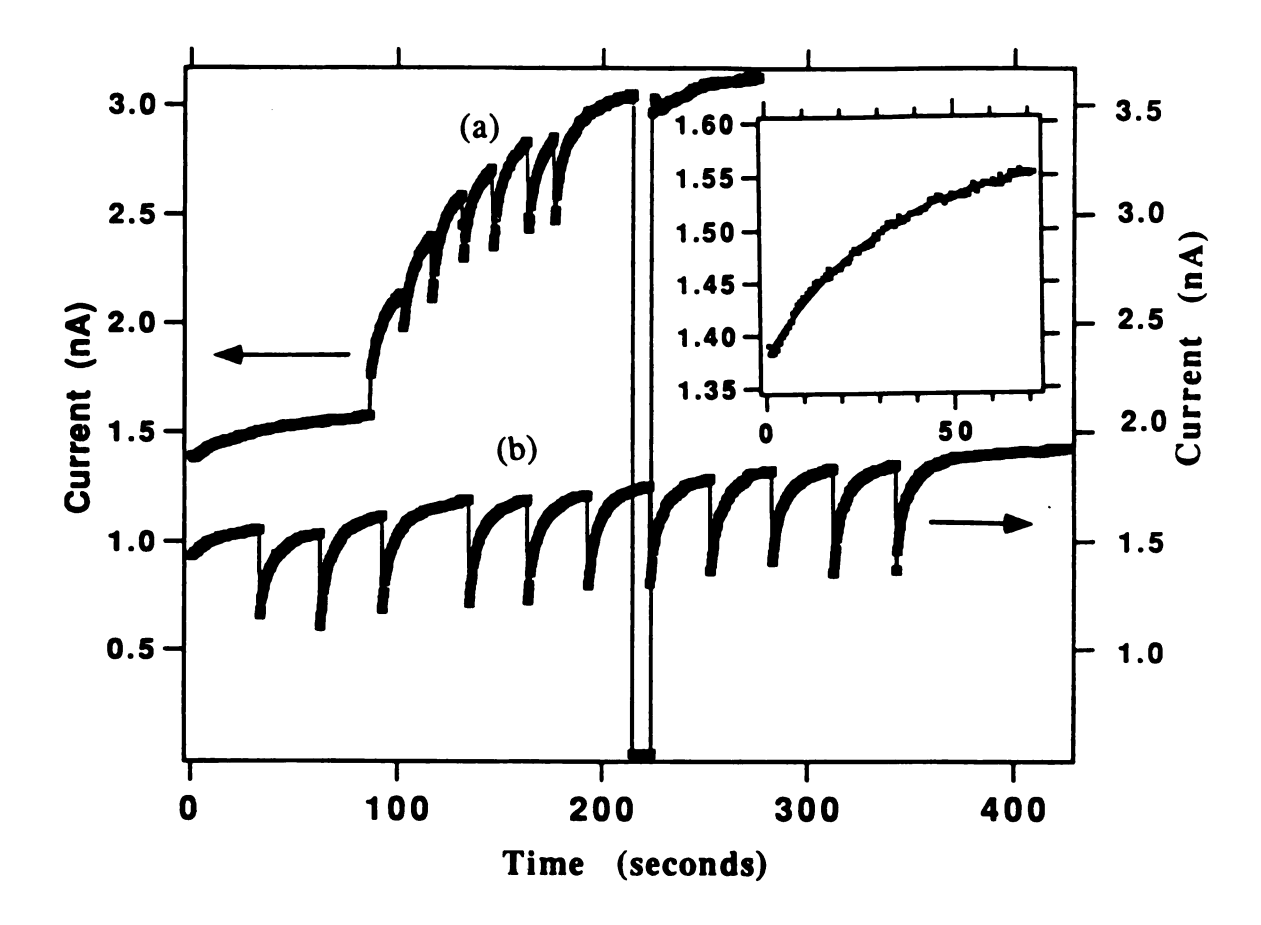


Figure 3-4. The response of the photoelectron emission current of a $Na^+C222\cdot Na^-$ polycrystalline thin sample to successive 532 nm laser pulses as analyzed with 600 nm xenon light (curve a). The drop to zero after seven pulses shows the dark current obtained by interrupting the xenon light. The inset shows the growth upon illumination with the 600 nm xenon light before laser pulsing. The solid curve is the least-squares fit by a simple exponential with rate constant $0.0305 \pm 0.0006 \, s^{-1}$. The lower curve (b) shows the behavior of a separate sample that had been previously pulsed repeatedly and analyzed with 400 nm xenon light (curve a in Figure 3-3). Note the slight relative increase per pulse.

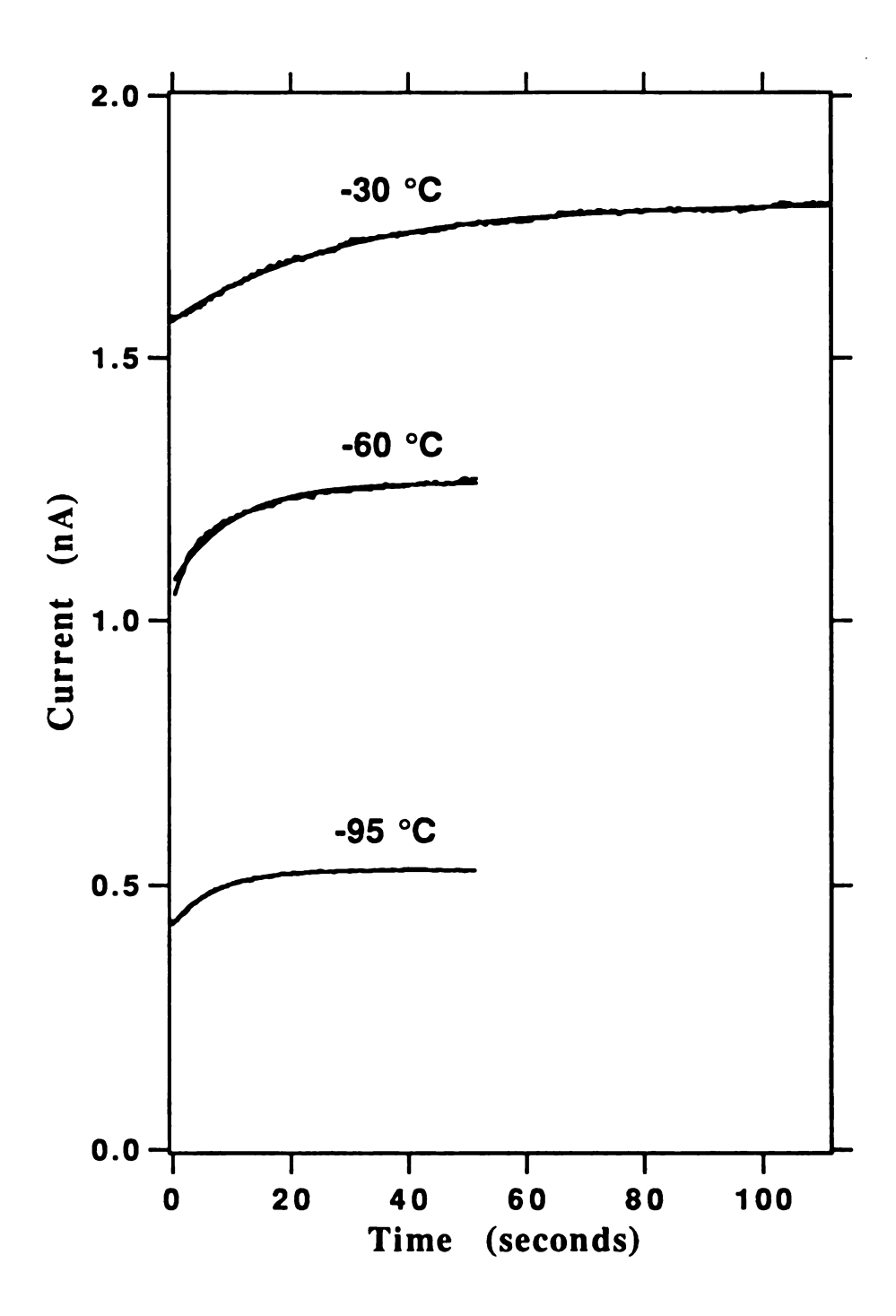


Figure 3-5. Growth of the photoelectron emission current of Na+C222·Na- at 600 nm after 532 nm laser pulses at three temperatures. Note the increase in current and the decrease in growth rate as the temperature is increased.

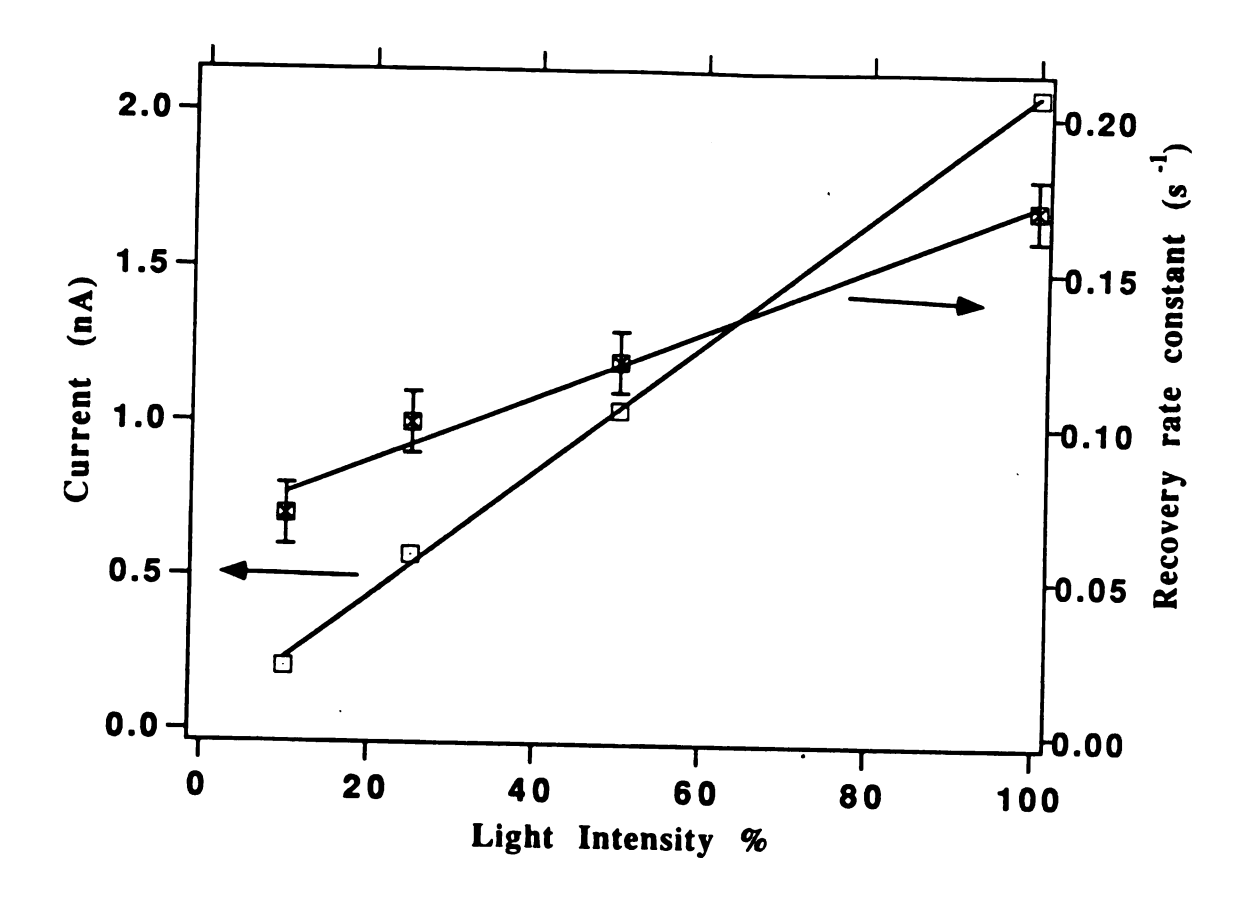


Figure 3-6. Linear dependence of the photoelectron emission current of Na⁻C222·Na⁻ (open squares) and of the recovery rate constant (crosses in squares) on the 600 nm xenon light intensity after 532 nm laser pulses. Note that the intercept of the former is zero, while that of the latter is 0.065 ± 0.005 s⁻¹, close to the value obtained from a direct measurement of the thermal decay (see Figure 3-9).

rates are the result of competition between replenishment of empty trap sites by the light from the xenon lamp, which populates the traps by excitation from the valence band, and the thermal decay toward an equilibrium state. The electron emission from trapped sites appears to be an indirect process since it is so sensitive to temperature. When the xenon light was set at other wavelengths between 500 and 700 nm, we also observed intermediate effects, including a decrease followed by an increase. (see Figure 3-7)

A magnetic field of ≈ 14 Gauss was applied during a test of the system to confirm that the emission was from electrons instead of ions. Effects due to artificial response of the circuits were also ruled out by studying the photoemission from an evaporated potassium film and bare copper under the same vacuum condition used with samples. No time-dependent artifacts were observed from the metals except for the circuit rise time of 40 ms.

III.D. Discussion

The experimental facts may be summarized as follows:

- (1). I_{em} is proportional to n_i where n_i is the concentration of trapped electrons in level i and I_{em} is the emission current.
- (2). I_{em} is strongly temperature dependent, with increased emission at higher temperature (Figure 3-5).
- (3). When the xenon light is turned off, a steady-state is reached after seconds to minutes such that n_i decays exponentially with time to a dark equilibrium value (Figure 3-9).

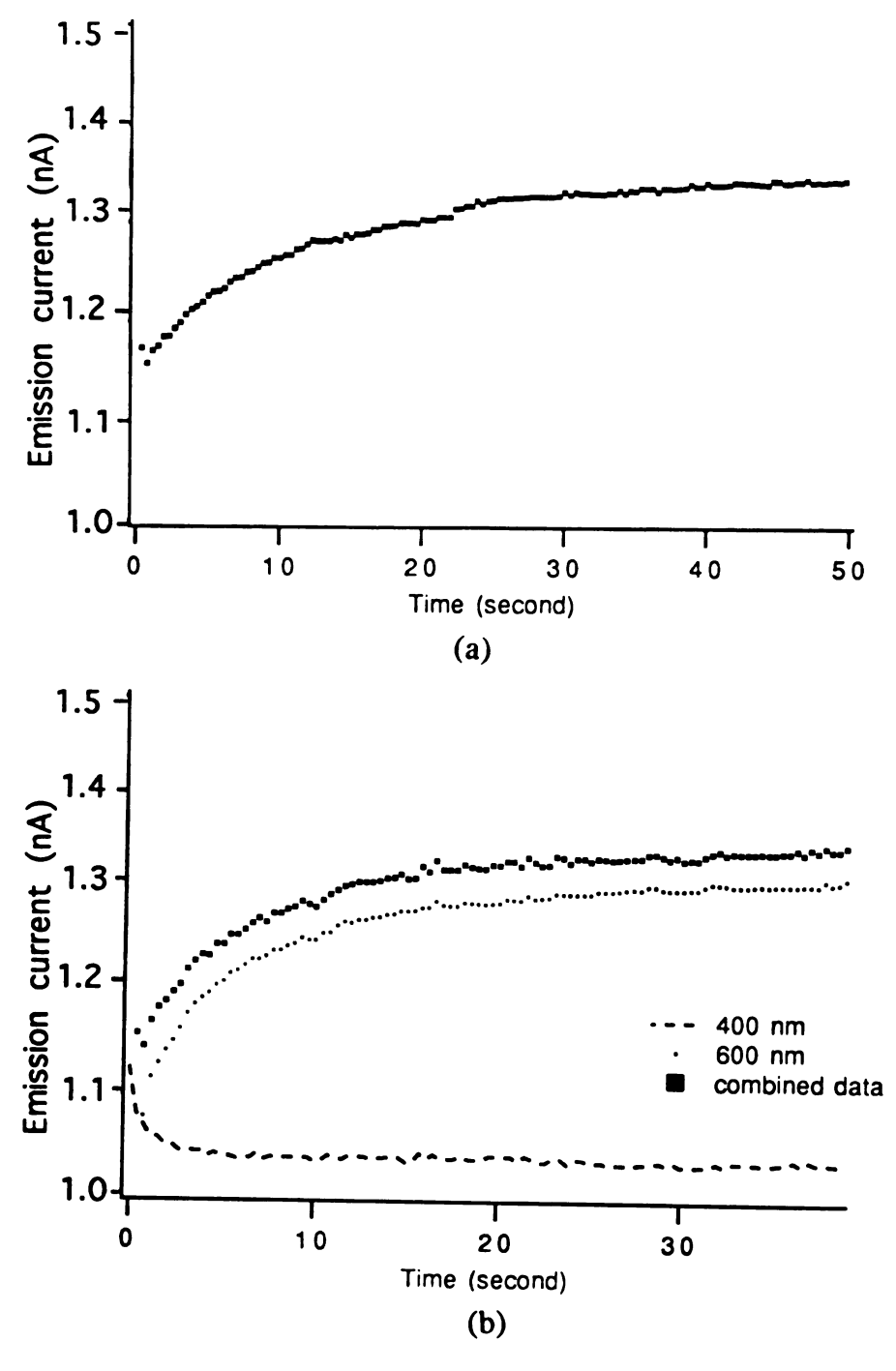


Fig. 3-7. (a) Photoemission from Na⁺C222·Na⁻ at 500 nm xenon light and -60 °C after the laser pulse, (b) the combination of the electron emissions at 400 nm and 600 nm after the laser pulses. Figure b is the sum of the photoemission intensities at 400 and 600 nm, decreased by 2.0. One can see that Figure a and the calculated curve in b are nearly the same.

- (4). Depletion of n_i within 530 nm of the vacuum level occurs during the laser pulse when compared with the steady-state value of n_i (Figure 3-4).
- (5). Enhancement of n_i within 400 nm of the vacuum level occurs during the laser pulse when compared with the steady-state value of n_i (Figure 3-3).
- (6). Repeated pulses lead to a constant steady-state value of n_i after 4 6 pulses. The biggest jump occurs with the first pulse (Figures 3-3a and 3-4a).
- (7). The rate constant for the growth of n_i after a pulse, monitored at 600 nm is directly proportional to I, the xenon light intensity, when first-order growth is assumed (Figure 3-6).
- (8). The growth rate constant decreases with increasing temperature when first-order kinetics are used (Figure 3-5).
- (9). The decay rate constant from the "full light" value of n_i in the dark is 0.06 to 0.07 s⁻¹ at -60 °C (Figure 3-9). This is also the zero light intensity intercept of a plot of the rate constant versus I_{xenon} at -60 °C (Figure 3-6).
- (10). The initial and steady state emission currents are directly proportional to I (Figures 3-6 and 3-9).
- (11). The decay amplitude (400 nm) decreases as we approach saturation but the growth amplitude is relatively constant (600 nm) (Figures 3-3a and 3-4b).

We first provide qualitative explanations of the effect of laser irradiation on the emission characteristics of Na⁺C222·Na⁻ and then develop a model to explain the kinetics. The basis for the explanation is the schematic energy diagram shown in Figure 3-8, in

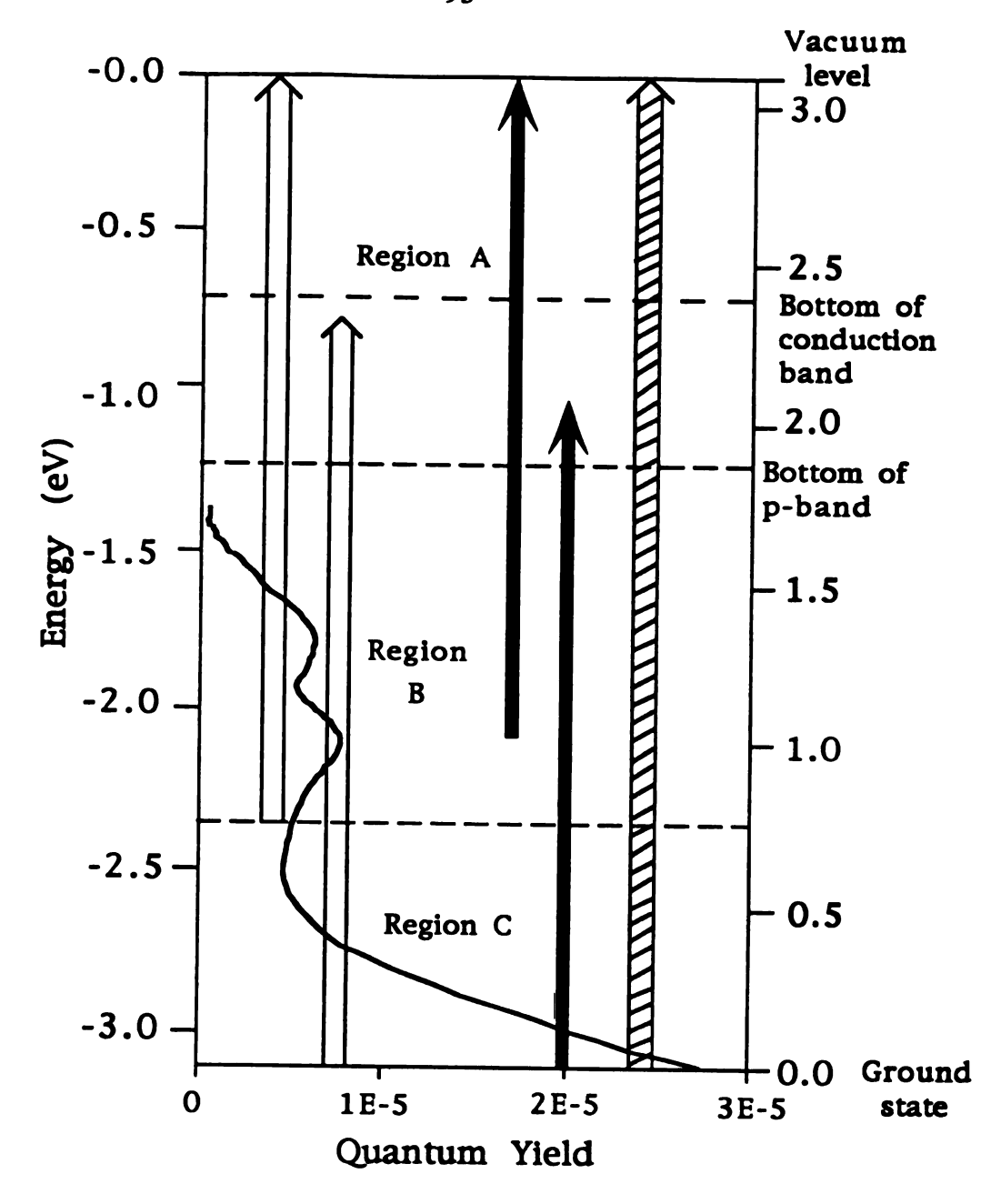


Figure 3-8. Energy diagram of Na⁺C222·Na⁻ related to photoelectron emission. The solid curve is the excess quantum yield that results from a number of laser pulses with 600 nm xenon analyzing light, plotted versus energy, and is obtained from the data shown in Figure 3-2. The open arrows represent the energy of 532 nm laser photons, the solid arrows that of 600 nm photons, and the shaded arrows that of 400 nm photons. The regions A, B, C represent electron trap energy regions that have different types of behavior (see text).

which the zero of energy is at the top of the $3s^2$ valence band. The bottom of the 3s3p band is at 1.84 eV based on fluorescence studies [4] while the bottom of the conduction band is at ≈ 2.4 eV based on conductivity measurements [2].

The vacuum level is ≈ 3.1 eV above the valence band edge. This is determined by extrapolating the straight line portion of the high-energy peak (290 nm) to zero emission. The high-energy peak is not very temperature dependent, suggesting that the emission is primarily direct, rather than indirect. According to the theory developed by Kane [44] for photoemission by bulk, direct processes without electron-electron scattering, the quantum yield is proportional to $(\hbar\omega - E_T)$, in which E_T is the threshold energy.

The breadth of the photoemission spectrum due to defect electrons is so large that we presume the existence of defect traps at various energies as represented by the short solid lines in Figure 3-8. Furthermore, it is clear that trap-to-trap migration of electrons at equilibrium is very slow, probably because of the spatial separation of the traps and low electron mobilities.

It is possible that the laser pulses generate additional trapping sites or cause chemical or structural changes at the surface. If so, however, this does not seem to alter the photoemission response of the compound. The photoemission spectrum of defect-free crystals is unchanged by the laser pulses, suggesting that new traps are either not formed or are not involved in subsequent photoemission. Also, the effect of laser irradiation decreases after 4 - 6 pulses, which again suggests that additional traps are not formed as a result of the laser pulses.

The picture that emerges from such considerations is that the initial samples contain both empty and filled defect sites, distributed over a wide energy range. Examination of Figure 3-2 shows that the defect electron concentration after laser irradiation is 3 - 4 times as high as before, with peak positions of spectra lying 3.4 eV and 2.0 eV below the vacuum level, but distributed over a wide range of energies.

The laser photon energy is too small for single photon induced electron emission from the ground state of Na- but it is high enough to transiently populate the p-band. Other studies [82, 86] show that high-power laser pulses can alter the absorption spectrum of thin films of this sodide, so that it is not surprising that the laser pulses increase the trapped electron concentration. In addition, we anticipate that the laser pulse will tend to "sweep-out" trapped electrons that are within 2.33 eV of the vacuum level.

The laser power is critical to the analysis of the effect of laser pulses. The energy deposited by the 532 nm laser pulses is ≈ 0.1 mJ mm⁻². This is close to, but below, the threshold for photobleaching of absorbance (≈ 0.2 mJ mm⁻²). At much higher power levels, the photoemission disappeared after a single pulse, presumably because of photo-decomposition on the surface.

Photons from the xenon lamp at 600 nm (2.07 eV) are not only able to cause photoemission from trapped electrons that are 1.0 eV or more above the valence band, but they can also populate states below 1.84 eV by electron transfer from the p-band to vacant traps. This results in steady-state photoemission from a higher population of trapped electrons than are present in the dark. Interrupting the

light results in thermal decay of these excess electrons with a first-order rate constant of 0.06 - 0.07 s⁻¹. (see Figure 3-9) Restoration of the light causes a slow increase in the photoemission intensity. Both the rate and the steady-state level achieved are proportional to the light intensity. It is important to note, however, that the order of 80 % of the final steady-state emission current is obtained immediately upon illumination. This again provides evidence for the presence of long-lived trapped electrons.

The temporal behavior after a laser pulse when 600 nm xenon light is present can be explained on the basis of the observations described above. Unless saturation has already occurred from previous laser pulses, the immediate effect of the laser pulse is to increase the photoemission current by increasing the number of trapped electrons with energies that are at least 1.0 eV above the ground state. However, depletion of pre-existing trapped electrons in this energy range leaves empty traps that can be filled from the p-band and replenished by the xenon lamp. Thus, the emission current grows until a steady-state is reached. Competition between trap-filling and decay of the p-band excited Na by fluorescence and radiationless decay causes the return to steady-state to be slower at higher temperatures where the steady-state p-band population is smaller.

When the xenon light comes from the monochromator at 400 nm the results are very different. At this wavelength, any trapped electrons above the ground state can be emitted (indeed even some emission from Na⁻ is expected). The result is that the laser pulse causes a net overpopulation of trapped electrons that decay

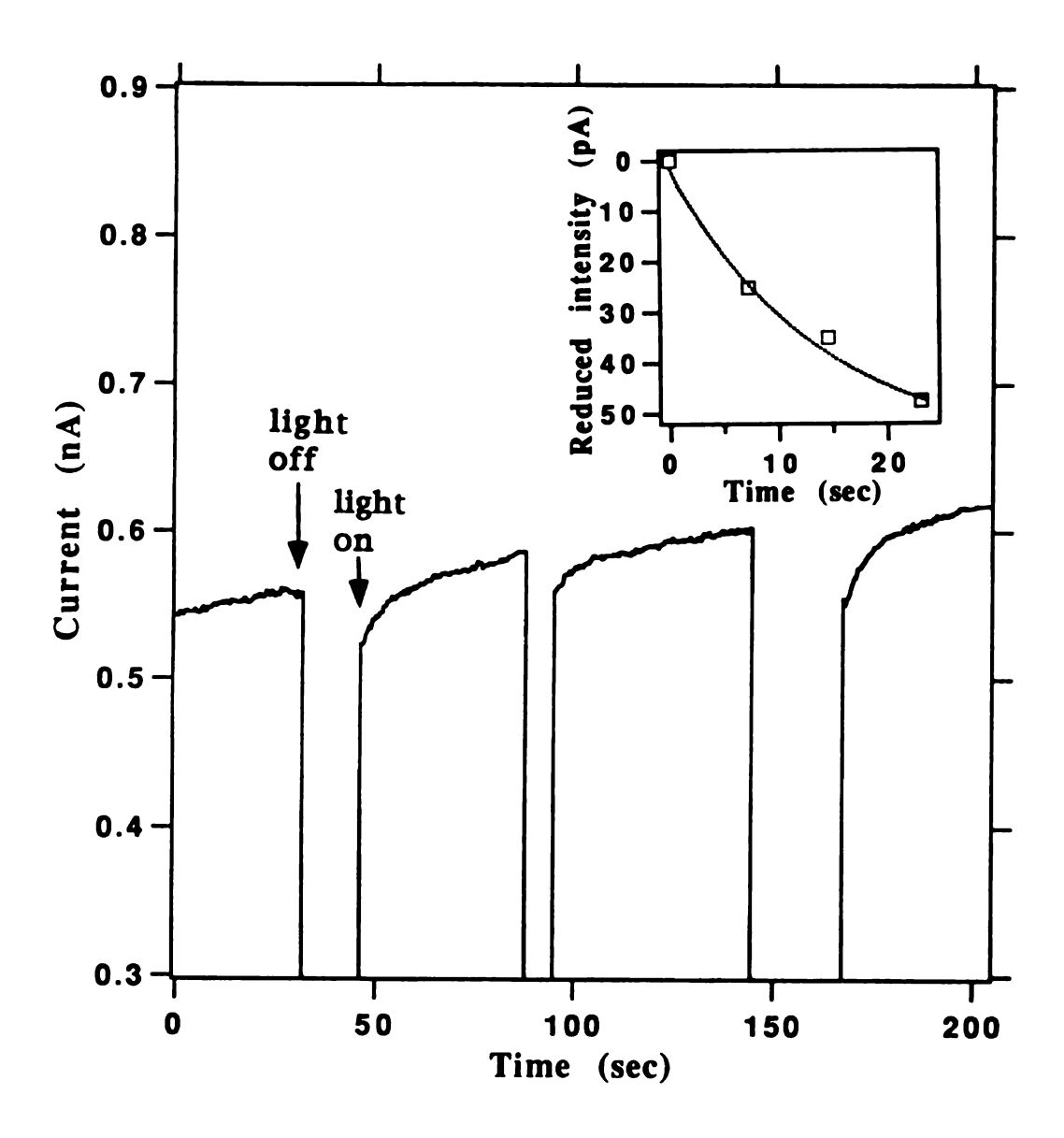


Figure 3-9. Sequence used to determine the thermal decay rate of Na⁺C222·Na⁻ in the absence of laser pulses. The decrease in signal intensity upon turning on the 600 nm xenon light after a variable dark period is plotted in the inset versus the length of the dark period. During the dark period the emission current was zero. The estimated rate constant for exponential thermal decay (dotted line in the inset) is between 0.06 and 0.07 s⁻¹.

SĮ ai la en ele reg the the thermally to a lower steady-state population. The competition between these two effects is particularly clear at intermediate wavelengths (500 nm) in which decay first occurs to a level below the steady-state level, followed by slow growth to the steady-state level (Figure 3-7).

These qualitative explanations can be put into more quantitative terms with the aid of a few assumptions about relative rates.

When the xenon light is set at 600 nm, the photons can emit trapped electrons that lie within 2.07 eV of the vacuum level, and also pump the laser induced excess electrons in the region within 2.33 eV of the ground state to the higher energy traps. At the same time this light will excite valence band electrons to replenish depleted shallow trap sites. Therefore, the concentration of trapped electrons is a result of the competition process between the thermal decay of laser induced excess electrons and the population of the depleted shallow trap sites. The effects can be seen in Figure 3-10, where the emission first decays and then slowly recovers. The spectrum can be deconvoluted into two separate processes, decay and recovery, with the equations derived from the models described later.

In comparison, when the xenon light is at 400 nm the photon energy can emit any trapped electrons and even the valence band electrons to the vacuum. The emission is from an overpopulated region because of the presence of laser-induced excess electrons in the deep trap sites. Therefore, the emission intensity is high at first, then decays to the steady-state value. No obvious recovery growth

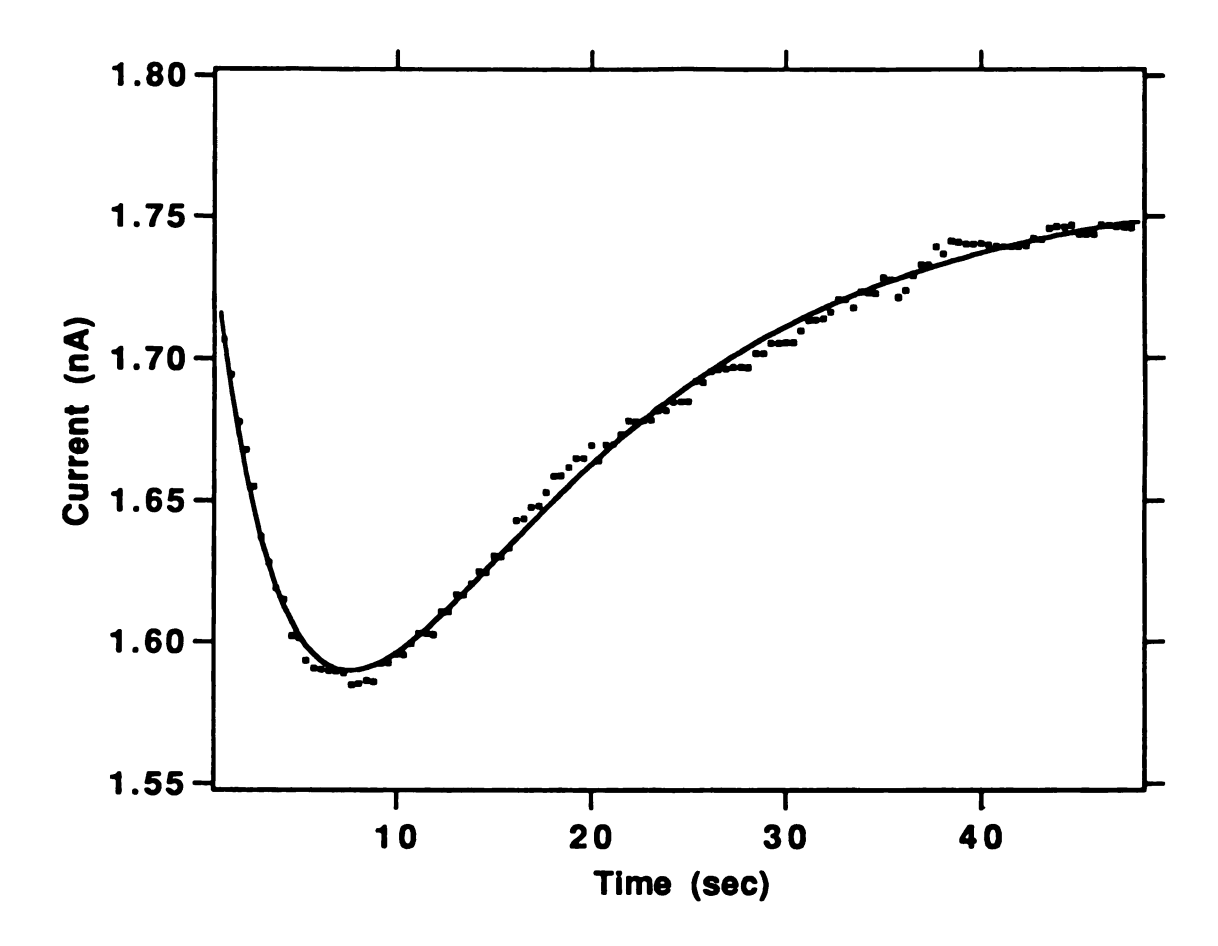


Figure 3-10. Decay and growth of the photoelectron emission current of Na⁺C222·Na⁻ after a 532 nm laser pulse at -30 °C with analysis by 600 nm xenon light. The solid line is the fit of these data by two exponentials with rate constants of $0.23 \pm 0.01 \text{ s}^{-1}$ (decay) and $0.070 \pm 0.004 \text{ s}^{-1}$ (growth).

is observed, probably because the photon-excited electrons at this wavelength are effectively quenched because they are in the conduction band or in a high-energy p-band.

From the previous qualitative observations and presumptions, two models are suggested to explain the recovery effects. The photon-excited electrons from higher energy states proceed to relax into empty trapping sites at lower energies, or else excited Na- states at the bottom of the p-band, either fill traps or return to the ground state by fluorescence and radiationless decay.

Based on the first model, the energy states of the trapping site can be divided into 3 regions (Figure 3-8):

- (a) Deep trapping sites $\sum_{a}^{N} n_a$, which are filled with laser-induced excess electrons, from which the electrons will not be emitted by 600 nm (2.07 eV) photons to the vacuum, but only to higher energy (shallow) trapping sites. Since photoemission from this region is only allowed by the 400 nm light, at this wavelength only decay of the photoemission current is observed after the 532 nm laser pulse. Such decay is biphasic. The fast component ($k \approx 0.4$ s⁻¹) decreases in magnitude with successive pulses while the slower component ($k \approx 0.09$ s⁻¹) remains significant.
- (b) The medium trapping sites $\sum_{b}^{m} n_b$, which are depleted by the laser pulse but are filled by laser-excited excess electrons. These trapped electrons can be emitted to the vacuum by 600 nm xenon light, and the empty states can also be refilled by electrons that are excited from deep traps and from the valence band. A net enhancement of the final trapped electron concentration is observed,

resulting from the laser pulse and 600 nm xenon light repopulation of traps.

(c) Trapping sites that are 2.33 eV or more above the ground state $\sum_{c}^{p} n_{c}$, which are depleted by the laser pulse, but are not refilled by the laser induced excess electrons. These trapped electrons can be emitted to the vacuum, and the empty traps will be refilled by the photon-excited electrons from the deep traps and the valence band (when 400 nm analyzing light is used). The concentration of trapped electrons in this region is too low to show long-time photoemission that is significant on the scale of photoemission intensities from the other regions.

In the first model the kinetic mechanism for the recovery from photobleaching by 600 nm xenon light would be

$$\frac{d\sum_{a}^{N} n_{a}}{dt} = C_{a} I k_{g} - (I k_{o} + k_{t}) \sum_{a}^{N} n_{a}$$

$$\frac{d\sum_{b}^{m} n_{b}}{dt} = C_{b} I k_{g} + C_{b}^{'} I k_{o} \sum_{a}^{N} n_{a} - (I k_{e} + k_{t}) \sum_{b}^{m} n_{b}$$

$$\frac{d\sum_{c}^{p} n_{c}}{dt} = C_{c} I k_{o} \sum_{a}^{N} n_{a} - (I k_{e} + k_{t}) \sum_{c}^{p} n_{c}$$
(3-1)

where C_a and C_b are the coefficients for the excitation of electrons from the ground state to fill the trap sites of $\sum_{a}^{N} n_a$ and $\sum_{b}^{m} n_b$, I is the xenon light intensity, k_g is the quantum yield for the excitation of electrons from the valence band to higher energy trap sites, k_e is the quantum yield for the emission of trapped electrons to the vacuum, k_i is the rate constant of thermal relaxation of trapped electrons, k_o is the quantum yield for the emission of deep trapped electrons to the shallow traps, and C_b and C_c are the coefficients for the emission of trapped electrons from states $\sum_{a}^{N} n_a$ to states $\sum_{b}^{m} n_b$ and $\sum_{c}^{p} n_c$, respectively.

The photoemission intensity I_{em} at 600 nm is the sum of electron emissions from 2.07 eV below the vacuum level, which includes region C and part of region B.

$$I_{em} = Ik_{e} \left[c_{\rho} B(t) + C(t) \right], \tag{3-2}$$

where c_p is a constant factor. The total emission can be obtained by solving the Equation 3-1 (with the assumption $k_e \approx k_o$),

$$I_{em} = X + (Yt + Z)\exp^{-(Ik_e + k_t)t}.$$
 (3-3)

The analyses of the recovery at 600 nm with this equation will be discussed later. This model does not explain the anomalous temperature-dependent recovery rates (slower at higher temperature). This mechanism also includes too many detailed processes, some of which may not be important.

In order to interpret the temperature-dependence of the recovery rate, another model is suggested in which the trapping states are filled from the bottom of the p-band and the lifetime of Na⁻ ions in the p-state decreases with an increase in temperature [4]

tr

fl

in pl

ra

en

rai

wh site

pu

Co

(see Figure 3-8). This would decrease the repopulation rate of the trapping sites as the temperature increases.

The concentration of excited Na^- ions in the p-band, n_p , is an equilibrium between the promotion rate and the decay rate by fluorescence and radiationless decay,

$$\frac{dn_p}{dt} = k_E I - k_f n_p,\tag{3-4}$$

in which I is the light intensity, k_E is related to the cross-section for photon absorption, and k_F represents both fluorescence and radiationless decay. Thus, in steady-state,

$$n_p = \frac{k_E}{k_f} I \tag{3-5}$$

If the major cause of trap-emptying is thermal relaxation to lowerenergy states (including the ground state) with rate constant k_T , the rate of change of trapped electron concentration, $\frac{dn_e}{dt}$, is given by

$$\frac{dn_{\epsilon}}{dt} = kn_{\rho}(n_{\iota} - n_{\epsilon}) - k_{\iota}n_{\epsilon}, \qquad (3-6)$$

where k is the refilling rate constant from the p-band to the trapped sites, n_i is the initial empty trap concentration produced by the laser pulse and n_e is the concentration of electrons in these traps. Combination of equations (3-5) and (3-6) gives

$$\frac{dn_{e}}{dt} = \left(\frac{kk_{E}}{k_{f}}\right)I(n_{i} - n_{e}) - k_{T}n_{e} \tag{3-7}$$

The photoemission intensity I_{em} at 600 nm is proportional to the density of trapped electrons in the appropriate region. The solution to Equation 3-7 can be expressed as an exponential function,

$$I_{m} = A + B \exp^{-[Ik^{2} + k_{i}]t}, \tag{3-8}$$

where
$$k$$
 is $(\frac{kk_E}{k_f})$, A is I_m^m , and B is $-(I_m^m - I_m^0)$.

Neither Equation 3-3 nor Equation 3-8 yields a complete fit of the recovery of the photoemission at -60 °C. The approximate rate constants are $\approx 0.15 \pm 0.01$ s⁻¹ for the former and $\approx 0.23 \pm 0.02$ s⁻¹ for the latter. The suggested mechanisms do not precisely describe the photobleaching effects. However, the latter model is preferred rather than the former one since it can interpret the temperature-dependence of the recovery rates.

To complete the analysis of the growth rate, a slow growth rate equal to that obtained with a fresh sample (0.0305 s⁻¹, see the inset in Figure 3-4) must be included. Thus, the complete expression for the growth of the emission intensity is

$$I_{-} = A + Be^{-kt} + Ce^{-0.030t} \tag{3-10}$$

The agreement of this equation with the data from repeated pulses is shown in Figure 3-11.

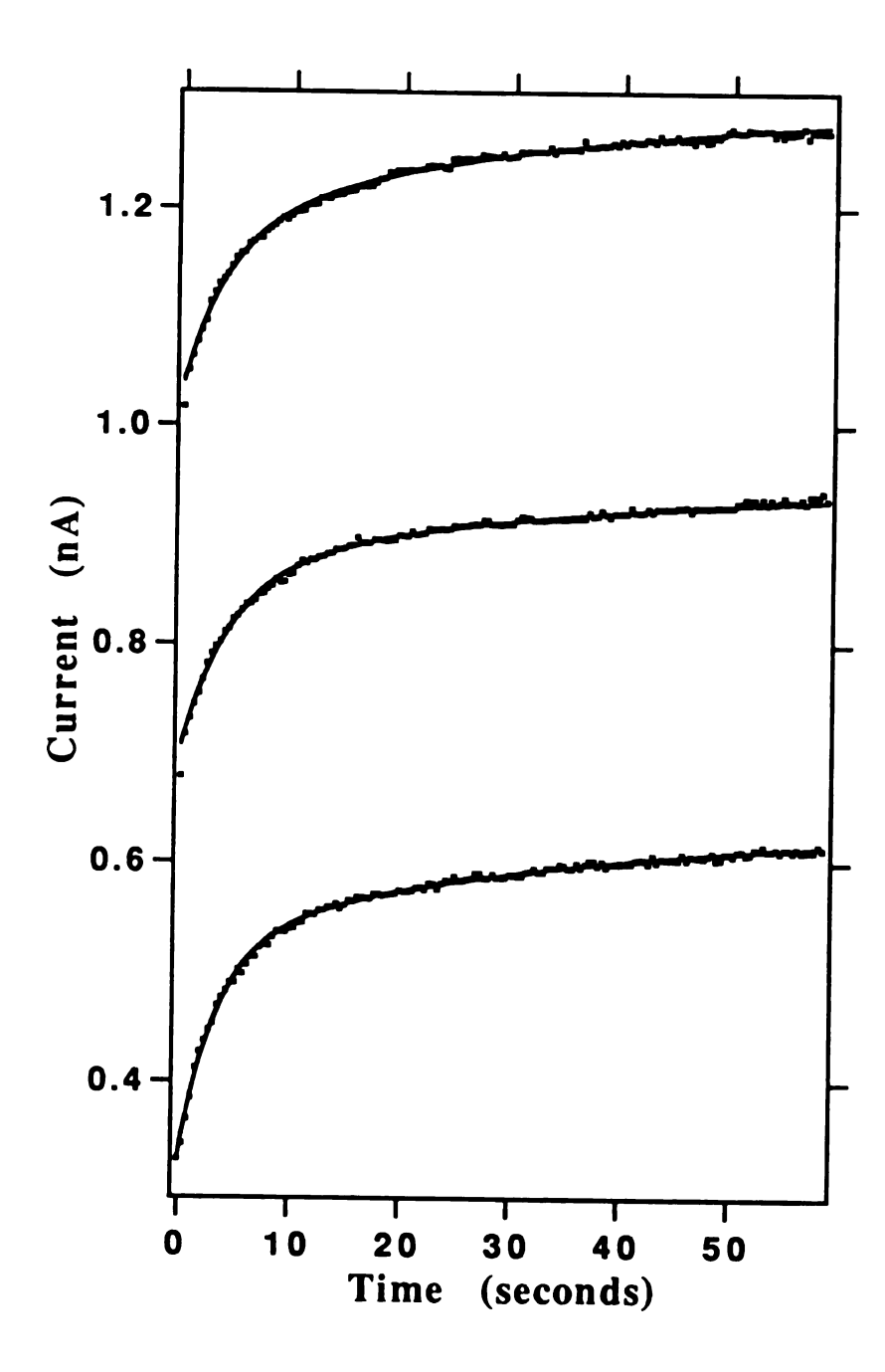


Figure 3-11. The least-squares fit of three successive photoelectron emission growth signals of Na⁺C222·Na⁻ after 532 nm laser pulses at -60 °C by Equation 3-10, a double exponential function in which the slower rate constant is not adjusted, but is determined from the growth rate prior to laser irradiation. Successive curves are displaced by 0.4 nA for clarity of presentation.

When the xenon light is set at 400 nm, the energy of the photons (3.1 eV) is high enough to emit electrons from any of the trapped sites and also from the valence band. Light of this wavelength can also pump electrons from the valence band to all trapped sites, probably through the bottom of the conduction band or a higher p-state, but the excited electrons may be efficiently quenched in the conduction band.

If the trapped electrons in Region C had long enough lifetimes, it was reasoned that two-photon absorption would yield enhanced photoelectron emission. In Figure 3-12, low intensity IR laser (1064 nm, 1.1 mJ mm⁻² per pulse with duration 0.2 ms) were intermittently combined with 400 nm xenon light. After illumination of the polycrystalline film sample with the 400 nm xenon light, turning on the IR laser pulse trains (pulse rate of 10 Hz) resulted in increased emission that continued to grow to a saturation level during exposure to both beams. When the xenon light was blocked, the emission abruptly dropped to a lower level and then continued to decrease slowly toward zero. An exponential fit of the decay data, assuming no emission at infinite time yielded a rate constant of 0.0044 ± 0.0003 s⁻¹. This indicates that long-lived traps within 1.2 eV of the vacuum level can be populated by 400 nm light. Illumination of the sample with 600 nm light followed by continuous IR laser pulses at low intensities had practically no cooperative effect. This is expected since the 600 nm photons have too low energies to populate many traps within 1.2 eV of the vacuum level.

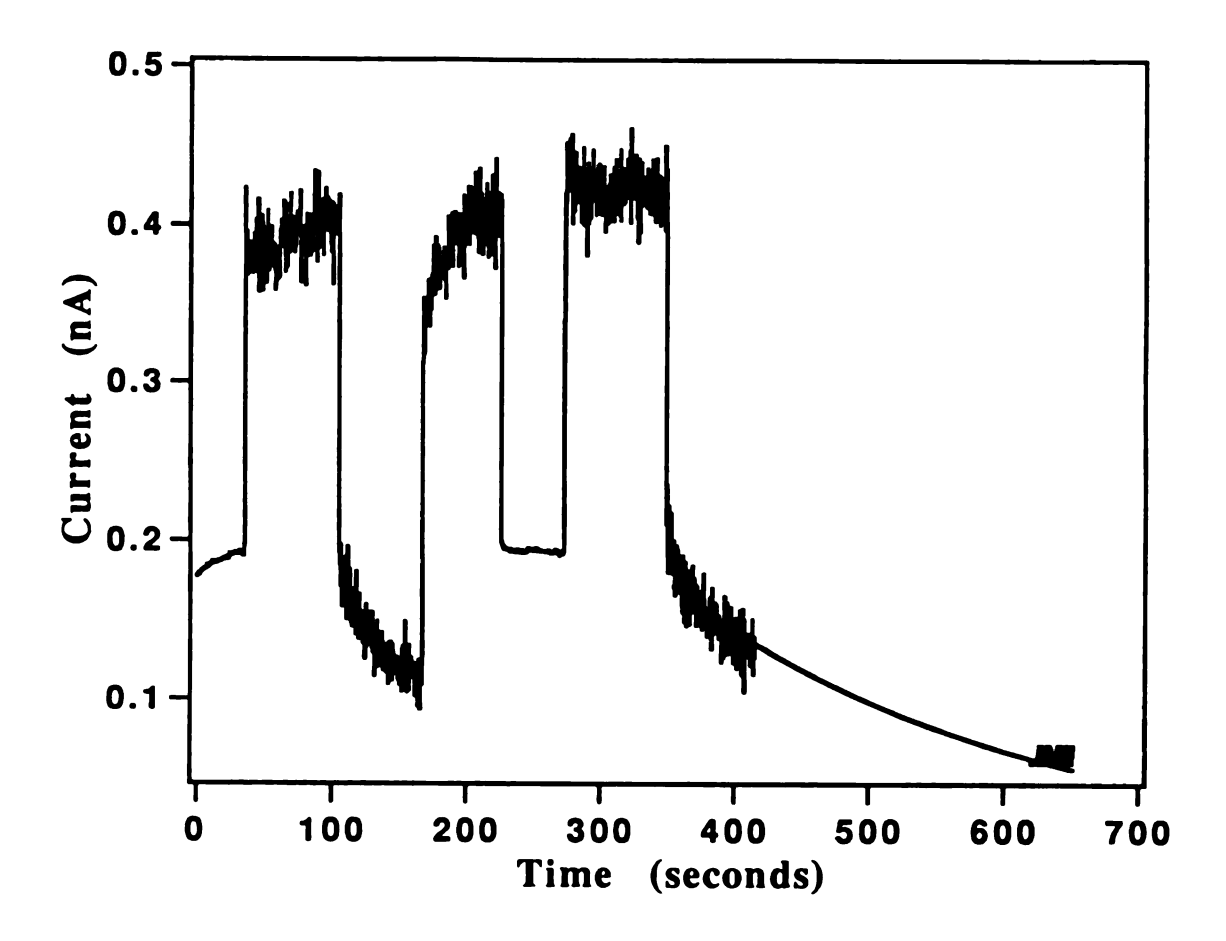


Figure 3-12. The effect of 1063 nm weak laser pulses (10 Hz) on the photoelectron emission current of Na⁺C222·Na⁻ at -60 °C during and after illumination with 400 nm xenon light. The successive vertical lines represent the effects of: 1) IR + 400 nm on; 2) 400 nm light off (note the slow decay of the signal with only IR illumination); 3) 400 nm light on again (note the growth to a plateau level); 4) IR laser light interrupted (note the constant signal representing saturation of trap occupancy); 5) IR laser light on again (note that saturation has already been achieved); 6) 400 nm light off (note the exponential slow decay towards zero signal with only the IR laser on). The solid line shows the fit of the final decay by a simple exponential having the value zero at infinite time.

III.D. Conclusions

The existence of defect sites in crystalline Na+C222·Na-depends on the procedure used for sample preparation. For a pure, nearly perfect crystal there is a low density of defect states in the energy gap. The photoemission spectrum of a collection of such "good" crystals shows a high energy emission peak at 290 nm and very low emission on the low energy side above 400 nm. For a polycrystalline sample, which contains more grain boundaries, defect sites and defect electrons, the photoemission spectrum shows, in addition to the high energy peak at 290 nm, a shoulder at 360 nm and a broad emission band in the range 500 - 700 nm. The low energy emission is presumed to be from trapped electrons.

Laser pluses are able to modify the surface of the sample, and can deplete trapped electrons that lie within 2.33 eV of the vacuum level. They can also populate trapping sites within 2.33 eV of the ground state with laser-excited excess electrons. When the wavelength of the xenon light is longer than 500 nm, the photons have lower energies than the photoemission threshold energy of the valence band, and a recovery growth in photoemission is observed. By contrast, at 400 nm only decay of the laser "shot-peak" occurred. Two kinetic models are suggested to explain the results based on competition between trap-filling and thermal decay. The refilling of empty traps by the photo-excited electrons is probably through the p-band at 600 nm, and through the conduction band or a higher energy band at 400 nm.

The nature of the trapped electrons, such as in what environments they reside or what type of defects are present is still unclear. The stabilization of the trapped electrons may be similar to that of trapped electrons in frozen ices. It is not possible to accurately calculate the density of trapped electrons from this experiment, but other studies suggest that the concentrations are less than a few percent of the Na- concentration.

CHAPTER IV

REFLECTANCE STUDIES OF SODIUM CRYPTAND [2.2.2] SODIDE

IV.A. Introduction

Crystals usually exhibit a wide range of light absorbance when the frequency is varied. In the spectral region of strong resonances, the crystal can be opaque even for the thinnest obtainable sample. Therefore, transmission measurements become impossible and utilization of reflectance spectroscopy is called for. For example, the semiconductors Si and GaAs are more suitable for reflectance than transmission measurements. In our case, the films of Na⁺C222·Na⁻ are polycrystalline samples instead of single-crystals, formed either by solvent evaporation of the sodium sodide solution or by co-deposition of Na and cryptand[2.2.2] vapors. Hence, it is impossible to obtain information about orientation-dependent transitional energies from transmission measurements.

The sodide crystal, Na⁺C222·Na⁻, has a closest-packed structure in which cryptated cations form a hexagonal pattern with sodium anions in the pseudo-octahedral holes. The packing follows an A, B, C, A...pattern. The distance of Na⁻ to Na⁻ is 8.83 Å in the packing plane perpendicular to the C axis, and 11 Å from Na⁻ to the nearest Na⁻ in an adjacent plane [1]. As a result, Na⁺C222·Na⁻ has prominent anisotropy of its physical properties. As is true of all alkalides, this sodide is an air- and temperature- sensitive compound.

So, for any optical study, the crystalline sample has to be under vacuum and at low temperatures.

The reflectance spectrum of Na+C222·Na- has been measured previously [19]. However, analysis of the reflectance data was done by combining the reflectivity and absorption data instead of by a Kramers-Kronig conversion. Also, this analysis could not provide information about the anisotropic properties of the sodide, because the polycrystalline films used for absorbance studies contained crystals with various orientations. In order to obtain further insights into the orientation-dependence of the excited p-states of the sodium anion, we applied the Kramers-Kronig method to analyze the reflectance results for single crystals.

Near-normal incidence reflectivity was measured, with a reflective microscope. Non-polarized and polarized light was used for the measurements. For the polarization-dependent measurements, the electric field vector of the light was aligned both perpendicular and parallel to the c-axis in the energy range 0.5 to 3.1 eV at \approx -60 °C. The optical constants were deduced from a Kramers-Kronig analysis of the reflectivity data. The calculated results are compared with those from the absorption spectra of thin polycrystalline vapor-deposited films of Na⁺C222·Na⁻.

The principles of Kramers-Kronig analyses, the theory of optical dispersion relations and the procedures used to make approximations are included in this introductory section.

IV.A1. The Kramers-Kronig Relations

The Kramers-Kronig (KK) relations are central to the analysis of optical experiments [87,88]. They are a pair of relations,

$$\alpha''(\omega) = -\frac{2\omega}{\pi} P \int_0^\infty \frac{\alpha'(\omega')}{\omega'^2 - \omega^2} d\omega'$$

$$\alpha'(\omega') = \frac{2}{\pi} P \int_0^\infty \frac{\omega \alpha''(\omega)}{\omega^2 - \omega'^2} d\omega$$
(4-1)

These equations enable us to find the imaginary part in a linear passive system from the real part of the response function if the frequency range is large enough, and vice versa. For example, we can relate the real and imaginary dielectric functions or refractive indices by the KK relations.

The origin of the KK relations is the Cauchy integral form and the Cauchy principle value contour [89]. In the Cauchy integral, a function f(z) is analytic when it is in the interior region, within a closed contour bounded by C. The integration is

$$\oint_C \frac{f(z)}{z - z_0} dz = 2\pi i f(z_0). \tag{4-2}$$

If z_0 is in the exterior region, the integral is zero.

The Cauchy principle value contour is shown in Fig. 4-1, where z_0 is exterior to the contour but unlimitedly close to the real X axis. The integration of the closed contour $\oint_C \frac{f(z)}{z-z_0} dz$ is zero.

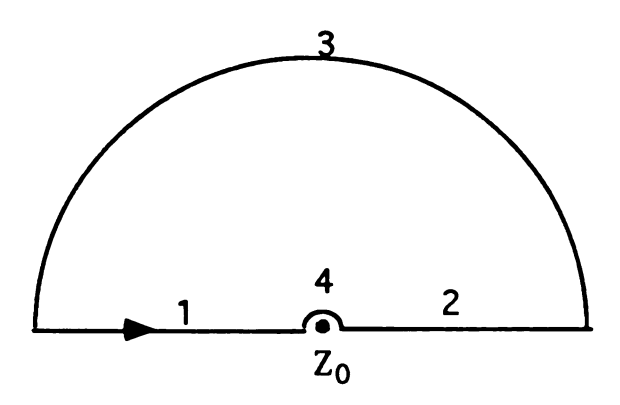


Figure 4-1. Contour for the Cauchy Principle Value integral.

The integrations of segments 1 and 2 can be derived

$$\int_{(1)} + \int_{(2)} = i\pi f(z_0) = P \int_{-\infty}^{\infty} \frac{f(x)}{x - z_0} dx, \qquad (4-3)$$

where f(x) is a complex function. Equation 4-3 is the origin of the Kramers-Kronig relations, which can be split into the real and imaginary parts of KK dispersion relations (as these in Equation 4-1), provide the following conditions can be met [90],

- (1) The poles of f(x) are all below the real axis X.
- (2) The integration of f(x)/x in the upper half semi-circle vanishes (a sufficient condition is $f(x) \to 0$ uniformly as $|x| \to \infty$).
- (3) The real part of f(x) is an even function and the imaginary part is odd.

The reflectivity $\gamma(\omega)$ is a complex function defined as the ratio of the incident electric field E to the reflected electric field. The reflectance R, defined as the intensity ratio,

$$R = \left(\frac{E(ref)}{E(inc)}\right)^{\bullet} \cdot \left(\frac{E(ref)}{E(inc)}\right),\tag{4-4}$$

is a real quantity, and has is a physically measurable value. The reflectance can also be expressed and related to the reflectivity, $\gamma(\omega)$ by

$$\gamma(\omega) = R^{\frac{1}{2}}(\omega)e^{i\theta(\omega)} \tag{4-5}$$

where $\theta(\omega)$ is the phase difference (or phase-shift) between the incident and reflected waves. It is difficult to measure the phase shift directly in reflectance, but the phase shift can be calculated when the reflectance is obtainable. Theoretically, if we know the reflectance at *all* frequencies we are able calculate the phase-shift angle through the Kramers-Kronig relations,

$$\theta(\omega) = -\frac{2\omega}{\pi} P \int_0^\infty \frac{\ln R^2(\omega')}{\omega'^2 - \omega^2} d\omega'$$
 (4-6)

where P is the Cauchy principle value, which indicates the process of integration that a voids the poles at ω . It is difficult to carry out the direct integration in Equation 4-6 due to the unknown values at very high and very low frequencies. In order to proceed with numerical integration, Equation 4-6 can be converted by partial-integration to the form

$$\theta(\omega) = -\frac{1}{2\pi} \int_0^{\infty} \ln \left| \frac{\omega' + \omega}{\omega' - \omega} \right| \frac{d \ln R(\omega')}{d\omega'} d\omega'$$
 (4-7)

This integration form permits some approximations that make the empirical numerical analysis appropriate. When the reflectance $R(\omega')$ becomes a constant in the very low and very high frequency regions, these regions do not make contributions to the integration because the derivative $\frac{d \ln R(\omega')}{d\omega'}$ is zero; and when ω' is much greater or much less than ω , the contribution of $\ln \left| \frac{(\omega' + \omega)}{(\omega' - \omega)} \right|$ becomes very small. These properties allow us to avoid the difficulties of obtaining experimental data at the extremes of frequency. The reflectance data at very high and very low frequencies are usually inaccessible by optical measurements. However, with sufficiently accurate extrapolations from the available experimental data, the KK calculations will not yield large deviations from the true spectra [91,92].

IV.A2. The Optical Dispersion Theory

For the optical study of a solid material, it is important to understand the interaction of photons with the material. Experimentally, the photon probe should have a larger wavelength (λ) than the dimensions of a unit cell, the roughness of the surface of the material should be much less than the wavelength of the light used, and only the bulk properties are considered to contribute.

The optical properties of a solid can be described in term of the macroscopic properties such as the refractive index n and the

extinction coefficient k. With Maxwell's equations, these optical constants can be further derived to yield relations to other functions such as the dielectric constants (ϵ ' and ϵ "), the optical conductivity (σ ' and σ ") and the energy loss function.

The optical constants are complex functions and any solid medium can be described by the complex refractive index, N(E) = n(E) - ik(E), or the complex dielectric function, $\varepsilon(E) = \varepsilon_1(E) - i\varepsilon_2(E)$. Since all the optical constants can be derived from n(E) and k(E), and they are functions of the photon energy, these equations are called the optical dispersion relations.

When an electric field is applied to solids, it will cause the opposite displacements of positive and negative charge entities. The polarization is defined as the dipole moment per unit volume, and is expressed as the integral form

$$P = V_{p}^{-1} \sum_{i} n_{i} q_{i} u_{i}. \tag{4-8}$$

The integration is over one primitive cell, where V_p is the unit cell volume, and q is the charge, μ is the displacement and n is the number of electrons in the unit cell. The dipole moment u can be expressed as a power series of E, $u \propto \alpha E + \beta E^2 + \gamma E^3 + \cdots$. When a normal electric field is applied (< 10^4 eV/cm), only the linear term needs to be considered. Polarization then becomes proportional to the electric field, $P = \chi$ E, where χ is electric susceptibility.

Reflectivity arises from oscillating valence electrons out of phase with the incident radiation. In the process no absorption of the induced polarization current occurs, and interference of the incident wave with the reradiated waves from the valence electrons leads to reflectivity. When a very low frequency electric field is applied, the polarization is completely adjusted to the applied field, so χ is a real number. However, as the frequency increases some of the displacements of heavier effective mass that contribute to P will not be able to follow the frequency. The part of the polarization that is out of phase by $\pi/2$ is the imaginary part. Therefore, P is strictly defined as $P = (\chi_1 + i\chi_2)$ E. This equation relates the magnitude and phase relations between two physically observable quantities, P and E.

The classical theory of the dispersion relations is mainly due to the Lorentz and Drude models. The Lorentz model is applicable to insulators and semiconductors, which assumes that all the interband transitions are direct (k conservative). The Drude treatment is applicable to free electron models, in which the interband transitions include all the transitions not involving a reciprocal lattice. From the Lorentz oscillator, the dielectric functions for nonmagnetic materials can be derived as

$$\varepsilon_{1} = 1 + \frac{4\pi Ne^{2}}{m} \frac{\left(\omega_{0}^{2} - \omega^{2}\right)}{\left(\omega_{0}^{2} - \omega^{2}\right)^{2} + \Gamma^{2}\omega^{2}}$$

$$\varepsilon_{2} = \frac{4\pi Ne^{2}}{m} \frac{\Gamma\omega}{\left(\omega_{0}^{2} - \omega^{2}\right)^{2} + \Gamma^{2}\omega^{2}}$$
(4-9)

in which ω_0 is the inherent harmonic frequency of the bound electrons, and Γ is a viscous damping coefficient. When Equations 4-9 are applied to classical atoms with more than one electron per atom, the N, ω and Γ terms need only be replaced by N_i , ω_i and Γ_i ,

respectively, and the equations are changed to summation forms. Equations 4-9 indicate that the real dielectric function is qualitatively dependent upon the band gap, and $\hbar\omega_0$ is verified as corresponding approximately to the band gap, where ε_1 decreases with the increase of $\hbar\omega_0$ [93].

Table 4-1 Important physical parameters and equations for a medium.

Parameters	Equations
$oldsymbol{arepsilon}_1, oldsymbol{\chi}_1$	$\varepsilon_1 = 1 + 4\pi \chi_1$
$arepsilon_{2,}\chi_{2}$	$\varepsilon_2 = 4\pi\chi_2$
$\sigma_{_1}, \chi_{_2}, arepsilon_{_2}$	$\sigma_1 = \omega \chi_2 = \omega \varepsilon_2 / 4\pi$
$\sigma_{\scriptscriptstyle 2}, \chi_{\scriptscriptstyle 1}, arepsilon_{\scriptscriptstyle 1}$	$\sigma_2 = -\omega \chi_1 = -\omega(\varepsilon_1 - 1)/4\pi$
$oldsymbol{arepsilon}_1, n, k$	$\varepsilon_1 = n^2 - k^2$
ε_2, n, k	$\varepsilon_2 = 2nk$
$n, \mathcal{E}_1, \mathcal{E}_2$	$n^2 = \left(\frac{1}{2}\right)\left[\varepsilon_1 + \left(\varepsilon_1^2 + \varepsilon_2^2\right)^{\frac{1}{2}}\right]$
$k, \varepsilon_1, \varepsilon_2$	$k^{2} = \left(\frac{1}{2}\right)\left[-\varepsilon_{1} + \left(\varepsilon_{1}^{2} + \varepsilon_{2}^{2}\right)^{\frac{1}{2}}\right]$

The physically unobservable parameters χ , ε and σ are defined in complex forms, and are co-related to each other, such that, once

one parameter is known the others can be obtained also. They define the essential optical characteristics of a solid. In Table 4-1, the equations for the parameters and their relations to the optical constants n and k are listed [94].

IV.A3. <u>Procedure and Approximations for Kramers-Kronig</u> <u>Applications</u>

Theoretically, calculating the exact θ requires the reflectance spectrum at all the frequencies. Empirically, this is impossible due to the difficulties of obtaining data at very high and very low frequencies. However, reasonably accurate calculations can be made if an appropriate extrapolation of R is applied beyond the range of measurement.

The extrapolation to zero frequency is easy; there are two ways to approach the goal. First, if the low-frequency dielectric constant is measured [95], the equations $\varepsilon_1 = n^2 - k^2$ and $R = \frac{(n-1)^2 + k^2}{(n+1)^2 + k^2}$ can be used to calculate the reflectance R at very low frequency, since the absorption coefficient k of the electron transition is zero at very low frequency. It should be pointed out that absorption bands from vibrations at low frequency do not contribute to the electronic transitions, and can be ignored. Second, for certain crystals, an accurate index of refraction n at very low frequency can be obtained from prism measurements [96, 97], so that R can be obtained.

The extrapolation of R beyond the data range to higher energies does not follow a simple rule, but there are conventions. Providing that the frequency region does not contain strong bands

caused by electronic transitions, the reflectance remains high until the plasma frequency, then falls rapidly at higher energy. The plasma frequency for semiconductors can sometimes be roughly estimated by using the free-electron plasma equation $\omega_p = (4\pi ne^2/m)^{1/2}$, by substituting the number of valence electrons per atom as free electrons into the equation. So, at high energy the value of R can be deduced from the asymptotic expression for the dielectric constant [98],

$$R(\omega) = c\omega^{-4},\tag{4-11}$$

at much higher energies, n and k can be assumed to be ≈ 1 and 0, respectively.

A more quantitative description of the extrapolation of R can be evaluated by comparing the known absorption coefficients of a bulk transmission to the calculated ones at energies near the band gap.

Original reflectance data are usually affected by noise, therefore the spectrum does not show a completely smooth curve. If direct differentiation of the data is carried out for numerical integration of Equation 4-7, the calculated results would lead to scattered values. A technique to circumvent this difficulty is to smooth the data by using the Savitzky-Golay method. The Savitzky-Golay smoothing is a least-squares procedure that allows the spectra to have their original shapes after the operation.

IV.B. Experimental

The sodide crystals were grown by programmed slow cooling, 2 °C per hour, of a solution of Na+C222·Na- in a mixture of solvents from -10 °C to -60 °C, in which the ratio of the solvents methylamine/trimethylamine was about 3:1. Crystals of dimensions up to several mm on an edge were formed, and some of these crystals were selected and vacuum-sealed in a quartz optical cell that was attached to the crystal-growing apparatus. They were stored in a -80 °C freezer and kept at a low temperature during the reflectance measurements. By never opening the cell after crystal growth, very shiny single crystals could be studied.

The reflectivity spectrometer had an Ealing-Beck microscope body with a 15X/ 28 reflecting objective (Figure 4-2). The light source was a 150-W tungsten-halogen lamp with the light directed by a 90° mirror via objective mirrors to the sample. Between the light source and the semi-transparent mirror a linear polarizer was installed with its polarization direction perpendicular to the reflective plane. The light hit the sample at near-normal incidence (= 6°), and the light spot was about 40 µm in diameter. The reflected light was transmitted to and through an optical fiber to the optical analyzer (Guided Wave model 206), which had resolutions of 6 nm from 400 nm to 1200 nm and 8 nm from 1200 to 2400 nm. A Si detector was used for the former optical range and a PbS detector was employed for the latter. Each of the reflectivity data points was accumulated 15 times to enhance the signal-to-noise ratio. The reflectivity of Na⁺C222·Cl⁻ was used to calibrate that of the Na+C222·Na-

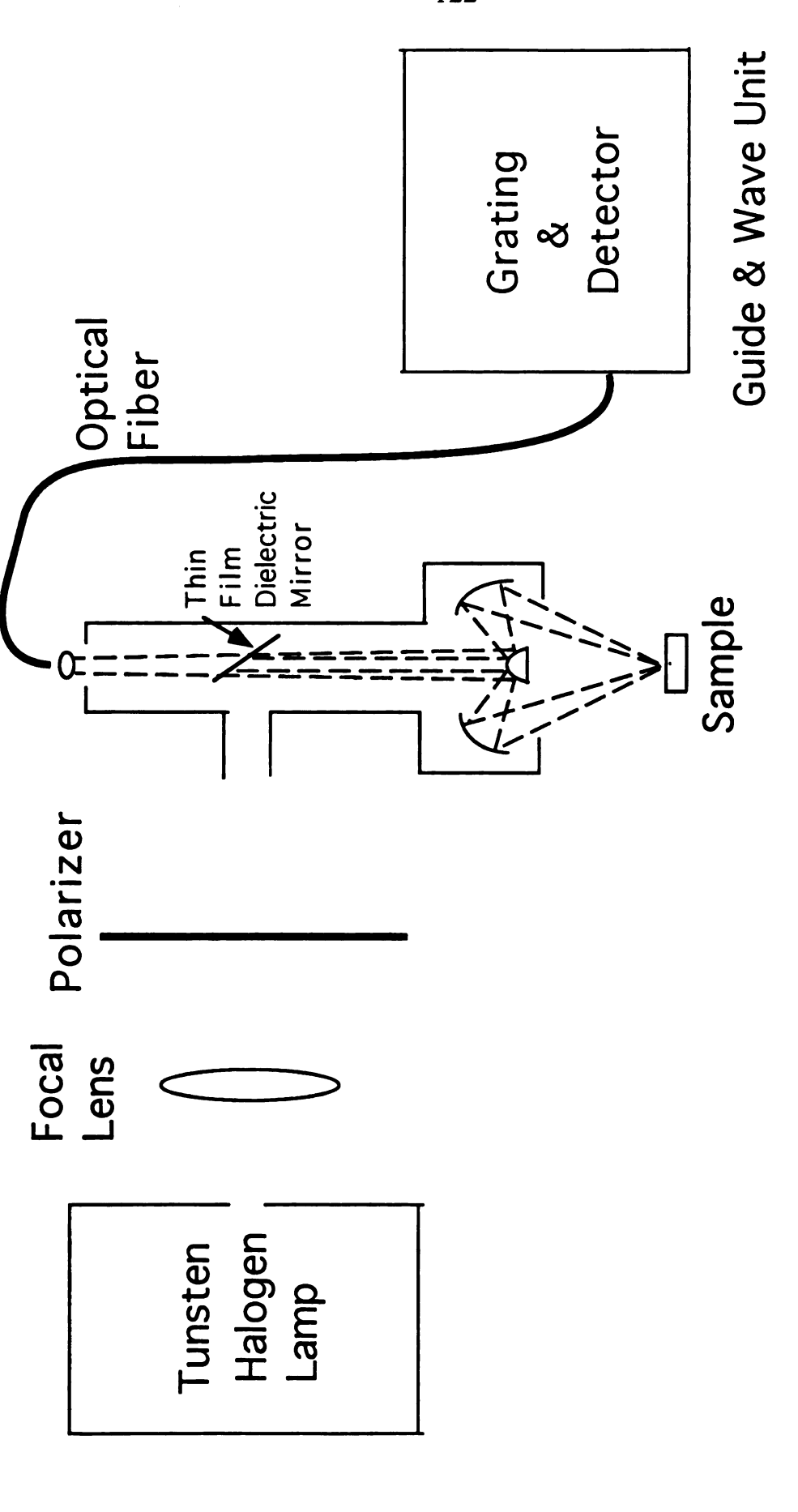


Fig. 4-2. Schematic diagram of the reflective microscope system.

In order to obtain the optical constants, we performed Kramers-Kronig analyses. In the far infrared, the reflectance was extrapolated to zero frequency by calculating R from the low frequency dielectric constant, presuming the absorptivity to be zero at zero frequency. At high energy, the reflectance was extrapolated with the asymptotic expression $R(\omega) = c\omega^{-4}$. The complete reflectance data set was first smoothed by the Savitzky-Golay method, then was subjected to a Spline fit to expand the data from about 150 to 2048 points. (The data expansions were used to reduce the errors in the derivatives required for the calculations.) After the phase shifts, $\theta(\omega)$, were calculated, the other orientation-dependent optical constants were then obtained by using the equations shown in Table 4-2.

As shown in the Appendix, three programs were written in the FORTRAN language for the numerical integration. In the integration, a key step is that in each integration to generate a data point, a corresponding pole has to be avoided.

The program KKFAB02.FOR is for numerical integration of Equation 4-7. The input data has to be a text array, and in the form of three columns with the number of rows less than 2200. The contents in the columns are $R(\omega)$, $\Delta \ln R(\omega)$ and E, in order. The output is in the same form as the input, in that the data of the columns are $R(\omega)$, $\omega(\theta)$ and E, in order. The output data are in the text form, and can be loaded into Lotus 1-2-3, and the optical constants can be calculated by using the equations listed in Table 4-2.

Table 4-2. Equations for calculation of the optical constants.*

Kramers-Kronig conversion	$\theta(\omega) = \frac{-2\omega}{\pi} P \int_0^\infty \frac{\ln R^{\frac{1}{2}}(\omega')}{{\omega'}^2 - \omega^2}$
Extinction coefficient	$k = \frac{2R^{\frac{1}{2}}\sin\theta}{1 + R - 2R^{\frac{1}{2}}\cos\theta}$
Refractive Index	$n = \frac{1 - R}{1 + R - 2R^{\frac{1}{2}}\cos\theta}$
Real part of the dielectric function	$\varepsilon' = n^2 - k^2$
Imaginary part of the dielectric function	$\varepsilon^{}=2nk$
Energy loss function	$-\operatorname{Im}\left(\frac{1}{\varepsilon}\right) = \frac{2nk}{(n^2 + k^2)^2}$

^{*}The applications to anisotropy are restricted.

Equation 4-7 can be further partially integrated to another integration form [99]

$$\theta(\omega) = \frac{1}{2\pi} \int_0^{\infty} \left[(\omega - \omega) \ln \left| \omega - \omega \right| + (\omega + \omega) \ln \left| \omega + \omega \right| \right] d\left(\frac{d \ln R(\omega)}{d\omega} \right). \tag{4-12}$$

The program FORKRON.FOR is for numerical integration of Equation 4-12. The input and output forms are the same as those of the program KKFAB02.FOR, except that the contents of columns are $R(\omega)$, $\Delta \ln R(\omega)$, E and P_k , in order, where P_k is $\left[\Delta \ln R(\omega_{k+1}) - \Delta \ln R(\omega_k)\right]$. The results calculated from this program are nearly identical to those calculated from the program KKFAB02.FOR. No advantage in the numerical integration is observed by using Equation 4-12 instead of Equation 4-7, but it provides a mean for comparison.

From Equation 4-1, a reflectance spectrum can be converted to an absorption spectrum, and vice versa. However, the extrapolation procedures for an absorption spectrum are different from those of reflectance. On the low frequency side, the absorption can be extrapolated to zero if one can assure that no electronic transitions occur below a specific frequency. On the higher energy side, the absorption can be assumed to be approaching a very low value, and k approaches zero at very high frequency. The program KKRFAB02.FOR is for converting the absorption spectrum to reflectance. The contents of the input columns are the absorption A, $\Delta k(\omega)$ and E, in order, in which k is the extinction coefficient. The outputs are k, n-1 and E. Note that the integration of Equation 4-13 yields n-1 instead of n [100],

$$n(\omega) - 1 = \frac{2}{\pi} P \int_0^{\infty} \frac{\omega' k(\omega')}{(\omega')^2 - \omega^2} d\omega'. \tag{4-13}$$

IV.C. Results and Discussion

Fig. 4-3 is a reflectance spectrum of a single crystal of Na+C222·Na- in the range from 0.5 to 3.1 eV (400 - 2400 nm). The peak reflectance is at ~ 2.1 eV (~ 600 nm) and a small shoulder occurs at ~ 1.65 eV (~ 680 nm). The small shoulder does not always show up on a given plane of the crystal, and its intensity varies with a change in the light spot position. We suggest that the shoulder maybe correspond to an indirect electronic transition of Na-, as indicated by the strong temperature dependence. The position of the shoulder shifts to a lower energy when the temperature is increased, and vice versa. (Figure 4-4) An alternative explanation is that the shoulder results from defect electrons that are trapped at Na-vacancies.

As shown in Figure 4-5, the shapes of reflectance spectra do not change appreciably by rotating the surface plane. This indicates that the reflectance spectra are true signals despite the fact that the surface is not exactly perpendicular to the beam path. The reflective light cone carries real information about the material.

Due to the hexagonal structure of Na⁺C222·Na⁻, anisotropic properties are expected. However, these properties cannot be observed in thin film samples because the films are composed of polycrystals with various orientations. Single crystal reflectance measurement with polarized light sources would provide abundant

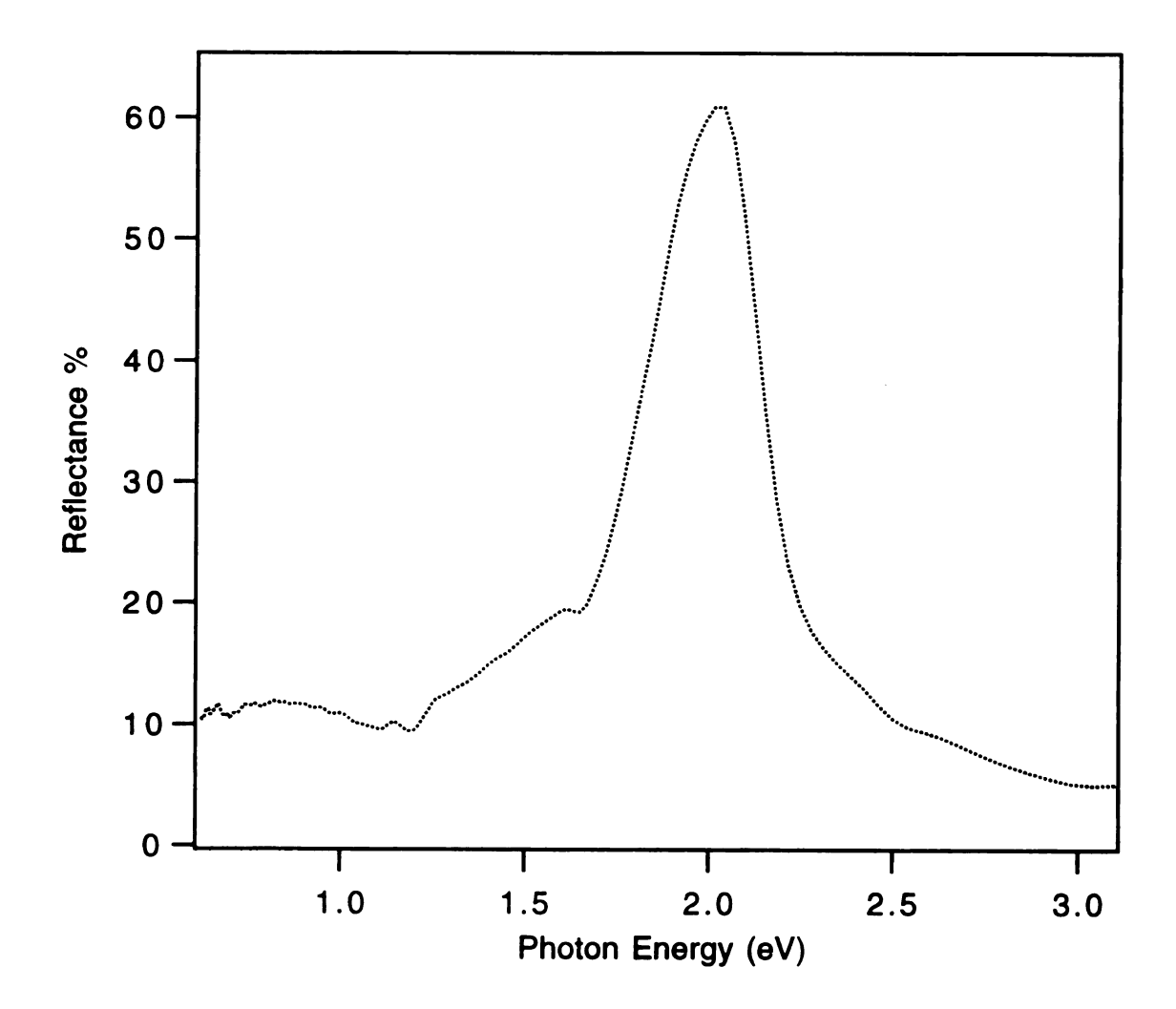


Figure 4-3. Reflectance spectra of a single-crystal of Na⁺C222·Na⁻ at ≈ -60 °C. Non-polarized light was used for this measurement.

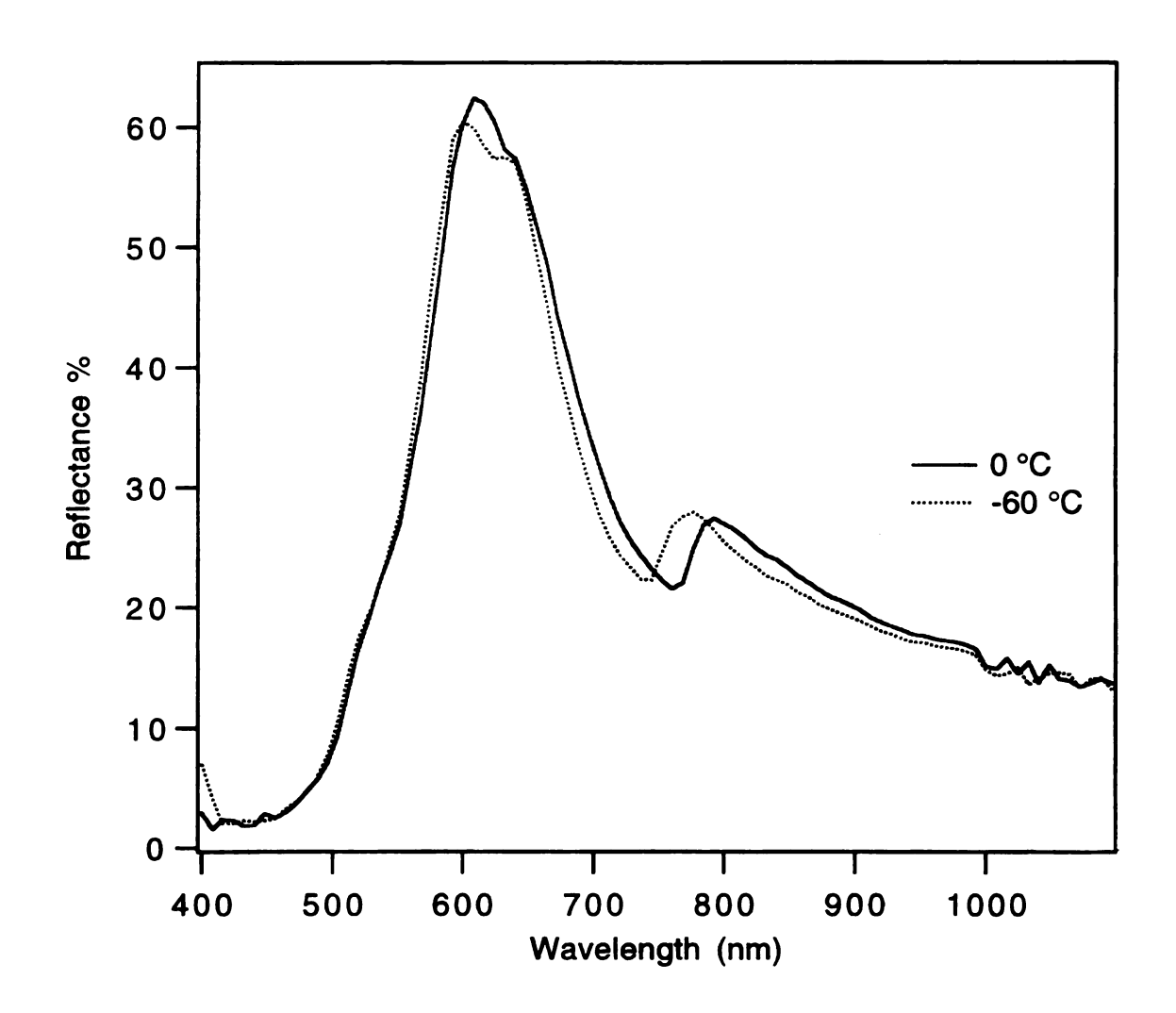


Figure 4-4. Temperature-dependent reflectance spectra of Na+C222·Na⁻. The shoulder at \approx 780 nm shifts from 775 nm to 795 nm when the temperature is increased from - 60 °C to 0 °C. Polarized light was used for this measurement with \vec{E} // C.

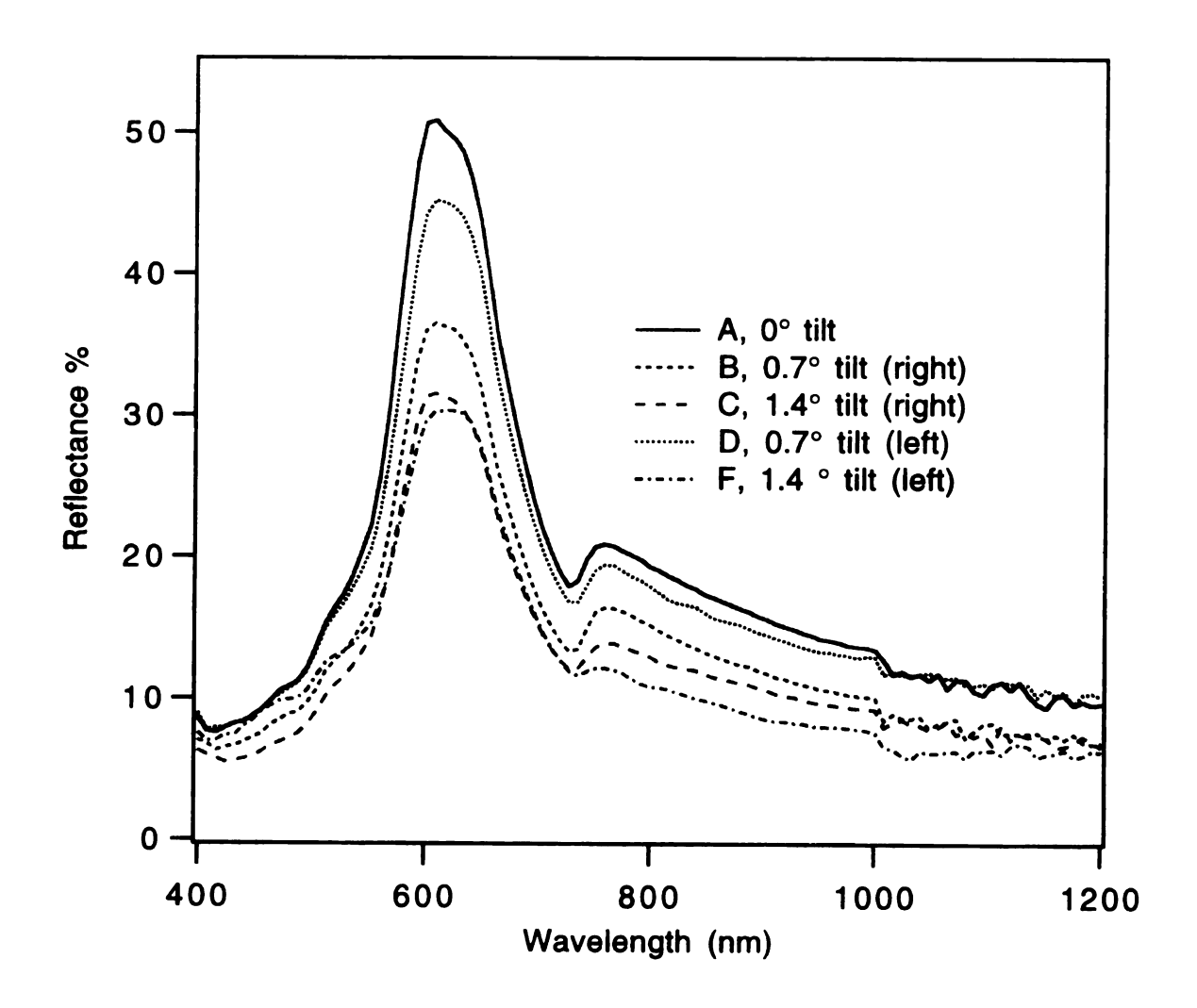


Figure 4-5. Reflectance spectra of single-crystal Na⁺C222·Na⁻ at ≈ - 60 °C with various small tilt angles of the surface plane. Non-polarized light was used for this measurement.

information to help in understanding the anisotropic properties that are related to the differences of the optical dispersion constants along the a- and b- axes from those along the c-axis.

Typical polarization dependent near-normal incidence reflectivity spectra at ≈ -60 °C of single crystal Na+C222·Na- in the energy range 0.5 - 3.1 eV are shown in Figure 4-6. The spectrum A has 4 major features at energies of 1.6, 1.95, 2.05 and 3.1 eV. In addition, there is a shoulder at 2.4 eV. Spectrum B has 3 major features at energies of 2.05, 2.5 and 3.1 eV and 3 very minor shoulders at the energies 1.6, 1.9 and 2.3 eV. There is seemingly a one-to-one correspondence in the peak positions. For example, the peaks at 1.6 and 1.95 eV for spectrum A correspond to the shoulders at 1.6 and 1.9 eV for spectra B. However, the peak at 2.5 eV in spectrum B does not have its counterpart in spectrum A.

The reflectivity spectra shown in Figure 4-6 were measured from different faces of the single crystal. A number of such measurements were made with the electric field \vec{E} of the polarized light along various directions in the faces. The reflectivity spectra were related to the structure by examining the characteristic shapes of the single crystals. For example, spectrum A corresponds to $\vec{E}/\!\!/C$, and spectrum B is for $\vec{E}\perp\!/C$.

The optical constants shown in Figures 4-8 to 4-13, which are more relevant to the electronic states under discussion than the reflectivity spectra, were deduced by means of Kramers-Kronig analyses of the reflectivity spectra. In Figure 4-9, the absorption spectra are obtained from the extinction coefficient k (Figure 4-8) and show that the main peak position is at 1.91 eV. One low energy

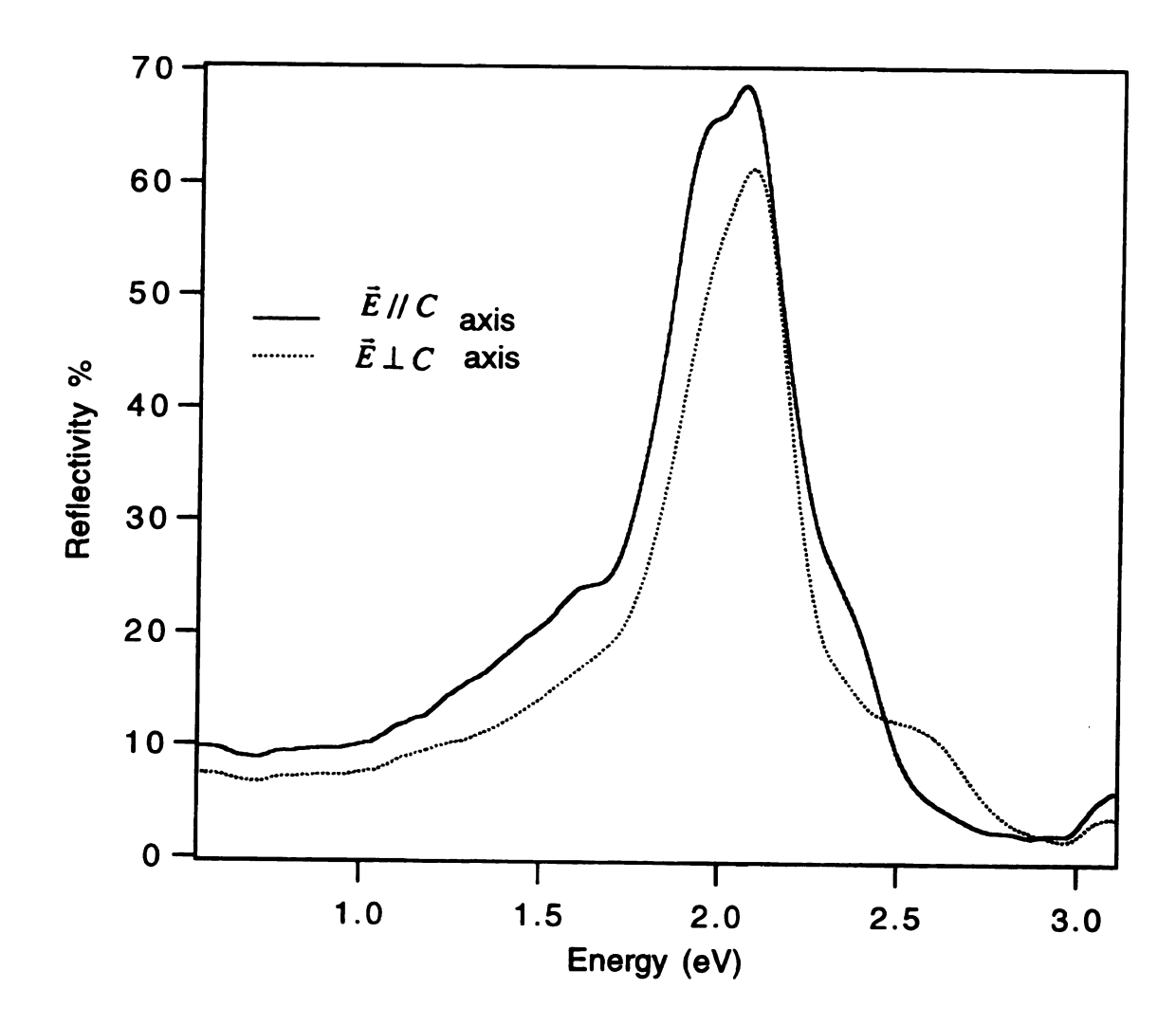


Figure 4-6. Near-normal incidence reflectivity of single-crystal Na⁺C222·Na⁻ for $\vec{E} /\!\!/ C$ and $\vec{E} \perp C$ at \approx - 60 °C.

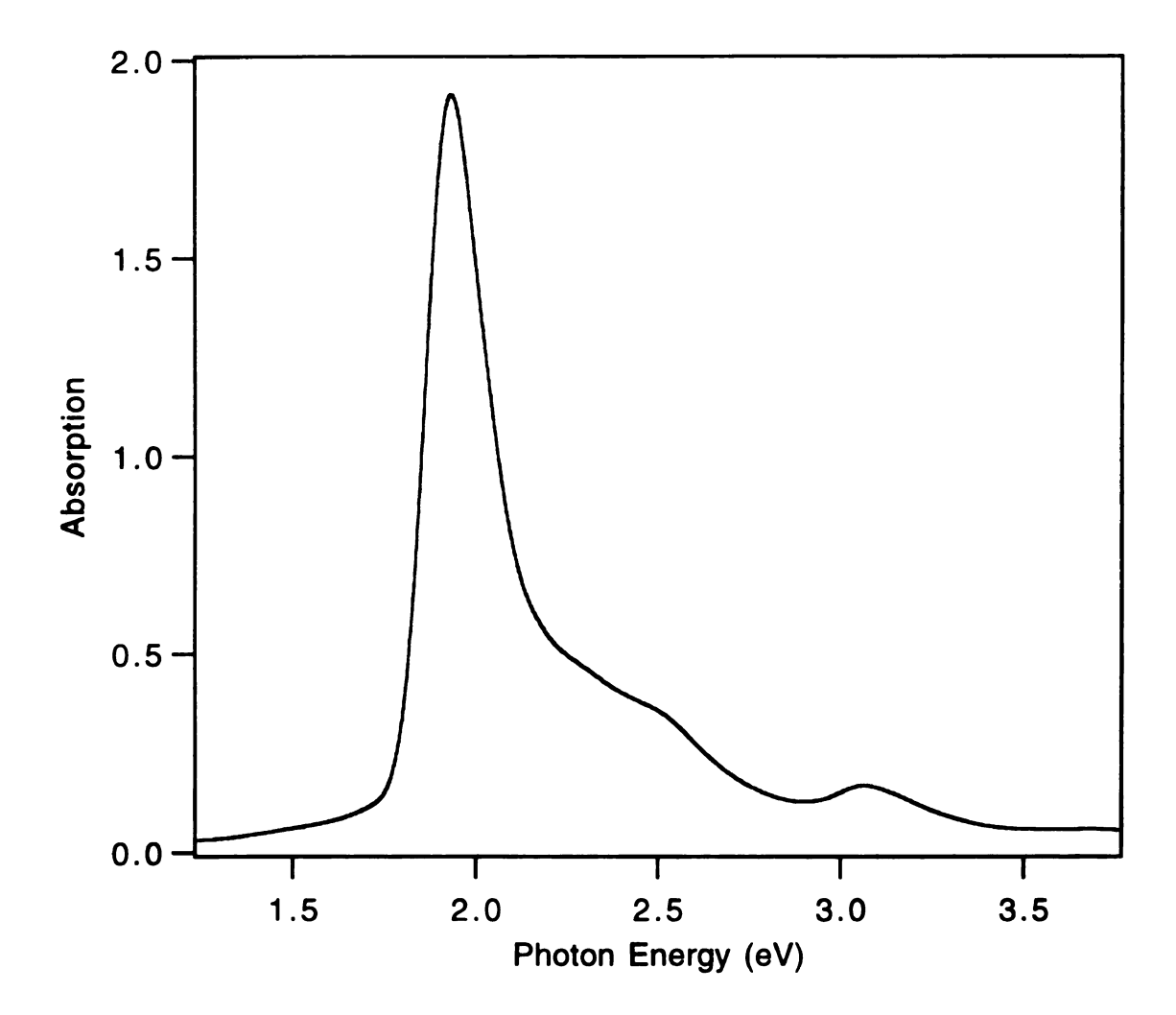


Figure 4-7. Absorption spectra of a polycrystalline thin film of Na+C222·Na⁻ with a thickness of 930 Å at ≈ - 60 °C. (Data of J. E. Hendrickson [86])

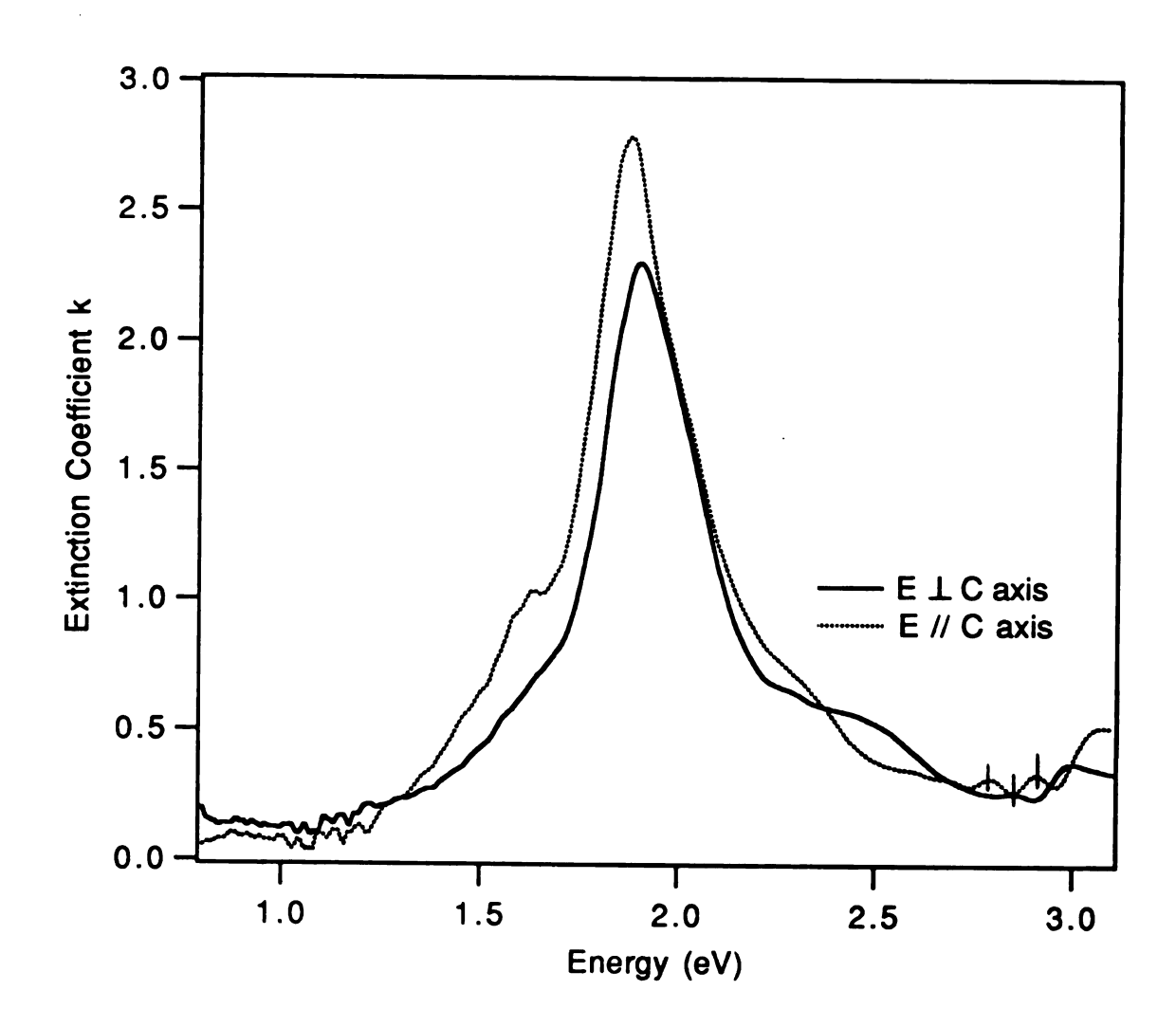


Figure 4-8. Spectral dependence of the derived extinction coefficient k of single-crystal Na⁺C222·Na⁻ for $\vec{E}//C$ and $\vec{E} \perp C$ at \approx - 60 °C. The peaks with tick marks are not real, but are due to noise on the weak signal.

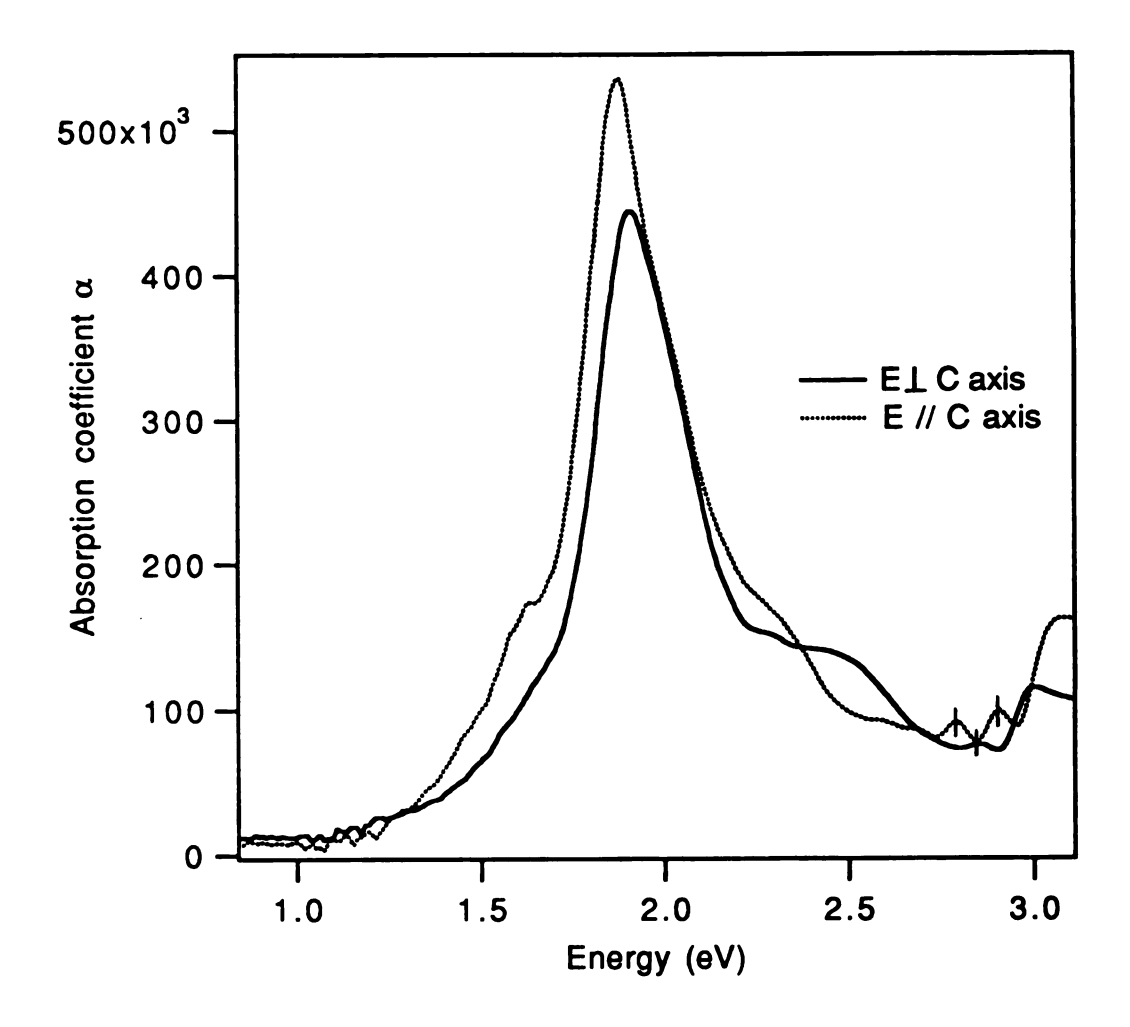


Figure 4-9. Absorption coefficient of single-crystal Na⁺C222·Na⁻ for $\bar{E}/\!\!/C$ and $\bar{E}\perp C$ at \approx -60 °C. On the high energy side of the main peak, the spectrum shows an apparent shoulder at \approx 2.35 eV for $\bar{E}/\!\!/C$ and a peak at 2.5 eV for $\bar{E}\perp C$. The peaks with tick marks are not real, but are due to noise on the weak signal.

peak at 1.65 eV only shows up for $\bar{E}/\!\!/C$. The shoulder at 2.35 eV for $\bar{E}/\!\!/C$ corresponds to a very small peak for $\bar{E}\perp\!\!/C$ whereas the peak that appears at 2.5 eV for $\bar{E}\perp\!\!/C$ is absent for $\bar{E}/\!\!/C$. These results are compared with the absorption spectrum of thin vapor-deposited films (Figure 4-7), together with other measurements such as fluorescence [17], conductivity[18] and photoemission. We identified the peak at \approx 1.91 eV as due to the transition from $3s^2 \rightarrow 3s^2$, the shoulder at 2.35 or peak at 2.5 eV is the transition from $3s^2 \rightarrow$ conduction band, and the 1.65 eV peak is presumed to be the absorption peak of trapped defect electrons on the surface.

The refractive index spectrum (Figure 4-10), n, as a function of photon energy is less affected than the extinction spectra, k, on the low energy side, by either the accumulated errors or extrapolation inaccuracy. Therefore, such spectra can be accurate even at low energies. The refractive index values 1.85 and 1.7 for E//C and $E\perp C$, respectively, at low frequencies, are presumed to be accurate. Comparing the main peak of the spectra in k with that in n, shows that the peak in k occurs at higher energies than that in n, which is consistent with the theory of interband transitions. Integration of the extinction coefficient k from very low frequency to very high frequency yields the oscillator strength, f, which is defined as $4.33 \times 10^{-9} C^{-1} \int k(\overline{\nu}) d\overline{\nu}$, in which C is the concentration of the absorbing species in mole per liter [19].

Figure 4-11 gives the real part of the optical dielectric function of Na⁺C222·Na⁻. The plasma energy, ω_p , is estimated to be about 2.5 eV, where the value of ε_1 is zero. The real part of the dielectric function is qualitatively dependent on the band gap. The optical

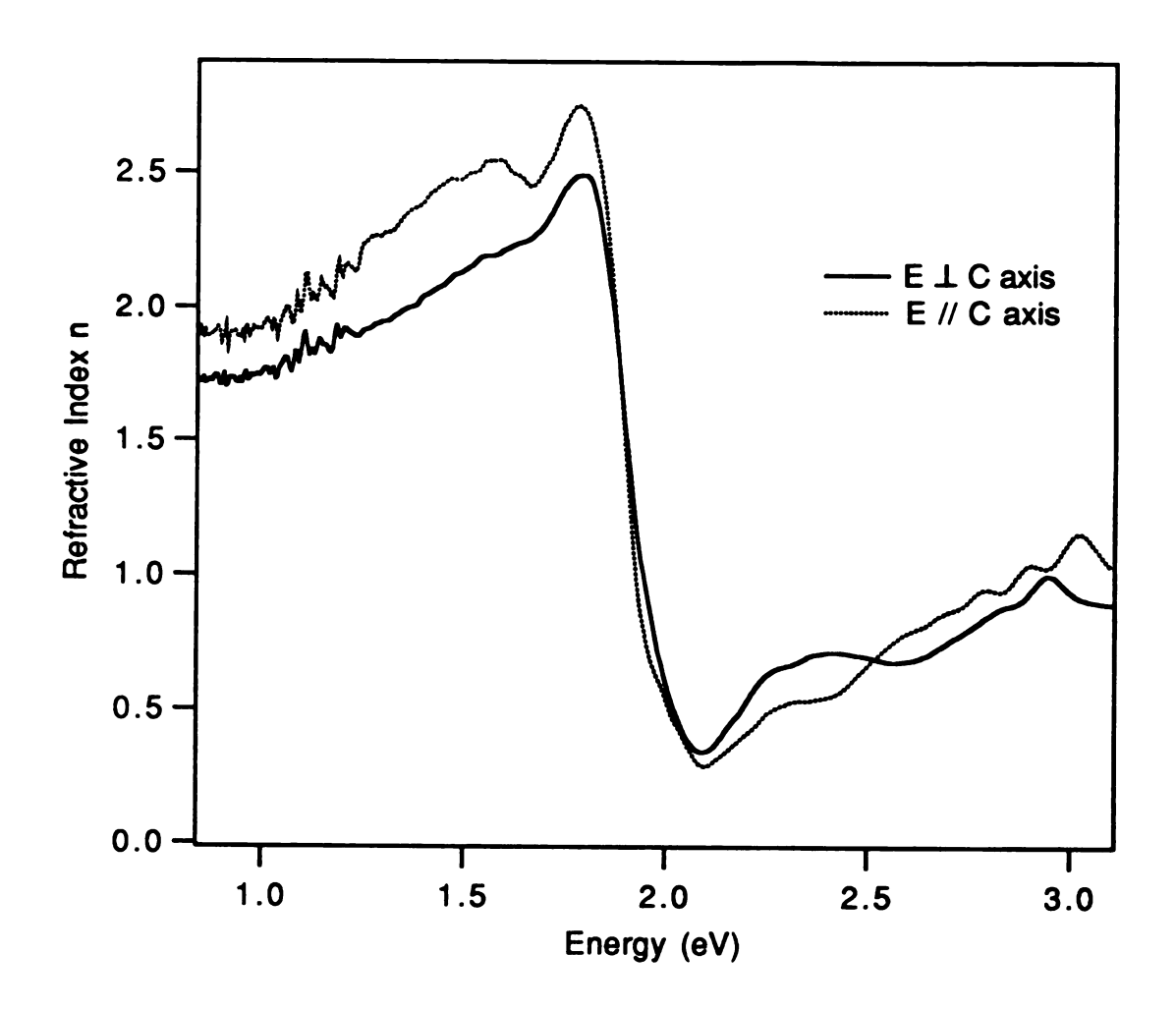


Figure 4-10. Spectral dependence of the real part of the refractive index n of single-crystal Na⁺C222·Na⁻ for $\vec{E} /\!\!/ C$ and $\vec{E} \perp C$ at \approx - 60 °C.

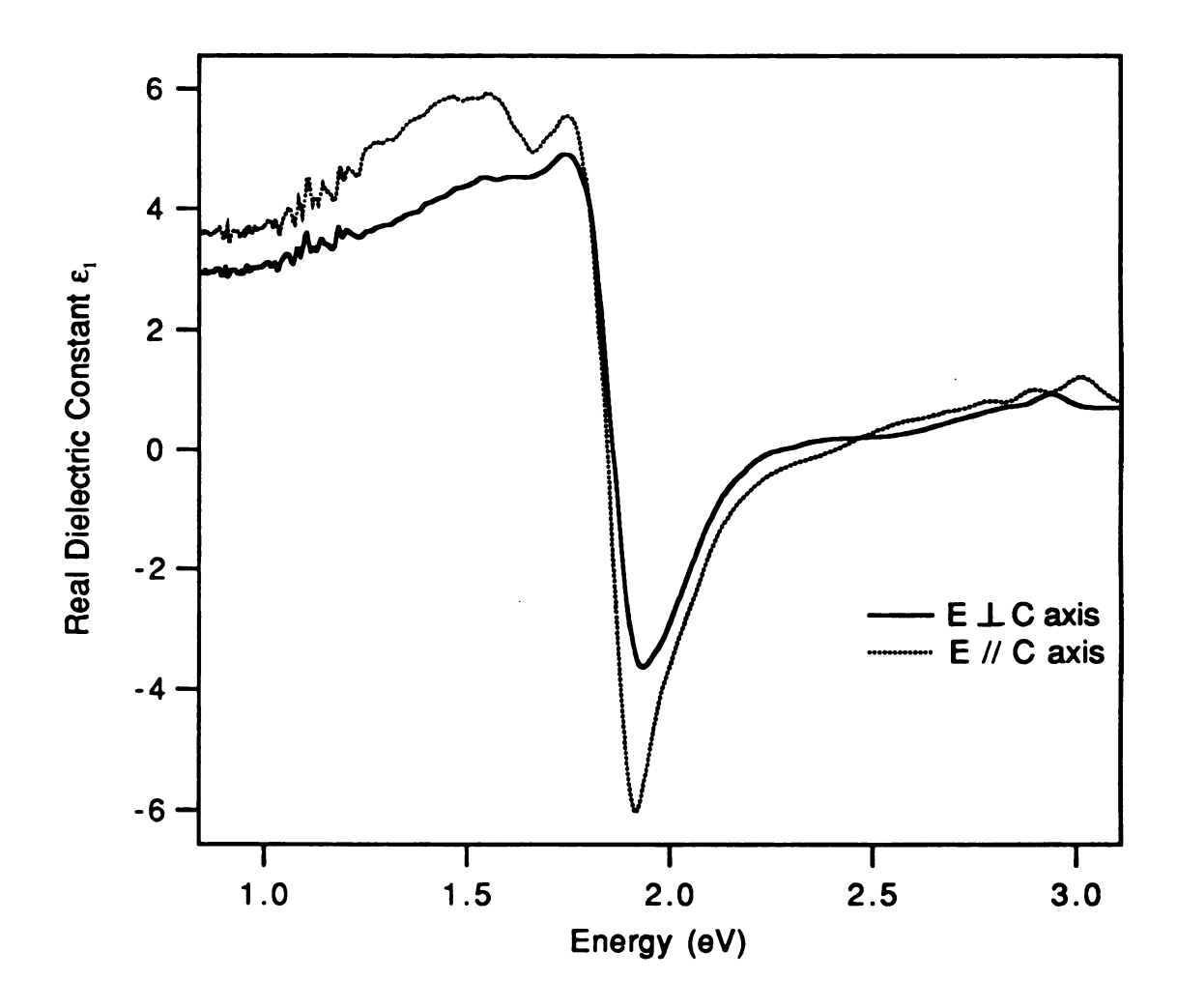


Figure 4-11. Spectral dependence of the real part of the dielectric function ε_1 of single-crystal Na⁺C222·Na⁻ for $\bar{E}/\!\!/C$ and $\bar{E} \perp C$ at \approx -60 °C.

dielectric functions at low frequency are 3.5 for $\bar{E}/\!\!/C$ and 3.0 for $\bar{E}\perp\!\!/C$. As a result, we suggest that the band gap for $\bar{E}\perp\!\!/C$ is larger than that for $\bar{E}/\!\!/C$ [9]. In Figure 4-9, the absorption peak at 2.5 eV for $\bar{E}\perp\!\!/C$ and shoulder at 2.35 eV for $\bar{E}/\!\!/C$ would be related to the gap energies.

The imaginary part of the dielectric function is the most meaningful to compare with theory since this quantity is directly related to the experimentally measured interband absorption strength, at least in the region where the intraband contribution is small. Theoretically, $\omega^2 \varepsilon_2(\omega)$ is proportional to the absorption strengths, and the peaks in ε_2 correspond directly to the positions of interband transitions. The ε_2 spectra are shown in Figure 4-12. Structures are apparent at 1.65 eV; 1.9 eV (main peak); and 2.35 eV for $\vec{E}/\!\!/\!\!/\!\!/\!\!/\!\!/\!\!/$ and at 1.9 eV (main peak); and 2.5 eV for $\vec{E}\perp\!\!/\!\!/\!\!/\!\!/\!\!/$ These results confirm that the Na⁺C222·Na⁻ has anisotropic optical properties.

The function $-\text{Im}\,\varepsilon^{-1}$ describes the energy loss of fast electrons traversing the material and is called the energy loss function. In figure 4-13, the maximum is at ≈ 2.5 eV for $\vec{E} \perp C$ and ≈ 2.6 eV for $\vec{E} \mid C$. The latter has a broad-band shape rather than a sharp peak with a maximum at ≈ 2.6 eV. A sharp peak of this function is frequently is associated with the existence of plasma oscillations, so the determined plasma frequency at ≈ 2.5 eV (see Figure 4-11) is close to this value. However, the high-energy trend of the spectra indicates that another peak may exist on the high energy side.

Figure 4-14 is the extinction coefficient spectrum calculated from the reflectance spectrum measured with non-polarized light,

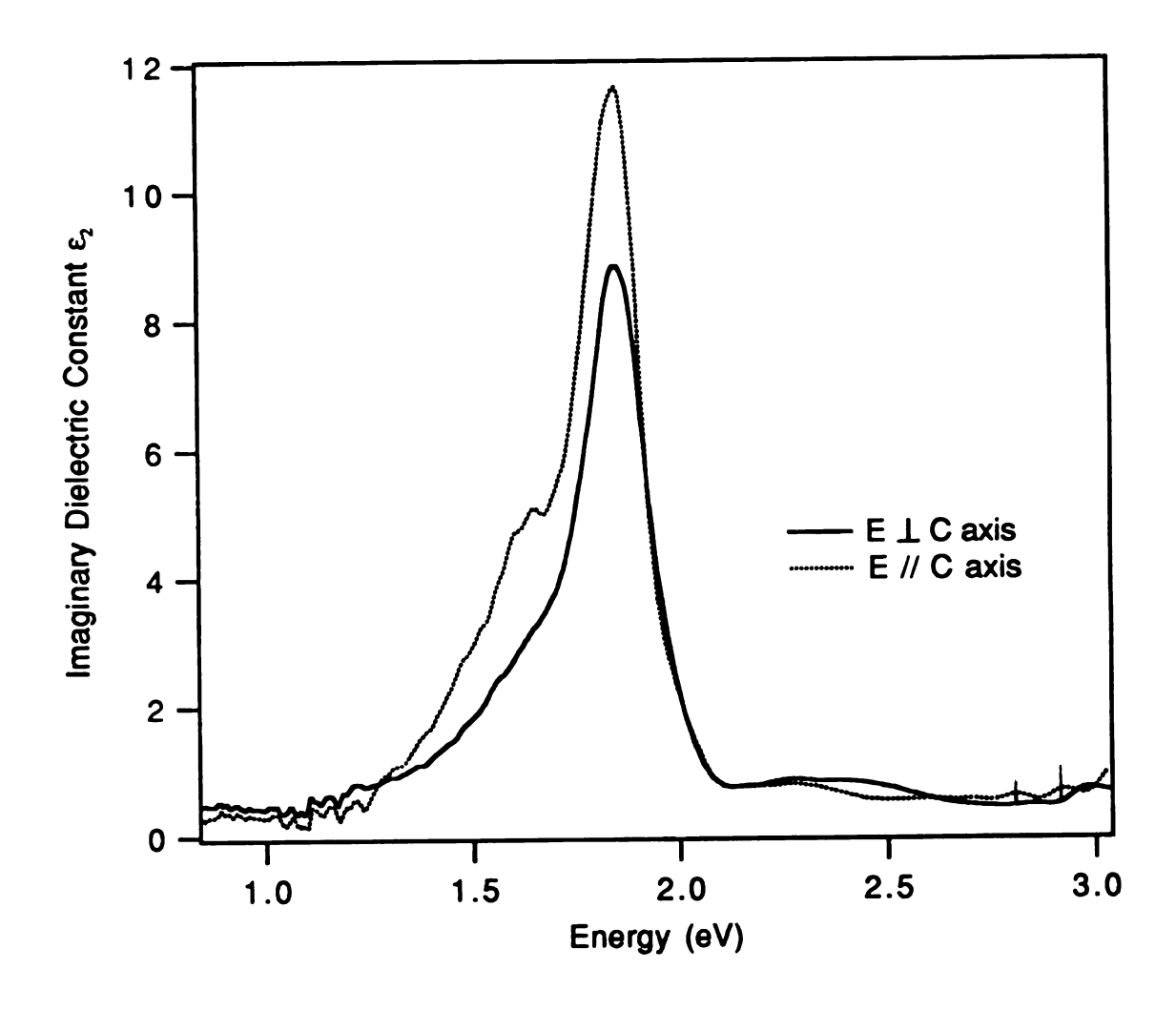


Figure 4-12. Spectral dependence of the imaginary part of the dielectric function ε_2 of single-crystal Na⁺C222·Na⁻ for $\vec{E}/\!\!/C$ and $\vec{E} \perp C$ at \approx -60 °C. The peaks with tick marks are not real, but are due to the low signal-to-noise ratio.

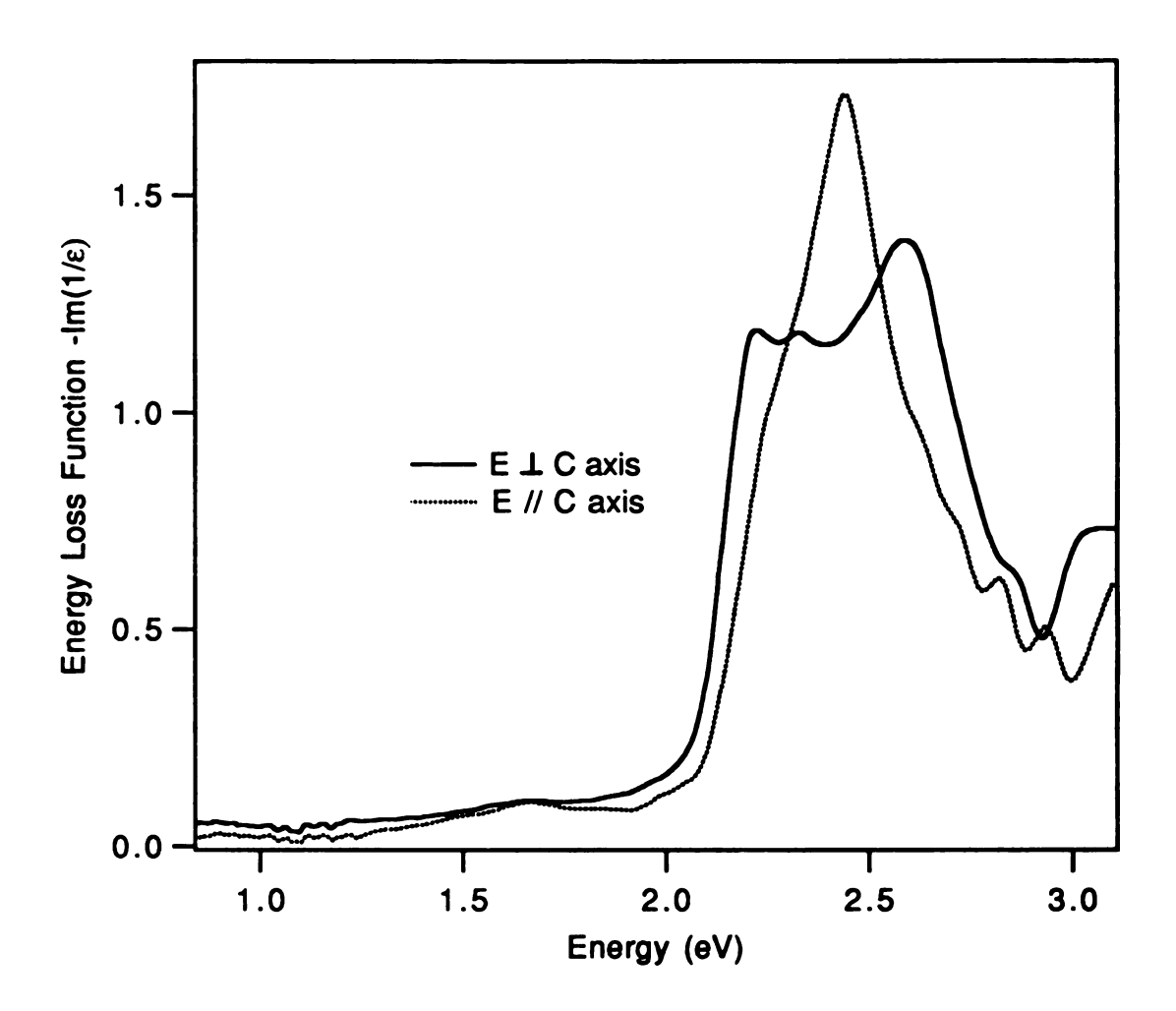


Figure 4-13. Spectral dependence of the energy loss function, $-\text{Im}(\varepsilon^{-1})$, of single-crystal Na⁺C222·Na⁻ for $\vec{E}/\!\!/ C$ and $\vec{E} \perp C$ at ≈ -60 °C.

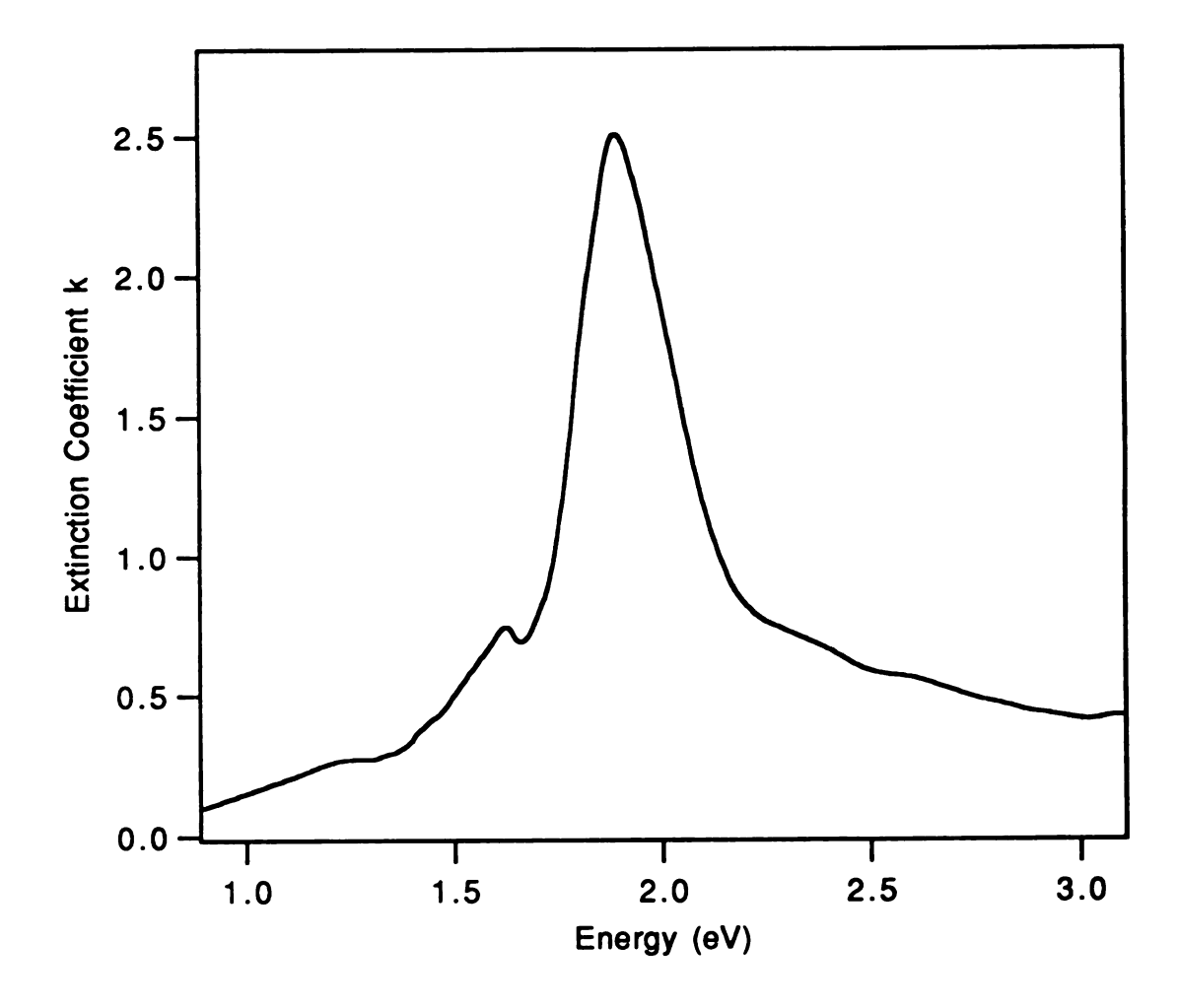


Figure 4-14. Spectral dependence of extinction coefficient k of single-crystal $Na^+C222 \cdot Na^-$ at ≈ -60 °C. Non-polarized light was used for this measurement. The small shoulder at 1.65 eV is presumed to result from trapped electrons.

which is essentially a combination of the electronic transitions in all possible orientations. The spectrum shows some differences from the results of polarization, especially weaker features on the shoulders. However, an average of combining the extinction coefficients for E/C and $E\perp C$ yields the spectrum shown in Figure 4-15, which is very similar to Figure 4-14. This result provides additional evidence for the anisotropic properties of Na+C222·Na-, and these properties can only be observed by polarization methods.

This polarization method provides useful information about the orientation-dependent properties. For the sake of comparison, these results are listed in Table 4-3.

The absorption spectrum of Figure 4-7 can be converted into the reflectance spectrum with Equation 4-13. The result is shown in Figure 4-16, which is likely to have better resolution than the measured reflectance spectra.

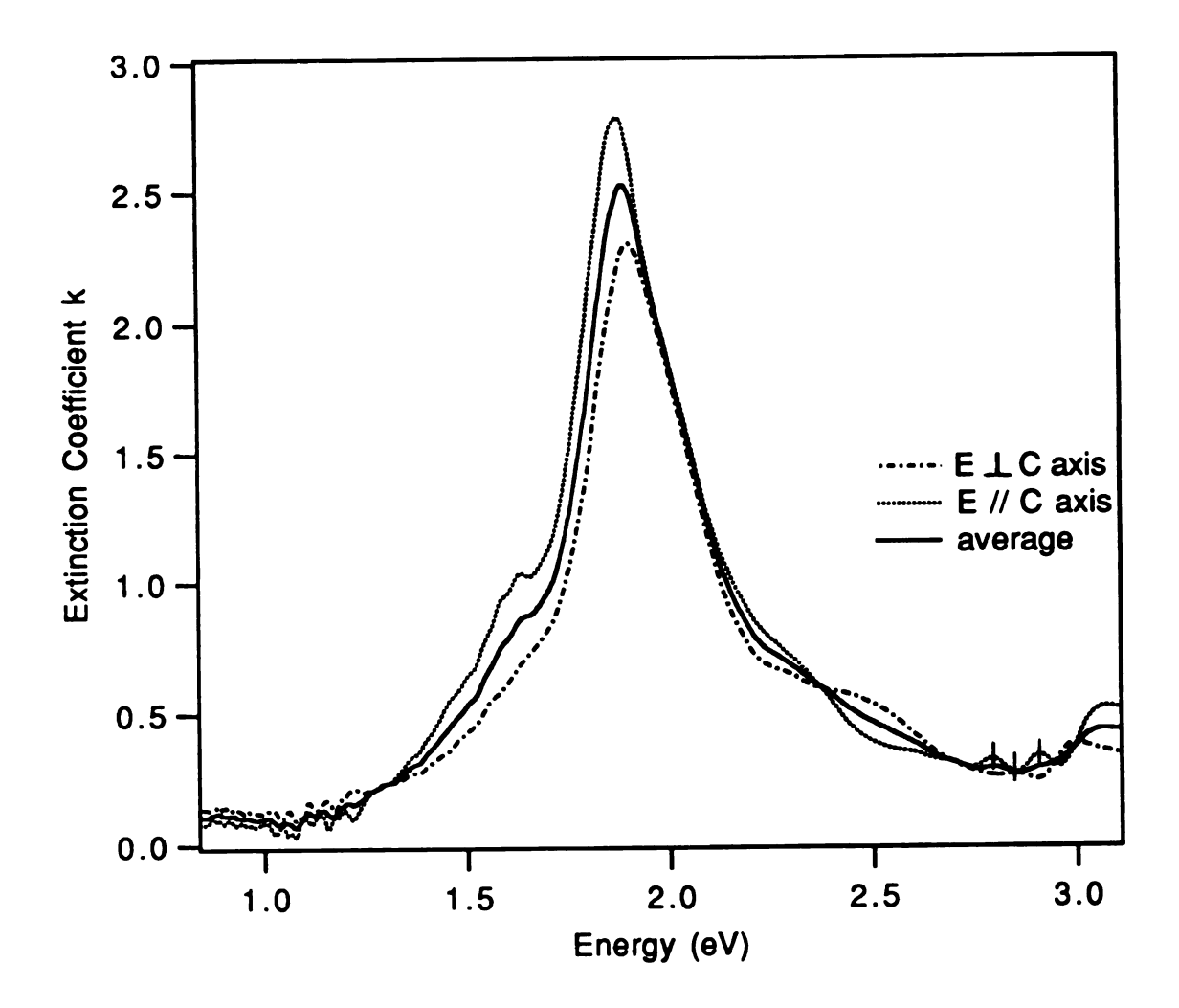


Figure 4-15. The spectral dependence of the extinction coefficient of single-crystal Na⁺C222·Na⁻ at \approx - 60 °C. The solid line is the average of the extinction coefficient for $\vec{E}/\!\!/ C$ and $\vec{E} \perp C$, and can be used to compare with the extinction coefficient from non-polarized light.

Table 4-3. Polarized and non-polarized studies of Na+C222·Na-.*

	$\vec{E}/\!/C$	$\vec{E}\bot C$	non-polarized
R peaks position(eV)	1.6, 1.95, 2.05 3.1	2.05, 2.5, 3.1	1.6, 2.0, <u>2.6</u>
R shoulders (eV)	2.4	1.6, 1.9, 2.3	2.3
k peaks (eV)	1.91, 1.65	1.93, <u>2.3,</u> 2.5	1.6, 1.92, <u>2.55</u>
k shoulders (eV)	2.35	none	2.35
n (at low energy)	1.8	1.6	1.85
n (at 0 frequency)	1.76	1.72	1.64
ε_1 (at low frequency)	3.5	3.0	3.6
ε_1 (at 0 frequency)	3.1	3.0	2.6
ε_2 peaks (eV)	1.65, 1.9, 2.35	1.9, 2.5	1.6, 1.9, 2.3, 2.6
-Im(1/ ^E) peaks (eV)	≈ 2.6	≈ 2.5	≈ 2.5

^{*} The data with under line are weak peaks.

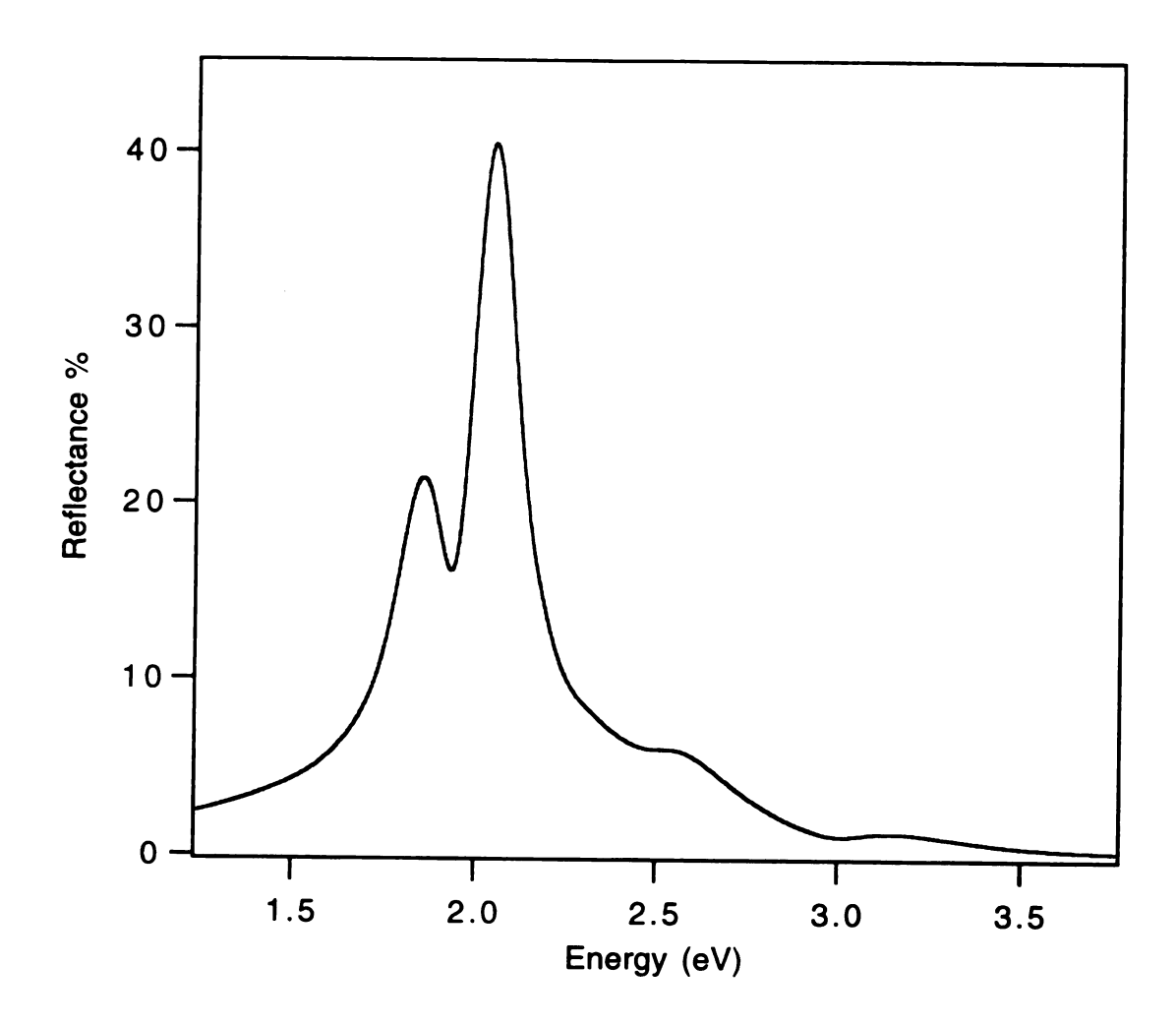


Figure 4-16. The reflectance spectrum obtained from Kramers-Kronig conversion of the absorption spectrum in Figure 4-7.

IV.D. Conclusions

From Kramers-Kronig conversions, the orientation-dependent optical constants have been obtained. The transitional energies from the ground state to the p-state are 1.91 eV for $\vec{E}/\!\!/C$ and 1.93 eV for $\vec{E}\perp\!\!/C$. The gap energy difference is even apparent, 2.35 eV for $\vec{E}/\!\!/C$ and 2.5 eV for $\vec{E}\perp\!\!/C$. Comparison between Figure 4-7 and Figure 4-8, shows that the absorption spectrum is closer to that for $\vec{E}\perp\!\!/C$. This indicates that probably most of the polycrystals in the Na+C222·Na-film are with the c-axis face-up; that is, the planes in which the Naions are close together are parallel to the surface of the sapphire substrate.

CHAPTER V

CONCLUSIONS AND SUGGESTIONS FOR FURTHER WORK

V.A. Conclusions

A photoemission system has been built that has the advantage of loading a sample with minimum contact with gases or moisture. The system has 3 vacuum chambers: loading, film-preparation and photoemission measurement chambers. Such a design permits one to perform sequential experimental procedures in different chambers according to the functions of the chambers. The purpose is to keep the main chamber clean and under good vacuum. The photoemission measurements can be performed in the range from room temperature to -130 °C, and the temperature is controlled with the accuracy of ± 2 °C. A data acquisition system has been built which includes a home-built interface for the monochromator and an IEEE-488 interface for the electrometer. The programs for data acquisition were written in the GW-Basic language which are able to control the output voltage of electrometer and the scanning speed of monochromator, and to record data with respect to wavelength or The combination of the photon source and the data acquisition system could be widely used for optical studies, not just limited to What would have to be done is to modify the photoemission. programs.

The photoemission of alkalides, K⁺(15C5)₂·K⁻, Rb⁺(15C5)₂·Rb⁻, Na⁺C222·Na⁻, K⁺C222·K⁻, Cs⁺C222·Cs⁻ and K⁺C222·Na⁻ were measured.

The photoemission threshold energies were determined according to the theory developed by O. Kane [44]. The spectra can be divided into three categories. A good crystalline sample with few defect states in the band gap has a spectrum that shows only a high energy emission peak of the valence electrons of M- and very low emission on the low energy side. If a polycrystalline sample contains a number of defect states, and defect electrons the spectrum shows, in addition to the high energy peak, an emission band and shoulder on the low energy side. The spectra of partially decomposed samples show only very weak emission on the high energy side.

Although the photoemission of electrides, K⁺(15C5)_{2·e⁻}, K⁺C222·e⁻ and Cs⁺(18C6)_{2·e⁻}, could be measured, the emissions seem not to be from the true electrides. The samples are inferred to be partially decomposed during the film-preparation.

Laser pulses had appreciable effects on $Na+C222 \cdot Na^-$ samples. The polycrystalline samples contain both defect sites and defect electrons. As a result, the laser pulses can both deplete and replenish the trap sites. The surface of the sample may also be modified due to the presence of lattice defects. The laser pulses deplete trapped electrons within 532 nm below the vacuum level and also populate trapping sites within 532 nm above the ground state. As a result, there is an enhancement of the trapped electron concentration (n_i) within 400 nm of the vacuum level but a decrease of n_i within 600 nm of the vacuum level compared to the steady state value. The recovery of the bleaching effect upon illumination at 600 nm is shown to be a photon assisted process instead of a thermal equilibrium process. The recovery rate constant decreases

with an increase in temperature, but the decay rate with 400 nm xenon light seems not to be temperature-dependent. Two model are suggested to describe the recovery effects. One is that photo-excited electrons proceed via a cascading relaxation to refill the empty trap sites; another model suggests that refilling the empty trap sites by photo-excited electrons is through the p-band. The second model is preferred because the first one does not explain the temperature-dependent recovery rates. To complete the analysis of the growth rate, a slow growth rate obtained with a fresh film was included in the second model.

The reflectance spectra have been successfully converted into absorption spectra, and vice versa. The programs for the Kramers-Kronig conversions have been tested with a set of CdS data taken from a book [99]; the nearly identical results prove that the method used for the numerical integration is correct. The programs can now be routinely used for conversion of spectra. Several successful steps made the reflectance studies possible. First, shiny single-crystals of Na+C222·Na- were able to be grown with a special method. Second, optical fibers and the Guided Wave spectrometer system were able to transfer and process the signal, which makes the measurements more reliable, accurate and efficient. Third, appropriately smoothing the data with the Savitzky-Golay method made the conversion possible even with somewhat noisy data.

The optical constants of Na+C222·Na- have been obtained, which is a help in understanding the optical properties of the sodide. For example, the peaks of the imaginary part of dielectric function correspond to the interband transitions. The polarization-

dependence studies, and then the optical constants obtained, provide important information about the anisotropic properties of Na+C222·Na-.

V.B. Suggestions for Further Works

The photoemission studies of electrides were always hampered by partial decomposition. A possible way to solve this problem would be to measure the PE without redissolving the samples to make films. However, the contact of the sample with the sample holder and the smoothness of the surface are still problems that need to be overcome.

The PE energy distribution curve measurements were obscured by the surface charge. To circumvent this problem, a higher energy photon source is necessary, but it is costly. An alternate way to make the measurements is to use a commercial UPS system such as the one in Dr. Ledford's laboratory. Unfortunately, two problems remains. One is that the instrument is not working yet. Another problem is that there is no cooling system in the instrument, so that any measurement of temperature-sensitive compounds would be very difficult.

The techniques for reflectance studies have been developed. The same methods can be applied to study any alkalides or electrides, but only if a shiny crystal can be grown and enough reflectance data can be obtained in the range from 400 - 2400 nm.

The FTIR reflective microscope is an alternate choice for measurement of reflectance due to the advantage of a broad range of

the light source (700 -5000 nm). However, two requirements have to be fulfilled before the measurements can be made. First, the platform has to have both X- and Y- directions adjustable as well as the Z- direction. Second, an appropriate window for the transmission of light at very low frequencies has to be employed.

Theoretical calculations of the band structure of these compounds would provide very interesting results to compare to the experimental data. This is especially true for Na⁺C222·Na⁻, because various measurements of the energy states have been made.

APPENDIX

MONOVOLT.BAS

10 REM PHOTOEMISSION DATA ACQUISITION SYSTEM.
15 REM 9/29/92, WRITTEN BY C. T. KUO
20 DIM DDAT(2000,3)
30 PRINT

INPUT FILE NAME AND STOPPING WAVELENGTH ************************************
40 INPUT "INPUT FILE NAME FOR DATA";FILE\$ 50 '
60 INPUT "STOP WAVELENGTH?";FINWAV 70 '
80 INPUT "DO YOU WANT AUTOMATIC CORRECTION WAVELENGTH (Y/N)";ANS\$
90 CORR=0
100 '
110 IF ANS\$="Y" THEN CORR=10
120 '

OPEN THE SERIAL PORT RS-232 TO LISTEN AND TALLK, AND
RESERVE A FILE FOR DATA STORAGE.

130 OPEN "COM1:9600,N,8,1,DS,CS,CD,RS" AS #1
140 OPEN FILE\$ FOR APPEND AS #2
150 IF LOF(2)=0 THEN CLOSE #2
160 ELSE PRINT"FILE ALREADY EXISTS":CLOSE #2
170 OPEN FILE\$ FOR OUTPUT AS #2
180 PRINT

INITIALIZE THE IEEE-488 INTERFACE BOARD, SET BIAS VOLTAGE
AND TIME INTERVAL BETWEEN DATA POINTS.

190 INPUT "TIME INTERVAL FOR DATA IN SECONDS";RUNTIME 200 INPUT "VOLTAGE IN VOLTS";PVO 500 'INITIALIZE THE BOARD 510 DEF SEG=&HC000 520 CMD\$="SYSCON MAD=3,CIC=1,NOB=1,BA0=&H300" 530 VAR%=0:FLG%=0:BRD%=0:IE488=0 540 CALL IE488(CMD\$,VAR%,FLG%,BRD%) 550 IN = ASC(INPUT\$(1,#1)) 560 PRINT IN 570 IF IN<>2 THEN GOTO 540 ************************************
SET PARAMETRS FOR THE INTERFACE OF MONOCHROMATOR
CONTROLLER

1000 C\$=CHR\$(3):M\$=CHR\$(4):GO\$=CHR\$(18)
1010 STA\$=CHR\$(80):STB\$=CHR\$(96):STC\$=CHR\$(121)
1020 NHUN\$=CHR\$(160):NDEC\$=CHR\$(144):NUNI\$=CHR\$(128)
1030 FIELD #1,1 AS AO\$
1040 LSET AO\$=GO\$
1050 PUT #1,1
1060 FIELD 1, 1 AS E\$
1070 LSET E\$=STA\$
1080 PUT #1,1
1090 FIELD #1,1 AS ASTB\$
1100 LSET ASTB\$=STB\$
1110 PUT #1,1
1120 FIELD 1,1 AS ASTC\$
1130 LSET ASTC\$=STC\$
1140 PUT #1,1

COMMUNICATE WITH THE IEEE-488 INTERFACE BOARD ************************************
1150 CMD\$="REMOTE 27"
1160 CALL IE488(CMD\$, VAR%, FLG%, BRD%)

```
1170 CMD$= "OUTPUT 27[$E]"
1180 A$="F1X"
1190 CALL IE488(CMD$,A$,FLG%,BRD%)
1200 X$="X"
1210 CMD$="OUTPUT 27[$E]"
1220 VON$= "O1X"
1230 CALL IE488(CMD$, VON$, FLG%, BRD%)
1240 COUNT%=0
1250 V$="V"
1260 VO$=V$+STR$(PVO)+X$
1270 CMD$="OUTPUT 27[$E]"
1280 TIMER1=TIMER
1290 CALL IE488(CMD$, VO$, FLG%, BRD%)
*************************
COMMUNICATE WITH THE INTERFACE OF MONOCHROMATOR
CONTROLLER
**************************
1300 FIELD 1,1 AS D$
1310 LSET D$=C$
1320 PUT #1,1
1330 PERIOD=0
1500 FOR J=1 TO 1000
1510 FIELD #1,1 AS NUN$
1520 LSET NUN$=NUNI$
1530 PUT #1,1
1540 NU=ASC(INPUT$(1,#1))
1550 PRINT NU
1560 FIELD 1,1 AS NDE$
1570 LSET NDE$=NDEC$
1580 PUT #1,1
1590 ND=ASC(INPUT$(1,#1))
1600 PRINT ND
1610 FIELD 1,1 AS NHU$
1620 LSET NHU$=NHUN$
```

1630 PUT #1,1
1640 NH=ASC(INPUT\$(1,#1))
1650 PRINT NH
1660 NAMP\$=SPACE\$(20)
1670 COUNT%=COUNT%+1
1680 CMD\$="ENTER 27[\$]"

SET TIME INTERVAL BETWEEN DATA POINTS

1690 TIM=TIMER-TIMER1
1700 CALL IE488(CMD\$,PVOL\$,FLG%,BRD%)
1710 PRINT NAMP\$
1720 E1 =VAL(MID\$(PVOL\$,5,20))
1730 DDAT(COUNT%,1)=E1
1740 DDAT(COUNT%,2)=TIM
1750 IF INKEY\$="P" THEN GOTO 2000
1760 ST=TIMER
1770 WHILE PERIOD < RUNTIME
1780 PERIOD =TIMER-ST
1790 WEND

CHECK AND CORRECT THE WAVELENGTHS SHIFTED BY RECORDING-
TIME LAGS

1800 DDAT(J,3)=100*NH+10*ND+NU
1810 IF DDAT(J,3)=FINWAV THEN GOTO 2000
1820 IF DDAT(J,3)-DDAT(J-1,3)>=10 THEN DDAT(J,3)=DDAT(J,3)-CORR
1830 IF DDAT(J,3)-DDAT(J-1,3)<=-10 THEN DDAT(J,3)=DDAT(J,3)+CORR
1840 NEXT J

CLOSE THE INTERFACES

2000 FIELD #1, 1 AS F\$
2010 LSET F\$=M\$

		<u>.</u> 1
		1 1 * D
		¥:

2020 PUT #1,1
2030 CMD\$="OUTPUT 27[\$E]"
2040 VO\$="O0X"
2050 CALL IE488(CMD\$,VO\$,FLG%,BRD%)
2060 CMD\$="LOCAL 27"
2070 CALL IE488(CMD\$, VAR%, FLG%, BRD%)
2080 CLOSE #1

RECORD DATA INTO HARD DISK

2110 FOR K=1 TO COUNT%
2120 WRITE #2,DDAT(K,1),DDAT(K,2),DDAT(K,3)
2130 NEXT K
2140 CLOSE #2
2150 END
VOLTSCAN.BAS
10 'VOLTSCAN.BAS, 2/23/92
20 'PROGRAM TO RECORD PHOTOEMISSION DATA AT A SPECIFIC
30 'WAVELENGTH AS A FUNCTION OF BIAS VOLTAGE
40 USES THE KEITHLEY MODEL 617 PROGRAMMABLE ELECTROMETER
50 'AS VOLTAGE SOURCE AND VOLTMETER
60 'WRITTEN BY C. T. KUO
70 '
80 DIM DDAT(1200,4)
90 '
100 'CHOOSE A DATA FILE
110 '
120 PRINT
130 PRINT

INPUT FILE NAME AND SET TIME INTERVAL BETWEEN DATA POINTS

VOLTSCAN.BAS (continued) 140 INPUT "INPUT FILE NAME FOR DATA":FILE\$ 150 CLOSE #1 160 OPEN FILES FOR APPEND AS # 1 170 IF LOF(1)=0 THEN CLOSE #1 180 ELSE PRINT "FILE ALREADY EXISTS" :CLOSE #1 190 INPUT "TIME INTERVAL FOR DATA IN SECONDS": RUNTIME 200 INPUT "DATA NUMBER":NI 210 ' INITIALIZE THE IEEE-488 INTERFACE BOARD ****************************** 220 'INITIALIZE THE BOARD 230 OPEN FILES FOR OUTPUT AS #1 240 DEF SEG=&HC000 250 CMD\$="SYSCON MAD=3, CIC=1, NOB=1, BA0=&H300" 260 VAR%=0 : FLG%=0 : BRD%=0 : IE488=0 270 CALL IE488(CMD\$, VAR%, FLG%, BRD%) 280 PRINT ********************** INPUT STARTING AND INCREMENT VOLTAGES ************************* 290 INPUT "INPUT STARTING VOLTAGE IN VOLTS": PVO 291 INPUT "VOLTAGE INCREMENT FOR EACH CYCLE", PIN 300 ' 310 CMD\$="REMOTE 27" 320 CALL IE488(CMD\$, VAR%, FLG%, BRD%) 330 CMD\$= "OUTPUT 27[\$E]" 340 A\$="F0X" 350 CALL IE488(CMD\$,A\$,FLG%,BRD%) 360 X\$="X" 370 CMD\$="OUTPUT 27[\$E]" 380 VON\$= "01X" 390 CALL IE488(CMD\$, VON\$, FLG%, BRD%) 400 COUNT%=0

60

VOLTSCAN.BAS (continued)

401 TIMER1=TIMER
410 V\$="V"
411 FOR N=1 TO NI
420 VO\$=V\$+STR\$(PVO)+X\$
430 CMD\$="OUTPUT 27[\$E]"
450 CALL IE488(CMD\$, VO\$, FLG%, BRD%)
470 PERIOD=0
480 PVOL\$=SPACE\$(20)
490 COUNT%=COUNT%+1
500 CMD\$="ENTER 27[\$]"
510 TIM=TIMER-TIMER1
520 CALL IE488(CMD\$,PVOL\$,FLG%,BRD%)
530 PRINT PVOL\$
540 E1=VAL(MID\$(PVOL\$,5,20))
550 DDAT(COUNT%,1)=E1
560 DDAT(COUNT%,2)=TIM
561 DDAT(COUNT%,3)=PVO
561 DDAT(COUNT%,3)=PVO 562 PVO=PVO+PIN
• • • • • • • • • • • • • • • • • • • •
562 PVO=PVO+PIN
562 PVO=PVO+PIN ***********************************

VOLTSCAN.BAS (continued)

WRITE DATA INTO THE OPEN FILE

670 FOR I=1 TO COUNT%
680 WRITE #1, DDAT(I,1), DDAT(I,2), DDAT(I,3) 690 NEXT I
695 CLOSE #1
700 END
PHOLASER.BAS
10 'PROGRAM PHOLASER.BAS ADAPTED FROM VOLTSCAN, 2/23/92
20 'PROGRAM TO TAKE PHOTOEMISSION DATA AT A SPECIFIC BIAS
30 'VOLTAGE AND WAVELENGTH AS A FUNCTION OF TIME
40 USES THE KEITHLEY MODEL 617 PROGRAMMABLE ELECTROMETER 50 'AS VOLTAGE SOURCE AND VOLTMETER
60 'WRITTEN BY C.T.KUO
70 '
80 DIM DDAT(2400,4)
90 '
100 'CHOOSE A DATA FILE
110 '
120 PRINT
130 PRINT

INPUT FILE NAME, TIME INTERVAL BETWEEN DATA POINTS AND
NUMBER OF DATA EXPECTED TO COLLECT

140 INPUT "INPUT FILE NAME FOR DATA";FILE\$
150 CLOSE #1
160 OPEN FILE\$ FOR APPEND AS # 1
170 IF LOF(1)=0 THEN CLOSE #1
180 ELSE PRINT "FILE ALREADY EXISTS" :CLOSE #1

PHOLASER.BAS (continued)

```
190 INPUT "TIME INTERVAL FOR DATA IN SECONDS":RUNTIME
200 INPUT "DATA NUMBER":NI
210 PRINT '
220 PRINT '
230 '
*************************
INPUT THE SPECIFIC WAVELENGTH OF LIGHT SOURCE
*************************
240 INPUT " THE SPECIFIC WAVELENGTH": SWAVE
250 '
260 '
INITIALIZE THE IEEE-488 INTERFACE BOARD
*************************
270 'INITIALIZE THE BOARD
280 OPEN FILES FOR OUTPUT AS #1
290 DEF SEG=&HC000
300 CMD$="SYSCON MAD=3, CIC=1, NOB=1, BA0=&H300"
310 VAR%=0 : FLG%=0 : BRD%=0 : IE488=0
320 CALL IE488(CMD$, VAR%, FLG%, BRD%)
330 PRINT
340 INPUT "INPUT VOLTAGE IN VOLTS": PVO
350 '
360 CMD$="REMOTE 27"
370 CALL IE488(CMD$, VAR%, FLG%, BRD%)
380 CMD$= "OUTPUT 27[$E]"
390 A$="F0X"
400 CALL IE488(CMD$,A$,FLG%,BRD%)
410 X$="X"
420 CMD$="OUTPUT 27[$E]"
430 VON$= "O1X"
440 CALL IE488(CMD$, VON$, FLG%, BRD%)
450 COUNT%=0
460 V$="V"
```

PHOLASER.BAS (continued)

470 VO\$=V\$+STR\$(PVO)+X\$
480 CMD\$="OUTPUT 27[\$E]"
490 TIMER1=TIMER
500 CALL IE488(CMD\$, VO\$, FLG%, BRD%)
510 FOR N=1 TO NI
520 PERIOD=0
530 PVOL\$=SPACE\$(20)
540 COUNT%=COUNT%+1
550 CMD\$="ENTER 27[\$]"
560 TIM=TIMER-TIMER1

READ SIGNAL VOLTAGE

570 CALL IE488(CMD\$,PVOL\$,FLG%,BRD%)
580 PRINT PVOL\$
590 E1=VAL(MID\$(PVOL\$,5,20))
600 DDAT(COUNT%,1)=E1
610 DDAT(COUNT%,2)=TIM

HIT "P" TO CLOSE PROGRAM AT ANY TIME

611 IF INKEY\$="P" THEN GOTO 680
620 ST=TIMER
630 WHILE PERIOD <runtime< td=""></runtime<>
640 PERIOD=TIMER-ST
650 WEND
660 PRINT "PERIOD TIME";PERIOD
670 NEXT N
680 CMD\$="OUTPUT 27[\$E]"
690 VO\$="O0X"
700 CALL IE488(CMD\$, VO\$, FLG%, BRD%)
710 CMD\$="LOCAL 27"
720 CALL 1E488(CMD\$ VAR% FLG% BRD%)

PHOLASER.BAS (continued)

770 END

```
This is Kramers-Kronig calculations-program KKFAB02.FOR
С
     integer dn
     real kk (2200,2), tem (2200,3), ref (2200,3)
     open(1,file='b:fa15en7.prn',status='old')
     open(2,file='c:test#2.dat',status='unknown')
     m = 1
   100 read(1,*,err=5000) ref(m,1),ref(m,2),ref(m,3)
     m = m + 1
     go to 100
 5000 continue
     dn=m-1
     do 200 n = 1, dn, 1
     do 400 i = 1, dn, 1
     if (n.eq.i) goto 400
     tem(i,1) = log(ref(i,3)+ref(n,3))-log(abs(ref(i,3)-ref(n,3)))
  400 continue
     do 500 k = 1, dn, 1
     tem(k,3) = ref(k,2)*tem(k,1)
  500 continue
     do 600 j = 1, dn, 1
     kk(n,1) = kk(n,1)+tem(j,3)
  600 continue
     kk(n,2) = -0.15915494*kk(n,1)
  200 continue
     do 700 1 = 1, dn, 1
     write(2, (1x, 3e15.5)) ref(1,1), kk(1,2), ref(1,3)
  700 continue
     close(1)
     close(2)
     end
```

```
This is Kramers-Kronig calculations- Program FORKRON.FOR
С
     integer dn
     real kk (2200,2), tem (2200,3), ref (2200,4)
     open(1,file='b:kkdat325.prn',status='old')
     open(2,file='C:test#1.dat',status='unknown')
     m = 1
   100 read(1,*,err=5000) ref(m,1),ref(m,2),ref(m,3),ref(m,4)
     m=m+1
     go to 100
 5000 continue
     dn = m - 1
     do 200 n = 1, dn, 1
     do 400 i = 1, dn, 1
     if (n.eq.i) goto 400
     tem(i,1) = log(abs(ref(n,3)-ref(i,3)))*(ref(n,3)-ref(i,3))
     tem(i,2) = log(ref(n,3)+ref(i,3))*(ref(n,3)+ref(i,3))
  400 continue
     do 500 k = 1, dn, 1
     tem(k,3) = ref(k,4)*(tem(k,1)+tem(k,2))
  500 continue
     do 600 i = 1, dn, 1
     kk(n,1)=kk(n,1)+tem(j,3)
  600 continue
     kk(n,2)=(1./6.2831853)*kk(n,1)
  200 continue
     do 700 1 = 1, dn, 1
     write(2, (1x, 3e15.5)) ref(1,1), kk(1,2), ref(1,3)
  700 continue
     close(1)
     close(2)
     end
```

```
This is Kramers-Kronig calculations-program KKRFAB02.FOR
С
     integer dn
     real kk (2200,2), tem (2200,3), ref (2200,3)
     open(1,file='b:rfa1521.prn',status='old')
     open(2,file='b:rfa1521.dat',status='unknown')
     m = 1
   100 read(1,*,err=5000) ref(m,1),ref(m,2),ref(m,3)
     m = m + 1
     go to 100
 5000 continue
     dn=m-1
     do 200 n = 1, dn, 1
     do 400 i = 1, dn, 1
     if (n.eq.i) goto 400
     tem(i,1) = log(ref(i,3)+ref(n,3))+log(abs(ref(i,3)-ref(n,3)))
  400 continue
     do 500 k = 1, dn, 1
     tem(k,3) = ref(k,2)*tem(k,1)
  500 continue
     do 600 j = 1, dn, 1
     kk(n,1) = kk(n,1)+tem(j,3)
  600 continue
     kk(n,2) = -0.3664678*2*kk(n,1)
  200 continue
     do 700 1 = 1, dn, 1
     write(2, (1x, 3e15.5)) ref(1,1), kk(1,2), ref(1,3)
  700 continue
     close(1)
     close(2)
     end
```

REFERENCES

- 1. F. J. Tehan, B. L. Barnett, and J. L. Dye, J. Am. Chem. Soc., 96,7203 (1974).
- 2. J. Papaioannou, S. Jaenicke, and J. L. Dye, J. Solid State Chem.,67, 122 (1987).
- 3. J. L. Dye, M. R. Yemen, M. G. MaGue, and J. -M. Lehn, J. Chem. Phys., 68, 1665 (1978).
- 4. R. S. Bannwart, S. A. Solin, M. G. DeBacker, and J. L. Dye, J. Am. Chem. Soc., 111, 5552 (1989).
- 5. A. S. Ellaboudy, P. B. Smith, and J. L. Dye, J. Am. Chem. Soc., 105, 6490 (1983).
- 6. Mary L. Tinkham, Ph.D. Dissertation, Michigan State University, (1985).
- 7. Ahmed S. Ellaboudy, Ph.D. Dissertation, Michigan State University, (1984).
- 8. J. L. Dye, Prog. Inorg. Chem., 32,327 (1984).
- A. Ellaboudy, M. L. Tinkham, B. Van Eck, J. L. Dye, and P. B. Smith,
 J. Phys. Chem., 88, 3852 (1984).
- 10. J. L. Dye, C. W. Andrews, and J. M. Ceraso, J. Phys. Chem., 79, 3076 (1975).
- 11. M. L. Tinkham, A. Ellaboudy, J. L. Dye, and P. B. Smith, J. Phys. Chem., 90, 14 (1986).
- 12. S. B. Dawes, J. L. Eglin, K. J. Moeggenborg, K. J. Kim, and J. L. Dye, J. Am. Chem. Soc., 113, 1605 (1991).
- 13. J. L. Dye, in "CHEMTRACTS-Inorganic Chemistry", Data Trace Chemistry Publishers, Inc., p. 243 (1993).

- 14. K. J. Moeggenborg, J. Papaioannou, and J. L. Dye, Chem. Mater, 3, 514 (1991).
- 15. M. J. Wagner, R. H. Huang, and J. L. Dye, J. Phys. Chem., 97, 3982 (1993).
- R. H. Huang, M. K. Faber, K. J. Moeggenborg, D. L. Ward, and J. L. Dye, Nature (London), 331, 599 (1988).
- 17. G. Xu, T. -R. Park, R. S. Bannwart, A. Sieradzan, M. G. DeBacker, S. A. Solin, and J. L. Dye, J. De Physique IV, Colloque C5, 1, c5-283 (1991).
- 18. S. Jaenicke and J. L. Dye, J. of Solid State Chem., 54, 320 (1984).
- 19. S. Jaenicke, M. K. Faber, J. L. Dye, and W. P. Pratt, Jr., Solid State Chem., 68, 239 (1987).
- 20. A. C. Albrecht, Acc. Chem. Res., 3, 238 (1970).
- L. Kevan, in "Advances in Radiation Chemistry", Ed. by M. Burton and J. L. Magee, pp 275 298, Wiley-Interscience, New York, N.Y., 1974.
- 22. J. E. Willard, J. Phys. Chem., 79, 2966 (1975).
- 23. A. Ekstrom and J. E. Willard, J. Phys. Chem., 72, 4599 (1968).
- 24. N. V. Klassen, H. A. Gillis, and G. G. Teather, J. Phys. Chem., 76, 3847 (1972).
- 25. S. L. Hager and J. E. Willard, J. Chem. Phys., 61, 3244 (1974).
- 26. G. C. Dismukes, S. L. Hager, G. H. Morine, and J. E. Willard, J. Chem. Phys., 61, 426 (1974).
- 27. D. R. Smith and J. J. Pieroni, Can. J. Chem., 45, 2723 (1967).
- 28. M. J. Blandemer, L. Shields, and M. C. R. Symons, J. Chem. Soc., 1127 (1965).
- 29. L. Kevan, Rev. Phys. Chem., 17, 413 (1981).

- 30. H. Hertz, Ann. Physik 31,983 (1887).
- 31. A. Einstein, Ann. Physik 17,132(1905).
- 32. W. E. Spicer, Phys. Rev., 112, 114 (1958).
- 33. T. E. Fischer, F. G. Allen, and G. W. Gobeli, Phys. Rev., 163, 703 (1967).
- 34. J. I. Pankove, Optical Processes in Semiconductors, p. 288, Dover Publications, Inc., New York, N.Y., 1971.
- 35. N. B. Kindig and W. E. Spicer, Rev. Sci. Instr. 36, 759 (1965).
- 36. J. E. Rowe, S. B. Christman, ans E. E. Chaban, Rev. Sci. Instrum., 44, 1675 (1973).
- 37. D. J. Kennedy and S. T. Manson, Phys. Rev. A5, 227 (1972).
- 38. M. Skibowski, B. Feuerbacher, W. Steinmann, R. P. Godwin, Z. Physik, 211, 329 (1968).
- 39. T. Huen and F. Wooten, Solid State Commun. 9, 871(1971).
- 40. W. E. Spicer and C. N. Berglund, Rev. Sci. Instrum., 35, 1665 (1964).
- 41. P. K. Ghosh, Introduction to Photoelectron spectroscopy, p. 354, John Wiley & Sons, Inc., New York (1983).
- 42. C. N. Berglund and W. E. Spicer, 136, A1030 (1964).
- 43. E. W. Spicer: "Photoelectric Emission", in Optical Properties of Solids, ed. by F. Abele's (Norht-Holland, Amsterdam 1972) P. 792.
- 44. E. O. Kane, Phys. Rev. 127, 131 (1962).
- 45. G. W. Gobeli and F. G. Allen, Phys. Rev. 127, 141 (1962).
- 46. J. I. Pankove, Optical Processes in Semiconductors, p. 294, Dover Publications, Inc., 1971.
- 47. S. Evans, in "Handbook of X-ray and Ultraviolet Photoemission

- spectroscopy", Ed. by D. Briggs, p. 121, Clowes &Sons Limited, London (1978).
- 48. D. Briggs, Handbook of X-ray and ultraviolet photoelectron spectroscopy, p. 121, Heyden & Son Ltd., London (1978).
- 49. R. H. Fowler, Phys. Rev. 38,45 (1931).
- 50. C. Herring, M. H. Nicols, Rev. Mod. Phys. 21, 185 (1949).
- 51. M. Cardona and L. Ley, Photoemission in solid I, p. 40, Springer-Verlag Express, Berlin (1978).
- 52. A. J. Blodgett, Jr. and W. E. Spicer, Phys. Rev., 146, 390 (1966).
- 53. C. N. Berglund and W. E. Spicer, Phys. Rev., 136, A1044 (1964).
- 54. W. E. Spicer, Phys. Rev. Letters, 11, 243 (1963).
- 55. N. V. Smith, Phys. Rev. B, 3, 1862 (1971).
- 56. D. E. Eastman and J. K. Cashion, Phys. Rev. Letters, 24, 310 (1970).
- 57. W. L. Schaich, in "Photoemission in Solid I", Ed. by M. Cardona and L. Ley, p. 105, Springer-Verlag Express, Berlin (1978).
- 58. J. L. Dye, Sci. Am. ,66, 257 (1987).
- 59. R. H. Huang, Ph.D. dissertation, Michigan State University (1987).
- 60. G. K. Wehner in "Methods of Surface Analysis", Vol.1 Methods and phynomena, Ed. by A. W. Czanderna, Elsevier, Amsterdam (1976).
- 61. R. J. Whitefield and J. J. Brady, Phys. Rev. Lett., 26, 380 (1971).
- 62. B. G. Orr and A. M. Goldman, Rev. Sci. Instrum. 56, 1288 (1985).
- 63. N. J. Dinardo, J. E. Demuth, W. A. Thompson, and P. G. Ledermann, Rev. Sci. Instrum., 55, 1492 (1984).
- 65. M. K. Faber, Ph.D. dissertation, michigan State University (1985).
- 66. R. H. Huang and J. L. Dye, unpublished results.
- 67. R. H. Huang, D. L. Ward, and J. L. Dye, J. Am. Chem. Soc., 111, 5707 (1989).

- 68. J. L. Dye, J. M. Ceraso, M. T. Lok, B. L. Barnett, and F. J. Tehan, J. Am. Chem. Soc., 96, 608 (1974).
- 69. R. H. Huang, D. L. Ward, and J. L. Dye, Acata Crystallogr., C46, 1835 (1990).
- 70. E. W. Spicer: "Photoelectric Emission", in Optical Properties of Solids, ed. by F. Abele's (Norht-Holland, Amsterdam 1972) P. 811.
- 71. E. A. Taft and H. R. Philipp, J. Phys. Chem. Solids, 3, 1(1957).
- 72. R. H. Huang and J. L. Dye, Tetrahedron Lett., 32, 5039 (1991).
- 73. F. G. Allen and G. W. Gobeli, Phys. Rev., 127, 150 (1962).
- 74. S. Golden, C. Guttman, and T. R. Tuttle, Jr., J. Chem. Phys. 44, 3791 (1966).
- 75. S. Matalon, S. Golden and M. Ottolenghi, J. Phys. Chem., 73, 3098 (1963).
- 76. S. Golden, C. Guttman, and T. R. Tuttle, Jr., J. Am. Chem. Soc., 87, 135 (1965).
- 77. J. L. Dye, in "Electrons in Fluids", Ed. by J. Jortner and N. R. Kestner, p.77, published by Springer-Verlag, Berlinheidelberg-New York (1973).
- 78. T. -R. Park, S. A. Solin, and J. L. Dye, Phys. Rev. B, 42, 817 (1992).
- 79. D. Huppert and K. H. Bar Eli, J. Phys. Chem., 74, 3285 (1970).
- 80. A. Friedenberg and H. Levanon, J. Phys. Chem., 81, 766 (1977).
- 81. S. H. Glarum and J. H. Marshall, J. Chem. Phys., 52, 5555 (1970).
- 82. M. G. De Backer and F. X. Sauvage, Chem. Phys. Lett., 173, 291 (1990).
- 83. M. A. Nelss and J. E. Willard, J. Phys. Chem., 79, 783 (1975).
- 84. E. A. Taft and H. R. Philipp, J. Phys. Chem. Solids, 3, 1(1957).

- 85. J. L. Dye, J. M. Ceraso, M. T. Lok, B. L. Barnett, and F. J. Tehan, J. Am. Chem. Soc., 96, 608 (1974).
- 86. J. E. Henderickson, W. P. Pratt, Jr., and J. L. Dye, unpublished results.
- 87. H. A. Kramers, Phys. Z., 30, 522 (1929).
- 88. R. de Kronig, Phys. Z., 30, 521 (1929).
- 89. L. V. Ahifors, Complex Analysis, 3rd ed. New York: McGraw-Hill (1979).
- 90. C. Kittel, Introduction to Solid State Physics, 6 ed., P. 293, John Wiley & Sons, New York (1986).
- 91. H. M. Nussenzveig, causality and dispersion relations (Academic, New York, 1985.
- 92. T. S. Moss, Optical Properties of Semiconductors, Butterworths Scientific Publications, London, 1959.
- 93. F. Wooten, Optical Properties of Solids, p. 51, Academic Press, New York, 1972.
- 94. G. Burns, Sloid State Physics, p.458, Academic Press, Boston, 1990.
- 95. M. Hass and B. W. Henvis, J. Phys. Chem. Solids, 23, 1099 (1962).
- 96. F. Stern, Phys. Rev.,133, A1653 (1964).
- 97. D. T. Maple, J. Appl. Phys., 35, 1241 (1964).
- 98. H. R. Phillip, E. A. Taft, Phys. Rev., 30, A1445 (1964).
- 99. M. Balkanski: "Photon-phonon interactions in solids", in Optical Properties of Solids, ed. by F. Abele's (Norht-Holland, Amsterda (1972) P. 558.
- 100. J. I. Pankove, Optical Processes in Semiconductors, p. 90, Dover Publications, Inc., New York, 1971.

- 101. T. Park, S. A. Solin, and J. L. Dye, Solid State Commun., 81, 59, 1992.
- 102. G. Xu, PhD Thesis, Michigan State University, 1992.

